ISSN 0021-3438 (Print)
ISSN 2412-8783 (Online)

IZVESTIYA
NON-FERROUS METALLURGY

Vol. 29, No. 6, 2023

Scientific and Technical Journal
Founded in 1958
6 Issues per year

ИЗВЕСТИЯ ВУЗОВ
ЦВЕТНАЯ МЕТАЛЛУРГИЯ

Том 29, № 6, 2023

Научно-технический журнал
Основан в 1958 г.
Выходит 6 раз в год

ISSN 0021-3438 (Print)
ISSN 2412-8783 (Online)

IZVESTIYA NON-FERROUS METALLURGY

Vol. 29, No. 6
2023

Scientific and Technical Journal Founded in 1958 6 Issues per year http://cvmet.misis.ru

Journal is included into the List of the peer-reviewed scientific publications recommended by the Highest Attestation Commission of the Ministry of Education and Science of the Russian Federation for publishing the results of doctoral and candidate dissertations

Abstracting/Indexing: Russian Science Citation Index (RSCI), Chemical Abstracts (Online), INIS, OCLC ArticleFirst, Ulrich's Periodicals Directory, VINITI Database (Abstract Journal)

Founder

National University of Science and Technology "MISIS"
Address: 4 build. 1 Leninskiy Prosp., Moscow 119049, Russia
http://www.misis.ru

Editor-in-Chief

Evgeny A. Levashov
Prof., Dr. Sci. (Eng.), Acad. of the RANS, NUST MISIS, Moscow, Russia

Deputy Editor

Vladislava A. Ignatkina
Prof., Dr. Sci., NUST MISIS, Moscow, Russia

Editorial Board

Abhilash – Dr., Ph.D., CSIR – National Metallurgical Laboratory, Jamshedpur, India
E.V. Ageev – Prof., Dr. Sci. (Eng.), SouthWest State University, Kursk, Russia
M.V. Ananyev – Prof., Dr. Sci. (Chem.), Federal State Research and Development Institute of Rare Metal Industry (JSC "Giredmet"), Moscow, Russia
N.A. Belov – Prof., Dr. Sci. (Eng.), NUST MISIS, Moscow, Russia
E.V. Bogatyreva – Prof., Dr. Sci. (Eng.), NUST MISIS, Moscow, Russia
V.B. Deev – Prof., Dr. Sci. (Eng.), NUST MISIS, Moscow, Russia
V.M. Denisov – Prof., Dr. Sci. (Chem.), Siberian Federal University, Krasnoyarsk, Russia
D.V. Drobot – Prof., Dr. Sci. (Chem.), Russian Technological University (MITHT), Moscow, Russia
F.V. Grechnikov – Prof., Dr. Sci. (Eng.), Acad. of RAS, Samara National Research University n.a. S.P. Korolev (Samara University), Samara, Russia
D.V. Gunderov – Dr. Sci. (Phys.-Math.), Institute of Molecule and Crystal Physics Ufa Research Center of the RAS, Ufa, Russia
B.B. Khina – Dr. Sci. (Phys.-Math.), The Physical-Techical Institute of NAS of Belarus, Minsk, Belarus
D.V. Louzguine – Prof., Dr. Sci., Tohoku University, Japan
S.V. Mamyachenkov – Prof., Dr. Sci. (Eng.), Ural Federal University, Yekaterinburg, Russia
Z.A. Mansurov – Dr. Sci. (Chem.), Prof., Institute of Combustion Problems, Almaty, Kazakhstan
N.V. Nemchinova – Prof., Dr. Sci. (Eng.), Irkutsk National Research Technical University, Irkutsk, Russia
K.V. Nikitin – Prof., Dr. Sci. (Eng.), Samara State Technical University, Samara, Russia
H.A. Oye – Prof., Dr., Norwegian University of Science and Technology, Trondheim, Norway
P.V. Polyakov – Prof., Dr. Sci. (Chem.), Siberian Federal University, Krasnoyarsk, Russia
E.S. Prusov – Cand. Sci. (Eng.), Vladimir State University, Vladimir, Russia
V.N. Richkov – Prof., Dr. Sci. (Chem.), Ural Federal University, Ekaterinburg, Russia
D. Sadoway – Prof., Dr., Massachusetts Institute of Technology, Boston, USA
G.A. Salishchev – Prof., Dr. Sci. (Eng.), Belgorod National Research University, Belgorod, Russia
D.V. Shtansky – Prof., Dr. Sci. (Phys.-Math.), NUST MISIS, Moscow, Russia
V.M. Sizyakov – Prof., Dr. Sci. (Eng.), Saint-Petersburg Mining University, St. Petersburg, Russia
Stopic Srecko – Dr.-Ing. habil., RWTH Aachen University, Aachen, Germany
B.B. Straumal – Prof., Dr. Sci. (Phys.-Math.), Institute of Solid State Physics of the RAS, Chernogolovka, Moscow region
O.Yu. Tkacheva – Dr. Sci. (Chem.), Institute of High Temperature Electrochemistry of the Ural Branch of the RAS, Yekaterinburg, Russia
M. Verhaege – Prof., Dr., University of Gent, Belgium
G.M. Vol'dman – Prof., Dr. Sci. (Chem.), Russian Technological University (MITHT), Moscow, Russia
G. Xanthopoulou – Dr., National Center for Scientific Research "Demokritos", Agia Paraskevi, Attica, Greece
A.L. Yerokhin – Prof., Dr., University of Manchester, United Kingdom
Onuralp Yücel – Prof., Dr., Istanbul Technical University, Maslak, Istanbul, Turkey
Yu.P. Zaikov – Prof., Dr. Sci. (Chem.), Institute of High Temperature Electrochemistry of the Ural Branch of the RAS, Yekaterinburg, Russia
R.Kh. Zalavutdinov – Cand. Sci. (Phys.-Math.), A.N. Frumkin Institute of Physical Chemistry and Electrochemistry of the RAS, Moscow, Russia
M. Zinigrad – Prof., Dr., Ariel University, Ariel, Israel
A.I. Zouboulis – Prof., Dr., Aristotle University of Thessaloniki, Greece

Editorial Staff

Address: NUST MISIS, 4 build. 1 Leninskiy Prosp.,
Moscow 119049, Russia
Phone: +7 (495) 638-45-35
E-mail: izv.vuz@misis.ru

Certificate of registration No. 015842 (13.03.1997)
Re-registration PI No. ФС77-79229 (25.09.2020)

Subscription: Ural-Press Agency

Leading Editor – O.V. Sosnina
Executive Editor – A.A. Kudinova
Layout Designer – E.A. Legkaya

Signed print 15.12.2023. Format 60×90 1/8.
Offset paper No. 1. Digital printing. Quires 10.5
Order 18886. Free price

Printed in the printing house of the MISIS Publish House
4 build. 1 Leninskiy Prosp., Moscow 119049, Russia. Phone/fax: +7 (499) 236-76-17

© NUST MISIS, Moscow, 2023
© Izvestiya. Non-Ferrous Metallurgy, 2023

Articles are available under Creative Commons Attribution Non-Commercial No Derivatives

ИЗВЕСТИЯ ВУЗОВ
ЦВЕТНАЯ МЕТАЛЛУРГИЯ

ISSN 0021-3438 (Print)
ISSN 2412-8783 (Online)

Том 29, № 6
2023

Научно-технический журнал Основан в 1958 г. Выходит 6 раз в год http://cvmet.misis.ru

Журнал включен в Перечень рецензируемых научных изданий, рекомендованных ВАК Минобрнауки РФ для публикации результатов диссертаций на соискание ученых степеней

Журнал включен в базы данных: Russian Science Citation Index (RSCI), Chemical Abstracts (Online), INIS, OCLC ArticleFirst, Ulrich's Periodicals Directory, РИНЦ, БД/РЖ ВИНИТИ

Учредитель

ФГАОУ ВО Национальный исследовательский технологический университет «МИСИС»
Адрес: 119049, г. Москва, Ленинский пр-т, 4, стр. 1
http://www.misis.ru

Главный редактор

Евгений Александрович Левашов
д.т.н., академик РАЕН, профессор, НИТУ МИСИС, г. Москва

Заместитель главного редактора

Владислава Анатольевна Игнаткина
д.т.н., профессор, НИТУ МИСИС, г. Москва

Редакционная коллегия

Е.В. Агеев – д.т.н., ЮЗГУ, г. Курск
М.В. Ананьев – д.х.н., АО «Гиредмет», г. Москва
Н.А. Белов – д.т.н., проф., НИТУ МИСИС, г. Москва
Е.В. Богатырева – д.т.н., НИТУ МИСИС, г. Москва
Г.М. Вольдман – д.х.н., проф., РТУ (МИТХТ), г. Москва
Ф.В. Гречников – д.т.н., акад. РАН, проф., СНИУ, г. Самара
Д.В. Гундеров – д.ф.-м.н., ИФМК УНЦ РАН, г. Уфа
В.Б. Деев – д.т.н., проф., НИТУ МИСИС, г. Москва
В.М. Денисов – д.х.н., проф., СФУ, г. Красноярск
Д.В. Дробот – д.х.н., проф., РТУ (МИТХТ), г. Москва
Ю.П. Зайков – д.х.н., проф., ИВТЭ УрО РАН, г. Екатеринбург
Р.Х. Залавутдинов – к.ф.-м.н., ИФХЭ РАН, г. Москва
С.В. Мамяченков – д.т.н., проф., УрФУ, г. Екатеринбург
З.А. Мансуров – д.х.н., проф., Институт проблем горения, г. Алматы, Казахстан
Н.В. Немчинова – д.т.н., проф., ИРНИТУ, г. Иркутск
К.В. Никитин – д.т.н., проф., СамГТУ, г. Самара
П.В. Поляков – д.х.н., проф., СФУ, г. Красноярск
Е.С. Прусов – к.т.н., доцент, ВлГУ, г. Владимир
В.Н. Рычков – д.х.н., проф., УрФУ, г. Екатеринбург
Г.А. Салищев – д.т.н., проф., НИУ «БелГУ», г. Белгород
В.М. Сизяков – д.т.н., проф., СПГУ, г. Санкт-Петербург
Б.Б. Страумал – д.ф.-м.н., проф., ИФТТ РАН, г. Черноголовка
О.Ю. Ткачева – д.х.н., ИВТЭ УрО РАН, г. Екатеринбург
Б.Б. Хина – д.ф.-м.н., доц., ФТИ НАН Беларуси, г. Минск, Беларусь
Д.В. Штанский – д.ф.-м.н., проф., НИТУ МИСИС, г. Москва
Abhilash – Dr., Ph.D., CSIR – National Metallurgical Laboratory, Jamshedpur, India
D.V. Louzguine – Prof., Dr., Tohoku University, Japan
H.A. Oye – Prof., Dr., Norwegian University of Science and Technology, Trondheim, Norway
D. Sadoway – Prof., Dr., Massachusetts Institute of Technology, Boston, USA
Stopic Srecko – Dr.-Ing. habil., RWTH Aachen University, Aachen, Germany
M. Verhaege – Prof., Dr., University of Gent, Belgium
G. Xanthopoulou – Dr., National Center for Scientific Research «Demokritos», Agia Paraskevi, Attica, Greece
A.L. Yerokhin – Prof., Dr., University of Manchester, United Kingdom
Yücel Onuralp – Prof., Dr., Istanbul Technical University, Maslak, Istanbul, Turkey
M. Zinigrad – Prof., Dr., Ariel University, Ariel, Israel
A.I. Zouboulis – Prof., Dr., Aristotle University of Thessaloniki, Greece

Редакция журнала

Адрес: 119049, г. Москва, Ленинский пр-т, 4, стр. 1,
НИТУ МИСИС

Тел.: +7 (495) 638-45-35

E-mail: izv.vuz@misis.ru

Свидетельство о регистрации № 015842 от 13.03.1997 г.
Перерегистрация ПИ № ФС77-79229 от 25.09.2020 г.

Подписка: Агентство «Урал-пресс»

Ведущий редактор – О.В. Соснина
Выпускающий редактор – А.А. Кудинова
Дизайн и верстка – Е.А. Легкая

Подписано в печать 15.12.2023. Формат 60×90 1/8.
Бум. офсетная № 1. Печать цифровая. Усл. печ. л. 10,5
Заказ 18886. Цена свободная

Отпечатано в типографии Издательского Дома МИСИС
119049, г. Москва, Ленинский пр-т, 4, стр. 1. Тел./факс: +7 (499) 236-76-17

© НИТУ МИСИС, Москва, 2023
© «Известия вузов. Цветная металлургия», 2023

Статьи доступны под лицензией Creative Commons Attribution Non-Commercial No Derivatives

CONTENTS

Mineral Processing of Non-Ferrous Metals

Metallurgy of Non-Ferrous Metals

Metallurgy of Rare and Precious Metals

Physical Metallurgy and Heat Treatment

СОДЕРЖАНИЕ

Обогащение руд цветных металлов

Металлургия цветных металлов

Металлургия редких и благородных металлов

Металловедение и термическая обработка

MINERAL PROCESSING OF NON-FERROUS METALS / ОБОГАЩЕНИЕ РУД ЦВЕТНЫХ МЕТАЛЛОВ

UDC 622.7'1
https://doi.org/10.17073/0021-3438-2023-6-5-12

Research article
Научная статья

Application of microwave radiation for decrepitation of spodumene from the Kolmozerskoe deposit

O.N. Krivolapova[1], **I.L. Fureev**[2]

[1] **National University of Science and Technology "MISIS"**
4 build. 1 Leninskiy Prosp., Moscow 119049, Russia

[2] **State Research and Design Institute of the Rare Metal Industry (Giredmet JSC)**
2 build. 1 Elektrodnaya Str., Moscow 111524, Russia

✉ Ilya L. Fureev (ifureev@mail.ru)

Abstract: The lithium-ion industry is experiencing a rapidly growing demand for compounds containing lithium. Spodumene is one of the primary industrial minerals used in the production of this metal. It exists in three polymorphic forms. In its natural state, it is known as α-spodumene, which possesses a high resistance to chemical attack due to its compact structure containing silicon and aluminum oxides. When subjected to microwave radiation, α-spodumene undergoes a transformation, first becoming the γ form and then transitioning to the β form. It is known that the β form can be chemically treated to extract lithium. In light of this, microwave exposure was applied to α-spodumene with the aim of decrepitation, followed by sulfuric acid decomposition of the mineral. The mineral was crushed into different sizes (1.0, 0.5, and 0.25 mm). Temperature changes, induced by both conventional and microwave heating, were analyzed. The heating process was continued for samples of various sizes until a temperature of 1200 °C was reached. Sulfation of calcined samples was carried out for 60 minutes at a temperature of 250 °C. After cooling to 22 °C, distilled water was added and mixed for 120 minutes in closed leaching vessels. To determine the recovery of valuable and associated components, leach cakes and the liquid phase were analyzed using inductively coupled plasma atomic emission spectrometry. Based on the analysis of experimental results, the feasibility of using microwave radiation for decrepitation of spodumene to extract lithium is confirmed. The influence of particle size on phase transformations and, consequently, the degree of lithium extraction from spodumene was investigated. It was found that the recovery of lithium during the microwave action and leaching process for particles smaller than 0.25 mm reached 96.82 %. Microwave heating resulted in lower recovery rates of "harmful" components, such as iron, sodium, and calcium, in the leaching process, leading to a higher purity of the resulting product.

Keywords: lithium, spodumene, microwave radiation, decrepitation, sulfation, leaching.

For citation: Krivolapova O.N., Fureev I.L. Application of microwave radiation for decrepitation of spodumene from the Kolmozerskoe deposit. *Izvestiya. Non-Ferrous Metallurgy.* 2023;29(6):5–12. https://doi.org/10.17073/0021-3438-2023-6-5-12

Применение микроволнового излучения для декрипитации сподумена Колмозерского месторождения

О.Н. Криволапова[1], **И.Л. Фуреев**[2]

[1] **Национальный исследовательский технологический университет «МИСИС»**
119049, Россия, г. Москва, Ленинский пр-т, 4, стр. 1

[2] **Государственный научно-исследовательский и проектный институт редкометаллической промышленности (АО «Гиредмет»)**
111524, Россия, г. Москва, ул. Электродная, 2, стр. 1

✉ Илья Леонидович Фуреев (ifureev@mail.ru)

Аннотация: Литий-ионная промышленность демонстрирует быстрорастущий спрос на Li-содержащие соединения. Сподумен является одним из основных промышленных минералов для производства этого металла. Он имеет 3 полиморфные формы.

В природе – это α-сподумен, который обладает высокой устойчивостью к химическому воздействию благодаря своей компактной структуре, содержащей оксиды кремния и алюминия. Микроволновое излучение превращает α-сподумен сначала в γ-, а после в β-форму, и известно, что последняя может подвергаться химическому воздействию с целью извлечения лития. Основываясь на этом факте, была проведена микроволновая процедура воздействия на α-сподумен, направленная на декрипитацию с последующим серно-кислотным разложением минерала, измельченного до разной крупности (1,0, 0,5 и 0,25 мм). Также были проанализированы зависимости изменения температуры при использовании традиционного нагрева. Обычный и микроволновый нагревы образцов различной крупности проводили до достижения температуры 1200 °С. Сульфатизацию прокаленных образцов осуществляли в течение 60 мин при t = 250 °С. После охлаждения до 22 °С добавляли дистиллированную воду и перемешивали в течение 120 мин в закрытых сосудах для выщелачивания. Для определения извлечения ценных и попутных компонентов был проведен анализ кеков выщелачивания и жидкой фазы методом атомно-эмиссионной спектрометрии с индуктивно связанной плазмой. На основе анализа результатов экспериментов обоснована рациональность применения микроволнового излучения для декрипитации сподумена с целью извлечения лития. Изучено влияние крупности на фазовые превращения и, соответственно, степень извлечения лития из сподумена. Показано, что извлечение лития в процессе микроволнового воздействия и выщелачивания класса менее 0,25 мм достигло 96,82 %. Микроволновый нагрев привел к более низким показателям извлечения «вредных» компонентов, таких как железо, натрий и кальций, в процессе выщелачивания, что дает преимущество в чистоте получаемого продукта.

Ключевые слова: литий, сподумен, микроволновое излучение, декрипитация, сульфатизация, выщелачивание.

Для цитирования: Криволапова О.Н., Фуреев И.Л. Применение микроволнового излучения для декрипитации сподумена Колмозерского месторождения. *Известия вузов. Цветная металлургия*. 2023;29(6):5–12.
https://doi.org/10.17073/0021-3438-2023-6-5-12

Introduction

Lithium, a metal with unique physical and chemical properties such as a high specific heat capacity, good conductivity, and strong chemical activity, is finding increasing applications across various industries and technologies. Its utility has expanded from traditional sectors like metallurgy, energy, aerospace, and medicine to the forefront of green energy technologies [1—3]. The current surge in the lithium market is predominantly fueled by the growing demand for energy storage devices [4]. In order to meet the projected lithium demand by 2030, there are plans to achieve the designed capacity of the Russian joint venture between MMC Norilsk Nickel and Rosatom for processing rare metal pegmatites from the Kolmozerskoe deposit (Murmansk Oblast, Russia) [5].

Sulfuric acid leaching is one of the methods employed to extract lithium carbonate from spodumene concentrates. Kola MMC is set to become the largest sulfuric acid producer in the Murmansk Oblast by 2027. They have plans to initiate copper production using the roasting—leaching—electroextraction process [6]. As a byproduct of this process, sulfuric acid will be generated, making it practical to utilize in the processing spodumene from the Kolmozerskoe deposit.

Currently, lithium production in the industry relies on three primary sources [7—9]:

— solid mineral resources, including spodumene, complex Li—Be-pegmatite ores — 50 %, and lithium mica — 20 %;

— liquid mineral resources, encompassing brines, and lake brines, oil formation waters, and thermal waters — 20 %);

— secondary raw materials, which consist of batteries, accumulators, and chemical current sources — 10 %).

Among these industrial minerals used for lithium extraction, spodumene holds significant importance [10]. Its chemical composition includes lithium oxide (8.1 %), aluminum oxide (27.4 %), and silicon dioxide (64.5 %) [11]. The pegmatites from the Kolmozerskoe deposit are not only a valuable source of lithium but also beryllium, tantalum, niobium, and other metals [12].

Spodumene can exist in three distinct modifications: α, β, γ [1]. Natural spodumene is naturally found in the crystalline α phase. The β form results from recrystallization when α spodumene is heated at temperatures within the range of 900 to 1100 °C [13; 14], with complete transformation occurring up to 1100 °C. The γ modification of spodumene is a metastable phase that occurs when α spodumene is heated to temperatures ranging from 700 to 900 °C [2; 15]. The γ phase is characterized by low reactivity and a limited degree of lithium extraction, underscoring the need for decrepitation [16; 17].

Traditional methods of thermal decrepitation have several disadvantages, including high energy consumption and adverse environmental impacts [18]. Additionally, the transportation of hydrocarbon energy resources to the production region in the Murmansk Oblast leads to added costs in the production of finished products. Therefore, it is crucial to assess the feasibility of using microwave radiation in comparison with conventional decrepitation methods.

When compared to conventional heating, microwave heating offers several advantages, including resource savings, shorter processing times, more controlled heating processes, and direct, non-contact selective and bulk heating [11]. Achieving uniform heating throughout the entire material bulk can increase the porosity of the carrier mineral, thereby reducing the required sintering time and the temperature of chemical reactions, while also enhancing the diffusion of the leaching agent within the mineral and improving recovery rates [12; 19]. Consequently, the use of ultrahigh-frequency (microwave) heating for the decrepitation of spodumene can be an efficient and cost-effective method. However, further research is necessary to assess its feasibility.

In terms of their interaction with microwaves, materials can be categorized into three groups: transparent, conductive/opaque, and absorbing [6]. Low dielectric loss materials, such as spodumene, are challenging to heat. However, they can absorb microwaves at elevated temperatures due to increased dielectric losses. Therefore, for microwave heating of such materials, a combined method is typically employed [20]. In this approach, materials are preheated by another heat source to a specific temperature at which they become more efficient in absorbing microwave radiation before being exposed to microwaves directly [13].

The mechanism and the impact of hybrid microwave on the structural changes of spodumene have not been comprehensively studied. Discrepancies in the results of phase transformations observed in spodumene polymorphs at high temperatures can be attributed to differences in grain sizes, impurity concentrations, amorphous materials formed during grinding, as well as variations in experimental setups, heating methods, and temperature measurements [21; 22]. However, the influence of process parameters on the phase transformations of spodumene from the Kolmozerskoe deposit and its leachability has not been thoroughly investigated.

In order to explore the potential advantages of both microwave and direct decrepitation methods, this study examines the calcination of spodumene using microwave radiation, investigates the impact of microwave and direct methods at different material sizes on phase transformations, and consequently assesses the leachability of this mineral. Furthermore, it compares microwave heating with standard methods.

Materials and methods

Mineralogical studies have revealed that the ore from the Kolmozerskoe deposit comprises approximately 20 % spodumene (~1.5÷1.6 % Li_2O), about 30 % quartz, 30 % albite, 15 % microcline, 5 % muscovite, along with traces of zircon and tourmaline [23].

Traditionally, spodumene ores are enriched to yield a concentrate containing roughly 5.0—6.0 % Li_2O and less than 1 % Fe_2O_3 as the raw material for subsequent calcination processes and lithium extraction [24]. For the experiments, spodumene was manually sampled from the ore mass and subjected to analysis. The sample was initially crushed to a particle size of –1 mm, after which quartered samples were further crushed to ensure 100 % content of classes smaller than 0.5 and 0.25 mm. The chemical composition of the quartered samples for research was as follows, wt.%:

Li_2O	5.6
Al_2O_3	25.1
SiO_2	65.7
Fe_2O_3	0.7
Na_2O	1.0

To investigate the efficiency of microwave calcination of the spodumene concentrate and the impact of feedstock size, experiments were conducted to calcine size classes less than 1.0, 0.5, and 0.25 mm. The temperature profiles of the samples over time during direct heating are depicted in Fig. 1.

Samples with particle sizes less than 1.0, 0.5, and 0.25 mm were exposed to direct heating in a muffle furnace, reaching a temperature of 1200 °C. During the initial 10 min of the process, they exhibited varying heating rates, but after this time, the rates equalized and stabilized at approximately 30 °C/min.

The microwave heating of the spodumene concentrate was conducted in a specialized microwave chamber equipped with independent magnetrons and a control system, enabling the adjustment of a 1 kW microwave power at a frequency of 2.5 GHz, along with temperature monitoring. In each test, a 100 g sample of spodumene concentrate was placed in glassware, chosen for its transparency to microwave radiation. The thickness of the material layer remained consistent at 10 mm. Temperature profiles illustrating the relationship between

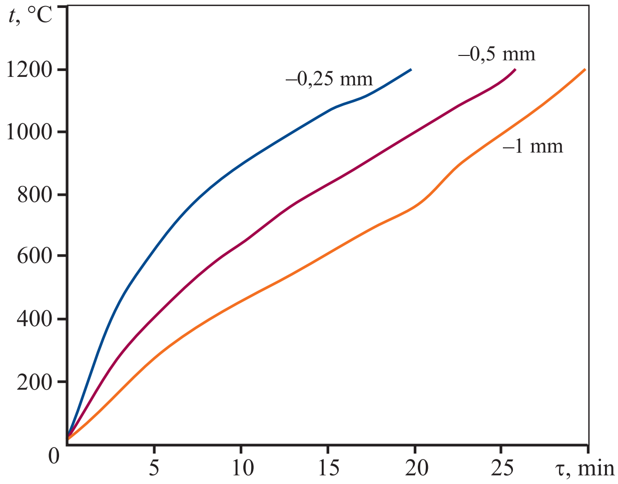

Fig. 1. Temperature as a function of heating duration in a muffle furnace

Рис. 1. Зависимость температуры образцов разной крупности от продолжительности нагрева в муфельной печи

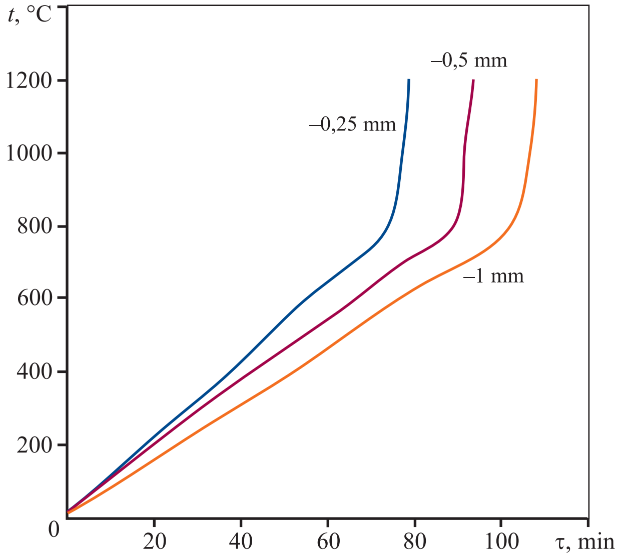

Fig. 2. Temperature as a function of microwave heating duration

Рис. 2. Зависимость температуры образцов разной крупности от продолжительности микроволнового нагрева

temperature and microwave exposure time are presented in Fig. 2.

The efficiency of microwave heating is contingent on the thermophysical properties of the sample [25]. Spodumene exhibits weak absorption of microwave radiation at low temperatures. The heating rate follows a linear pattern up to approximately 700 °C, at which point it reaches around 20 °C/min. This rate is lower compared to direct heating in a muffle furnace. Beyond 800 °C, there is a sharp increase in the heating rate, reaching about 70 °C/min. This significant change is attributed to alterations in the dielectric properties of spodumene as it crosses the critical temperature of approximately 634 °C [13], which explains the rapid acceleration in its heating rate. As the temperature rises to around 800 °C, the heating profiles rapidly become nearly exponential, enabling the temperature to reach 1200 °C in approximately 6 min.

The results indicate that the time required to raise the temperature from 800 to 1200 °C is considerably shorter when microwave radiation is employed. The direct heating method yields the best results for $t < 800$ °C. The temperature profiles depicted in Figs. 1 and 2 highlight the efficiency of microwave hybrid heating of spodumene.

The temperature profiles for different heating methods reveal that smaller spodumene particles undergo a faster transformation into β spodumene with shorter heat exposure times. This implies that particle size has an impact on both microwave and direct heating of spodumene.

The leaching properties of samples subjected to microwave and conventional calcination methods were compared. To extract lithium from the calcined samples, specifically β-spodumene, a process involving sulfatizing roasting followed by water leaching was carried out. In this process, concentrated sulfuric acid was introduced to the calcined sample. The mixture was then heated in an oven at a temperature of 250 °C for 60 min. Following sulfatizing roasting and subsequent cooling to room temperature, distilled water was added, and the resulting mixture was stirred for 120 min at ambient temperature with agitation at 200 rpm. This step was performed to leach the soluble lithium sulfate that was produced during the roasting process. The filtrate, containing the dissolved components, was then separated from the solid residue using a Büchner funnel, Bunsen flask, and filter paper. The leaching cakes and the resulting solutions were analyzed for their Li, Fe, Na, and Ca content. It's important to note that only samples with a particle size smaller than 0.25 mm were investigated in this study.

Results and discussion

Table presents a summary of the metal balance following conventional and microwave radiation treatments.

For direct heating, the lithium extraction rate was 97.37 %, while the microwave procedure yielded a slightly lower rate of 96.82 %. These results indicate that α-spodumene exhibits very low reactivity, suggest-

Metal balance

Баланс металла

Product	Weight (volume), g (ml)	Content, % (g/l)				Extraction, %			
		Li	Fe	Na	Ca	Li	Fe	Na	Ca
Heating in a muffle furnace									
Product solution	(100.02)	(1.27)	(0.02)	(0.30)	(0.57)	97.37	9.81	72.25	94.32
Leaching cake	98.35	0.03	0.22	0.12	0.03	2.63	90.19	27.75	5.68
Initial material	100.00	1.30	0.24	0.42	0.60	100.00	100.00	100.00	100.00
Microwave heating									
Product solution	(100.04)	(1.26)	(0.01)	(0.16)	(0.23)	96.82	5.06	37.36	38.04
Leaching cake	98.23	0.04	0.23	0.27	0.38	3.18	94.94	62.64	61.96
Initial material	100.00	1.30	0.24	0.42	0.60	100.00	100.00	100.00	100.00

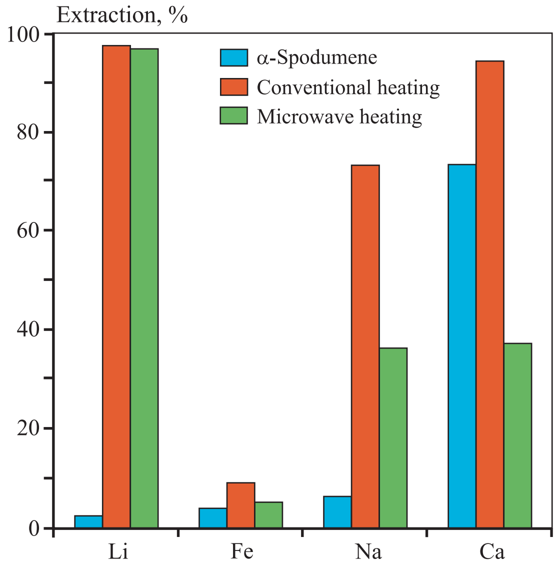

Fig. 3. Extraction of major elements by leaching from initial spodumene concentrates and calcined by microwave and conventional methods

Рис. 3. Извлечение основных элементов при выщелачивании из необработанного и прокаленного с помощью микроволнового и обычного методов нагрева образцов концентрата сподумена

ing limited efficiency in lithium leaching. Fig. 3 illustrates the recovery of iron, sodium, and calcium through leaching from initial spodumene concentrates and those subjected to calcination by both microwave and conventional methods. The obtained results indicate that the extraction of these elements was lower under microwave exposure, providing an advantage over conventional heating in subsequent stages of lithium extraction from the resulting solutions.

Conclusions

In this study, the impact of microwave radiation power on lithium leaching was thoroughly investigated. As the temperature increases to approximately 700 °C, the microwave heating rate experiences a sharp rise, allowing it to reach 1200 °C in approximately 6 minutes. The research has confirmed that microwave power plays a significant role in influencing phase transformations and, consequently, the leaching of calcined samples of spodumene concentrate.

The study has also revealed that the most efficient heating method involves a combination of conventional and microwave treatments on the sample. Based on the research findings, it is suggested that traditional heating should be applied up to a temperature of 800 °C, after which microwave exposure is initiated. This approach allows for achieving the maximum heating rate.

With the combined method, it becomes possible to reach a temperature of 1200 °C in approximately 14 minutes, which is significantly quicker compared to 20 and 80 min required for conventional and microwave exposure, respectively.

By using microwave radiation, a lithium recovery rate of 96.82 % was achieved, which is comparable to the recovery rate of the calcined sample under conventional heating. Moreover, microwave calcination resulted in lower impurity levels in the leachate, presenting an advantage in downstream processing stages.

An establishment of a pilot plant for implementing the combined heating procedure and conducting additional research will enable further validation and refinement of the results obtained.

References

1. Salakjani N.K., Singh P., Nikoloski A.N., Production of lithium — a literature review Pt. 1: Pretreatment of Spodumene. *Mineral Processing and Extractive Metallurgy Review.* 2020; 41(5):335—348.
   https://doi.org/10.1080/08827508.2019.1643343
2. U.S. Geological Survey Mineral commodity summaries 2023. Reston, 2023. 214 p. URL: https://www.kriittisetmateriaalit.fi/wp-content/uploads/2023/02/Mineral-Commodity-Summaries-2023-USGS-Jan-2023.pdf (accessed: 15.06.2023).
3. Kurkov A.V., Mamoshin M.Yu., Anufrieva S.I., Rogozhin A.A. Breakthrough technologies for the direct extraction of lithium from hydromineral raw materials In: *Mineral resource base of high-tech metals. Development, reproduction, use: Proceedings of the Second scientific and practical conference with international participation* (Moscow, December 07—08, 2021). Moscow: FGBU "VIMS", 2021. P. 175—189. (In Russ.).
   Курков А.В., Мамошин М.Ю., Ануфриева С.И., Рогожин А.А. Прорывные технологии прямого извлечения лития из гидроминерального сырья. В сб.: *Минерально-сырьевая база металлов высоких технологий. Освоение, воспроизводство, использование: Труды Второй научно-практической конференции с международным участием* (г. Москва, 07—08 декабря 2021 г.). М.: ФГБУ «ВИМС», 2021. С. 175—189.
4. Infomine Report «Overview of the market of spodumene and lithium hydroxide in the world». Moscow: Infomine, 2021. 179 p. URL: http://www.infomine.ru/research/38/650/ (accessed: 17.04.2023). (In Russ.).
   Отчет «Обзор рынка сподумена и гидроксида лития в мире». М.: ООО «ИГ «Инфомайн», 2021.179 с. URL: http://www.infomine.ru/research/38/650/ (дата обращения: 17.04.2023).
5. Stepanov S.S. Joint venture of Norilsk Nickel and Rosatom received the right to develop the Kolmozerskoye deposit. URL: www.nornickel.ru/news-and-media/press-releases-and-news/sovmestnoe-predpriyatie-nornikelya-i-rosatoma-poluchilo-litsenziyu-na-razrabotku-kolmozerskogo-mestorozhdeniya/ (accessed: 15.06.2023). (In Russ.).
   Степанов С.С. Совместное предприятие «Норникеля» и «Росатома» получило право на разработку Колмозерского месторождения. URL: https://www.nornickel.ru/news-and-media/press-releases-and-news/sovmestnoe-predpriyatie-nornikelya-i-rosatoma-poluchilo-litsenziyu-na-razrabotku-kolmozerskogo-mestorozhdeniya/ (дата обращения: 15.05.2023).
6. Kasikov A.G., Shchelokova E.A., Yakovlev K.A., Korovin V.N., Glukhovskaya I.V. Sulfuric acid decomposition of the spodumene concentrate of the Kolmozerskoe deposit. In: *Proceedings of the Kola Scientific Center of the Russian Academy of Sciences. Series: Engineering Sciences.* 2023;14(2):102—106. (In Russ.).
   http://dx.doi.org/10.37614/2949-1215.2023.14.2.018
   Касиков А.Г., Щелокова Е.А., Яковлев К.А., Коровин В.Н., Глуховская И.В. Сернокислотное разложение сподуменового концентрата Колмозерского месторождения. *Труды Кольского научного центра РАН. Сер.: Технические науки*. 2023;14(2):102—106.
   http://dx.doi.org/10.37614/2949-1215.2023.14.2.018
7. Tadesse B., Makuei F., Albijanic B., Dyer L. The beneficiation of lithium minerals from hard rock ores: A review. *Minerals Engineering.* 2019;131:170—184.
   https://doi.org/10.1016/j.mineng.2018.11.023
8. Youqi Fan, Hu Li, Chang Lu, Shiliang Chen, Yonglin Yao, Hanbing He, Shuai Ma, Zhen Peng, Kangjun Shao. A novel method for recovering valuable metals from spent lithium-ion batteries inspired by the mineral characteristics of natural spodumene. *Journal of Cleaner Production*. 2023; 417(7):41—48.
   https://doi.org/10.1016/j.jclepro.2023.138043
9. Zhang S.J., Cui L.W., Kong L.H., Jiang A.L., Li J.B. Summarize on the lithium mineral resources and their distribution at home and abroad. *Nonferrous Metals Engineering.* 2020;10(10): 95—104.
   https://doi.org/10.3969/j.issn.2095-1744.2020.10.015
10. Zhang L., Yang H.P., Liu L., Ding G.F. 2020. Global technology trends of lithium extraction. *Conservation and Utilization of Mineral Resources*. 2020; 40(5): 24—31.
    https://doi.org/10.13779/j.cnki.issn1001-0076.2020.05.004
11. Roskill: CO_2 emissions from lithium production set to triple by 2025. URL: https://www.greencarcongress.com/2020/10/20201006-roskill.html (accessed: 13.05.2023).
12. Galeeva E.V., Kudryashov N.M. Rare-metal pegmatite deposits of the Kolmozero-Voronya greenstone belt (Kola region). In: *Proceedings of the Fersman Scientific Session of the GI KSC RAS*. Apatity: Geological Institute of the Kola Science Center of the Russian Academy of Sciences, 2022. P. 37—41. (In Russ.).
    https://doi.org/10.31241/FNS.2022.19.007
    Галеева Е.В., Кудряшов Н.М. Редкометальные пегматитовые месторождения зеленокаменного пояса Колмозеро-Воронья (Кольский регион). В сб.: *Труды Ферсмановской научной сессии ГИ КНЦ РАН*. Апатиты: Геологический институт Кольского научного центра Российской академии наук, 2022. С. 37—41.
    https://doi.org/10.31241/FNS.2022.19.007

13. Dessemond C., Soucy G., Harvey J.P., Ouzilleau P. Phase transitions in the α—γ—β spodumene thermodynamic system and impact of γ-spodumene on the efficiency of lithium extraction by acid leaching. *Minerals.* 2020; 10(6):98-107. http://dx.doi.org/10.3390/min10060519
14. Alhadad M.F., Oskierski H.C., Chischi J., Senanayake G., Dlugogorski B.Z. Lithium extraction from β-spodumene: A comparison of keatite and analcime processes. *Hydrometallurgy.* 2023;215:15-23. https://doi.org/10.1016/j.hydromet.2022.105985
15. Salakjani N.Kh., Singh P., Nikoloski A.N. Acid roasting of spodumene: Microwave vs. conventional heating. *Minerals Engineering.* 2019;138:161—167. https://doi.org/10.1016/j.mineng.2019.05.003
16. Morozova L.N., Bazai A.V. Spodumene is the main source of lithium in rare-metal pegmatites of the Kolmozerskoe deposit. In: *Proceedings of the Fersman Scientific Session of the GI KSC RAS.* Apatity: Geological Institute of the Kola Science Center of the Russian Academy of Sciences, 2022. P. 369—373. (In Russ.). https://doi.org/10.31241/FNS.2020.17.070
Морозова Л.Н., Базай А.В. Сподумен — основной источник лития редкометалльных пегматитов Колмозерского месторождения. В сб.: *Труды Ферсмановской научной сессии ГИ КНЦ РАН.* Апатиты: Геологический институт Кольского научного центра Российской академии наук, 2022. С. 369—373. https://doi.org/10.31241/FNS.2020.17.070
17. Yunfeng S., Tianyu Z., Lihua H., Zhongwei Z., Xuheng L., A promising approach for directly extracting lithium from α-spodumene by alkaline digestion and precipitation as phosphate. *Hydrometallurgy.* 2019;189: 68—75. https://doi.org/10.1016/j.hydromet.2019.105141
18. Rezaee M., Han Sh., Sagzhanov D., Hassas B.V, Slawecki T.M., Agrawal D., Akbari H., Mensah-Biney R. Microwave-assisted calcination of spodumene for efficient, low-cost and environmentally friendly extraction of lithium. *Powder Technology.* 2022;397:115—132. https://doi.org/10.1016/j.powtec.2021.11.036
19. Quartarolli L., Brandão B., Silveira A., Nakamura M., Toma H. Improving the lithium recovery using leached beta-spodumene residues processed by magnetic nanohydrometallurgy. *Minerals Engineering.* 2022;186:223-241. https://doi.org/10.1016/j.mineng.2022.107747
20. Nobuyuki M., Shoki K., Eiji M. Microwave-based extractive metallurgy to obtain pure metals: A review. *Cleaner Engineering and Technology.* 2021;5:13—28. https://doi.org/10.1016/j.clet.2021.100306
21. Zhu Y., Zhang D., Qiu S., Liu C., Yu J., Can J. Lithium recovery from pretreated α-spodumene residue through acid leaching at ambient temperature. *Canadian Journal of Chemical Engineering.* 2023;101(8):4360—4373. https://doi.org/10.1002/cjce.24806
22. Yoğurtcuoğlu E. Investigation of the effect of cyanidation after microwave roasting treatment on refractory gold/silver ores by characterization studies. *Physicochemical Problems of Mineral Processing.* 2023;59(1):14—21. https://doi.org/10.37190/ppmp/157487
23. Fureev I.L., Neradovsky Yu. N. Choice of rational technology for processing ore from the Kolmozerskoe deposit based on the study of the chemical and mineral composition of the ore-gathering sample. In: *Proceedings of the Kola Scientific Center of the Russian Academy of Sciences. Series: Engineering sciences.* 2023;14(1):245—249. (In Russ.). http://dx.doi.org/10.37614/2949-1215.2023.14.1.044
Фуреев И. Л., Нерадовский Ю. Н. Выбор рациональной технологии переработки руды Колмозерского месторождения на основе изучения химического и минерального составов рудоразборной пробы. *Труды Кольского научного центра РАН. Сер.: Технические науки.* 2023;14(1):245—249. http://dx.doi.org/10.37614/2949-1215.2023.14.1.044
24. Tadesse B., Makuei F., Albijanic B., Dyer L. The beneficiation of lithium minerals from hard rock ores: A review. *Minerals Engineering.* 2019;131:170—184. https://doi.org/10.1016/j.mineng.2018.11.023
25. Volpi M., Pirola C., Rota C., Joaquim A., Carnaroglio D. Microwave-assisted sample preparation of α-spodumene: A simple procedure for analysis of a complex sample. *Minerals Engineering.* 2022;187:33—42. http://dx.doi.org/10.1016/j.mineng.2022.107820

Information about the authors

Olga N. Krivolapova – Cand. Sci. (Eng.), Associate Professor of the Department of Nonferrous Metals and Gold, National University of Science and Technology "MISIS".
https://orcid.org/0000-0002-5055-9430
E-mail: onk@misis.ru

Ilya L. Fureev – Head of the Department of the Laboratory for the Complex Processing of Ore Raw Materials, State Research and Design Institute of Rare Metal Industry (JSC "Giredmet").
https://orcid.org/0009-0007-7674-526X
E-mail: ifureev@mail.ru

Информация об авторах

Ольга Николаевна Криволапова – к.т.н., доцент кафедры цветных металлов и золота, Национальный исследовательский технологический университет «МИСИС».
https://orcid.org/0000-0002-5055-9430
E-mail: onk@misis.ru

Илья Леонидович Фуреев – руководитель направления лаборатории комплексной переработки рудного сырья, Государственный научно-исследовательский и проектный институт редкометаллической промышленности (АО «Гиредмет»).
https://orcid.org/0009-0007-7674-526X
E-mail: ifureev@mail.ru

Contribution of the authors

O.N. Krivolapova – determined the purpose of the work, supervised the experiments, wrote the article.

I.L. Fureev – prepared mixtures and initial samples, conducted laboratory experiments, participated in the discussion of the results.

Вклад авторов

О.Н. Криволапова – определение цели работы, руководство экспериментами, написание текста статьи.

И.Л. Фуреев – подготовка смеси и исходных образцов, проведение лабораторных экспериментов, участие в обсуждении результатов.

The article was submitted 04.09.2023, revised 08.10.2023, accepted for publication 10.10.2023

Статья поступила в редакцию 04.09.2023, доработана 08.10.2023, подписана в печать 10.10.2023

UDC 669.017:620.197
https://doi.org/10.17073/0021-3438-2023-6-13-21

Research article
Научная статья

Effect of lithium on the anodic behavior of AlTi0.1 aluminum conducting alloy in NaCl electrolyte environment

I.N. Ganiev[1], **G.M. Rakhmatulloeva**[2], **F.Sh. Zokirov**[1], **B.B. Eshov**[2]

[1] **Tajik Technical University named after M.S. Osimi**
10 Academician Rajabov Prosp., Dushanbe 734043, Republic of Tajikistan

[2] **Center for Research of Innovative Technologies**
of the National Academy of Sciences of Tajikistan
299/3 Aini Prosp., Dushanbe 734063, Republic of Tajikistan

✉ Izatullo N. Ganiev (ganievizatullo48@gmail.com)

Abstract: Aluminum ranks as the fourth most conductive metal, trailing behind silver, copper, and gold in electrical conductivity. Annealed aluminum demonstrates an approximate 62 % conductivity of the International IACS compared to annealed standard copper, which registers 100 % IACS at $t = 20$ °C. Because to its low specific gravity, aluminum exhibits twice the conductivity per unit mass compared to copper, showcasing its potential economic advantage as a material for conducting electricity. For equal conductivity (in terms of length), an aluminum conductor exhibits a cross-sectional area 60 % larger than that of copper, while weighing only 48 % of copper's mass. However, the widespread use of aluminum as a conductor in electrical engineering is often challenging and sometimes unfeasible due to its inherent low mechanical strength. Enhancing this crucial property is achievable through the addition of dopants. However, this approach tends to elevate mechanical strength at the cost of noticeable reductions in electrical conductivity. This study investigates the impact of lithium addition on the anodic behavior of an A5 aluminum conductor alloy, specifically modified with 0.1 wt.% Ti (AlTi0.1 alloy), within a NaCl electrolyte environment. The experiments were conducted utilizing the potentiostatic method in potentiodynamic mode at a potential sweep rate of 2 mV/s. Results indicate that the introduction of lithium to the AlTi0.1 alloy leads to a shift in the potentials of free corrosion, pitting, and repassivation towards positive values. Additionally, the corrosion rate decreases by 10–20 % with the incorporation of 0.01–0.50 wt.% Li. Moreover, varying concentrations of chloride ions in the NaCl electrolyte prompt fluctuations in the corrosion rate of the alloys and a shift in electrochemical potentials towards the negative range.

Key words: AlTi0.1 aluminum alloy, lithium, potentiostatic method, stationary potential, corrosion potential, corrosion rate, NaCl electrolyte.

For citation: Ganiev I.N., Rakhmatulloeva G.M., Zokirov F.Sh., Eshov B.B. Effect of lithium on the anodic behavior of AlTi0.1 aluminum conducting alloy in NaCl electrolyte environment. *Izvestiya. Non-Ferrous Metallurgy*. 2023;29(6):13–21.
https://doi.org/10.17073/0021-3438-2023-6-13-21

Влияние лития на анодное поведение алюминиевого проводникового сплава AlTi0.1 в среде электролита NaCl

И.Н. Ганиев[1], **Г.М. Рахматуллоева**[2], **Ф.Ш. Зокиров**[1], **Б.Б. Эшов**[2]

[1] **Таджикский технический университет им. М.С. Осими**
734043, Республика Таджикистан, г. Душанбе, пр-т Академиков Раджабовых, 10

[2] **Центр по исследованию инновационных технологий Национальной академии наук Таджикистана**
734063, Республика Таджикистан, г. Душанбе, пр-т Айни, 299/3

✉ Изатулло Наврузович Ганиев (ganievizatullo48@gmail.com)

Аннотация: Среди всех известных металлов алюминий по электропроводности занимает 4-е место после серебра, меди и золота. Электропроводность отожженного алюминия составляет приблизительно 62 % IACS от электропроводности отожженной стандартной меди, которая при $t = 20$ °С принимается за 100 % IACS. Однако благодаря малому удельному весу алюминий обладает проводимостью на единицу массы в 2 раза большей, чем медь, что дает нам представление об экономической выгодности применения его в качестве материала для проводников. При равной проводимости (одна и та же длина) алюминиевый проводник имеет площадь поперечного сечения на 60 % больше, чем медный, а его масса составляет только 48 % от массы меди. В большинстве случаев в электротехнике использование алюминия в качестве проводника затруднено, а часто и просто невозможно из-за его низкой механической прочности. Повышение этого значимого показателя возможно за счет введения легирующих добавок. В таком случае механическая прочность возрастает, вызывая, однако, заметное снижение электропроводности. В работе исследовано влияние добавки лития на анодное поведение алюминиевого проводникового сплава марки А5, модифицированного 0,1 мас.% Ti (сплава AlTi0.1), в среде электролита NaCl. Эксперименты проведены потенциостатическим методом в потенциодинамическом режиме при скорости развертки потенциала 2 мВ/с. Показано, что добавка лития в сплав AlTi0.1 способствует смещению потенциалов свободной коррозии, питтингообразования и репассивации в положительную область значений, а скорость коррозии при введении 0,01–0,50 мас.% Li снижается на 10–20 %. В зависимости от концентрации хлорид-иона в электролите NaCl отмечен рост скорости коррозии сплавов и смещение электрохимических потенциалов в область отрицательных значений.

Ключевые слова: алюминиевый сплав AlTi0.1, литий, потенциостатический метод, стационарный потенциал, потенциал коррозии, скорость коррозии, электролит NaCl.

Для цитирования: Ганиев И.Н., Рахматуллоева Г.М., Зокиров Ф.Ш., Эшов Б.Б. Влияние лития на анодное поведение алюминиевого проводникового сплава AlTi0.1 в среде электролита NaCl. *Известия вузов. Цветная металлургия*. 2023;29(6):13–21.
https://doi.org/10.17073/0021-3438-2023-6-13-21

Introduction

In many instances within electrical engineering, utilizing aluminum as a conductor poses challenges and, at times, becomes unfeasible due to its inherent low mechanical strength. Furthermore, conductive aluminum, when subjected to cold deformation to enhance its strength, tends to lose this enhanced property at temperatures around 100 °C. While it's possible to enhance its mechanical strength by introducing dopants to create alloys [1—3], this improvement often leads to a notable decrease in electrical conductivity [4—7].

The impact of various alloying elements on both the electrical conductivity and strength of aluminum reveals that the most substantial enhancement in hardness occurs upon the inclusion of poorly soluble alloying elements like Fe, Zr, Mn, Cr, Ti, Ca, and Mg. These elements significantly differ in atomic diameters from aluminum. Given that electrical conductivity stands as a paramount parameter for a conductor material, the selection of alloying elements should carefully consider their influence on altering this property [8—11].

Presently, several theories regarding modification exist, yet a consensus remains elusive in addressing this issue concerning aluminum alloys. This complexity arises primarily due to the intricacies of the modification process, which is reliant on melting and casting conditions. Additionally, the presence of uncontrolled impurities and elements may impact the refinement of the original alloy grain. The additive introduced as a modifier, as exemplified by titanium in our case, should fulfill specific prerequisites:

— exhibit adequate stability in the melt without altering the chemical composition;

— possess a higher melting point than that of aluminum;

— demonstrate structural and dimensional compatibility between the crystal lattices of the modifier and aluminum [12; 13].

The primary function of modifiers lies in reducing surface tension on crystal faces, facilitating an accelerated nucleation rate of crystallization centers. This decelerates crystal growth, consequently augmenting the number of crystallization centers and refining the overall structure. However, there exists no definitive classification distinguishing modifiers into the first and second kinds or dopants, given the absence of substances solely soluble in liquid states and entirely insoluble in solid states [14; 15].

Aspects concerning the corrosion and electrochemical behavior of aluminum alloys are detailed in [16—21].

This study aimed to investigate the impact of lithium addition on the corrosion and electrochemical behavior of A5 aluminum, which was modified with 0.1 wt.% Ti (AlTi0.1 alloy).

Research methods for assessing corrosion and electrochemical characteristics of alloys

Alloy samples were prepared using aluminum grade A5 (State Standard GOST 110669-01), titanium grade TG-90 (State Standard GOST 19807-91), and lithium grade LE-1 (State Standard GOST 8774-75). These alloys were produced in SShOL type furnaces, casting rods with a diameter of 8 mm and a length of 140 mm into graphite molds for electrochemical studies. The end of the electrode served as the working surface, while the non-working part of the samples was insulated with a resin mixture (comprising 50 % rosin and 50 % paraffin). Before immersion in the working solution, the end part of each sample underwent cleaning with sandpaper, polishing, degreasing, thorough washing with alcohol, and then immersion in a NaCl electrolyte solution. The temperature of the solution within the cell was maintained consistently at 20 °C using an MLSh-8 thermostat.

The electrochemical testing of the samples was conducted employing the potentiostatic method in potentiodynamic mode, utilizing a PI-50-1.1 pulse potentiostat with a potential sweep rate set at 2 mV/s within a NaCl electrolyte environment. The reference electrode employed was silver chloride, while the auxiliary electrode used was platinum. The investigation of the electrochemical behavior of ternary alloys followed the methodology outlined in [22—26].

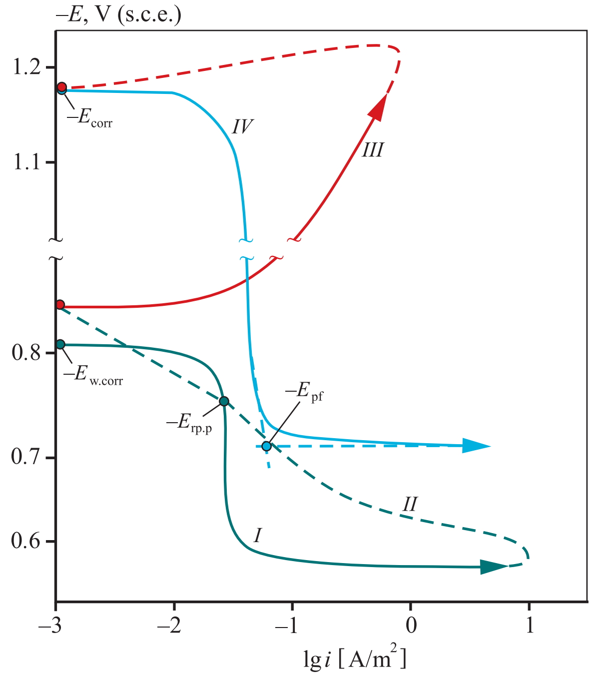

Fig. 1. Full polarization curve (at a potential sweep rate of 2 mV/s) of AlTi0.1 aluminum conducting alloy in a 3.0 % NaCl electrolyte environment

E_{pf} – potential of pitting formation; $E_{rp.p}$ – repassivation potential; E_{corr} – corrosion potential

Рис. 1. Полная поляризационная кривая (при скорости развертки потенциала 2 мВ/с) алюминиевого проводникового сплава AlTi0.1 в среде электролита – 3,0 %-ного NaCl

E_{pf} – потенциал питтингообразования; $E_{rp.p}$ – потенциал репассивации, E_{corr}– потенциал коррозии

For instance, Fig. 1 illustrates the comprehensive polarization diagram concerning the initial AlTi0 aluminum alloy in a 3 % NaCl electrolyte. The samples underwent potentiodynamic polarization, initially moving positively from the established immersion potential until a sharp increase in current denoting pitting (Fig. 1, curve *I*). Subsequently, the samples were polarized in the opposite direction (Fig. 1, curve *II*), and the repassivation potential ($E_{rp.p}$) was determined either from the intersection of curves *I* and *II* or from the inflection point in curve *II*. Following this, the process moved towards the cathode region, reaching a potential value of –1.2 V to eliminate oxide films from the electrode surface (Fig. 1, curve *III*) by alkalization near the electrode surface. Finally, the samples were once again polarized in the positive direction (Fig. 1, curve *IV*), enabling determination of the primary electrochemical parameters pertaining to the alloy's corrosion process from the anodic curves.

The corrosion current (i_{corr}), regarded as the primary electrochemical characteristic of the corrosion process, was computed utilizing the cathodic curve. This calculation considered the Tafel slope (b_k = = 0.12 V) and the understanding that in neutral environments, the pitting corrosion process of aluminum and its alloys is governed by the cathodic reaction involving oxygen ionization. The corrosion rate, on the other hand, is expressed as a function of the corrosion current according to the formula:

$$K = i_{corr}\kappa,$$

where κ = 0.335 g/(A·h), representing the electrochemical equivalent of aluminum.

Results and discussion

The findings from the investigations of corrosion and electrochemical behavior of the AlTi0.1 aluminum alloy, incorporating varying amounts of lithium in a NaCl electrolyte environment, indicate a noticeable shift in the free corrosion potential ($E_{w.corr}$) towards positive values (Fig. 2). Notably, a higher concentration of the modifying component (lithium) correlates with a more positive $E_{w.corr}$ value. Furthermore, transitioning from 0.03 % NaCl to 3.0 % NaCl, results in a more negative $E_{w.corr}$, irrespective of the quantity of the modifying additive (Li) in the AlTi0.1 alloy.

Table summarizes the corrosion and electrochemical behavior of the examined AlTi0.1 alloy across NaCl electrolyte with various concentrations. The table illustrates that an increase in lithium content within the initial AlTi0.1 sample leads to the displacement of

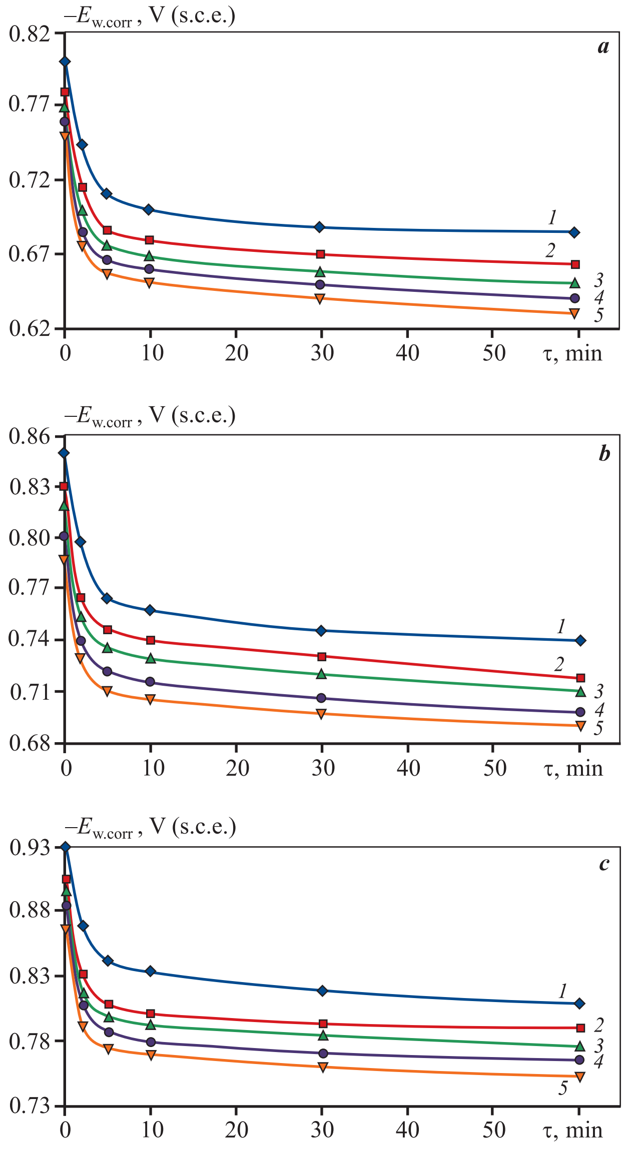

Fig. 2. Potential of free corrosion plotted against time for the initial AlTi0.1 aluminum conducting alloy (*1*) and lithium-modified alloys (***2–5***) in NaCl electrolyte environment, wt.%: 0.03 (***a***), 0.3 (***b***) and 3.0 (***c***)

Li, wt.%: 0 (*1*), 0.01 (*2*), 0.05 (*3*), 0.10 (*4*), 0.50 (*5*)

Рис. 2. Временна́я зависимость потенциала свободной коррозии исходного алюминиевого проводникового сплава AlTi0.1 (*1*) и модифицированных литием образцов (***2–5***) в среде электролита NaCl, мас.%: 0,03 (***a***), 0,3 (***b***) и 3,0 (***c***)

Содержание Li, мас.%: 0 (*1*), 0,01 (*2*), 0,05 (*3*), 0,10 (*4*) и 0,50 (*5*)

corrosion, pitting, and repassivation potentials toward the positive range. This shift is attributed to the establishment of a stable oxide film on the electrode surface within the NaCl environment.

Alloys containing 0.01—0.5 % lithium exhibit a corrosion rate 10—20 % lower than that of the original AlTi0.1 sample.

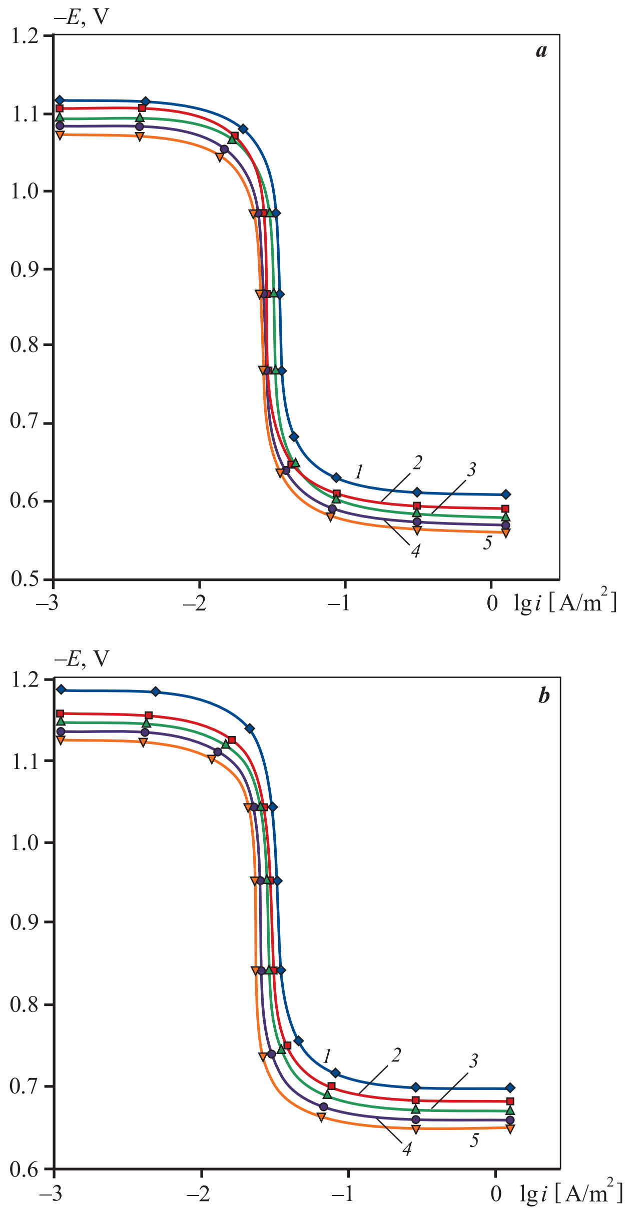

Fig. 3. Anode branches of potentiodynamic curves (potential sweep rate 2 mV/s) of the initial AlTi0.1 aluminum conducting alloy (*1*) and lithium-modified variants (***2–5***) in NaCl electrolyte environment 0.03 % (***a***) and 3.0 % (***b***)

Li, wt.%: 0 (*1*), 0.01 (*2*), 0.05 (*3*), 0.10 (*4*) и 0.50 (*5*)

Рис. 3. Анодные ветви потенциодинамических кривых (скорость развертки потенциала 2 мВ/с) исходного алюминиевого проводникового сплава AlTi0.1 (*1*) и модифицированных образцов (***2–5***) в среде электролита NaCl, мас.%: 0,03 (***a***) и 3,0 (***b***)

Содержание Li, мас.%: 0 (*1*), 0,01 (*2*), 0,05 (*3*), 0,10 (*4*) и 0,50 (*5*)

Consequently, the introduction of lithium into the aluminum conducting alloy AlTi0.1 assists in diminishing the rate of anodic corrosion, as indicated by the shift of the anodic branches in the potentiodynamic curves towards the positive region (Fig. 3). Notably,

Corrosion and electrochemical characteristics of AlTi0.1 aluminum conducting alloy with varying lithium modifications in NaCl electrolyte environment

Коррозионно-электрохимические характеристики алюминиевого проводникового сплава AlTi0.1, модифицированного литием, в среде электролита NaCl

NaCl, wt.%	Li, wt.%	Electrochemical potentials, V (s.c.e.)				Corrosion parameters	
		$-E_{\text{w.corr}}$	$-E_{\text{corr}}$	$-E_{\text{pf.p}}$	$-E_{\text{rp.p}}$	i_{corr}, A/m^2	$K \cdot 10^3$, g/(m$^2 \cdot$h)
0.03	0.0	0.685	1.120	0.610	0.660	0.048	16.0
	0.01	0.663	1.100	0.591	0.640	0.045	15.0
	0.05	0.650	1.090	0.582	0.630	0.043	14.4
	0.1	0.640	1.080	0.570	0.620	0.041	13.7
	0.5	0.630	1.071	0.560	0.610	0.039	13.0
0.30	0.0	0.740	1.150	0.650	0.690	0.068	22.7
	0.01	0.718	1.132	0.630	0.669	0.065	21.7
	0.05	0.710	1.125	0.619	0.660	0.062	21.1
	0.1	0.698	1.112	0.610	0.650	0.061	20.4
	0.5	0.690	1.100	0.600	0.641	0.059	19.7
3.00	0.0	0.809	1.180	0.700	0.750	0.086	28.8
	0.01	0.790	1.165	0.682	0.733	0.083	27.8
	0.05	0.776	1.154	0.670	0.725	0.081	27.1
	0.1	0.765	1.143	0.661	0.716	0.079	26.4
	0.5	0.752	1.130	0.650	0.705	0.077	25.7

the anodic curves associated with the modified alloys are situated to the left of the curve representing the original AlTi0.1 sample, implying a somewhat lower anodic corrosion rate across all examined environments (see Fig. 3).

Figure 4 demonstrates the corrosion rates of the AlTi0.1 alloy relative to lithium content and NaCl electrolyte concentration. It was observed that the addition of lithium to the AlTi0.1 alloy consistently decreases its corrosion rate across all NaCl electrolyte environments under consideration.

Figure 5 illustrates the corrosion current density of the AlTi0.1 aluminum conducting alloy in relation to varying lithium content across different concentrations of NaCl electrolyte. It's evident that as the concentration of the modifier increases, corrosion decreases. Within the range of 0.05—0.50 wt.% lithium concentration in the AlTi0.1 alloy, optimal conditions emerge, exhibiting minimal corrosion rates for these alloys. With an elevation in chloride ion content, there is a noticeable

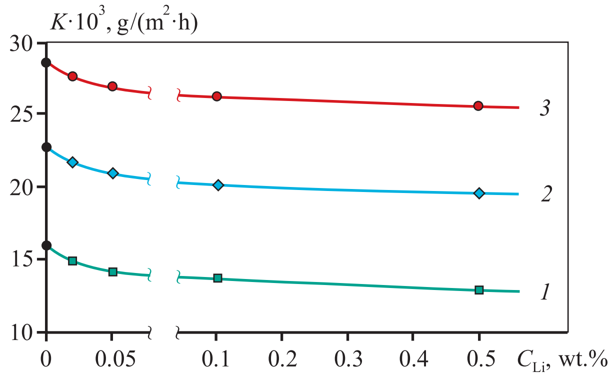

Fig. 4. Corrosion rate variations of the AlTi0.1 aluminum conducting alloy plotted against lithium content in NaCl electrolyte environment, wt.%:
0.03 (***1***), 0.3 (***2***) and 3.0 (***3***)

Рис. 4. Зависимость скорости коррозии алюминиевого проводникового сплава AlTi0.1 от содержания в нем лития и концентрации электролита NaCl, мас.%:
0,03 (***1***), 0,3 (***2***) и 3,0 (***3***)

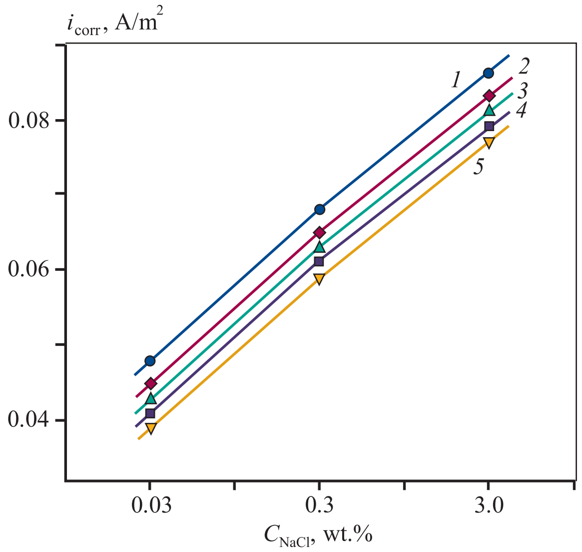

Fig. 5. Corrosion current density comparison between the initial AlTi0.1 aluminum conducting alloy (*1*) and lithium-modified alloys (*2–5*) in relation to the concentration of NaCl electrolyte

Li, wt.%: 0 (*1*), 0.01 (*2*), 0.05 (*3*), 0.10 (*4*), 0.50 (*5*)

Рис. 5. Зависимость плотности тока коррозии исходного алюминиевого проводникового сплава AlTi0.1 (*1*) и модифицированных образцов с литием (*2–5*) от концентрации электролита NaCl

Содержание Li, мас.%: 0 (*1*), 0,01 (*2*), 0,05 (*3*), 0,10 (*4*) и 0,50 (*5*)

increase in the corrosion rate for both the original aluminum alloy and the lithium-modified variant.

Conclusions

Aluminum alloys are highly chemically reactive materials that readily react with oxygen, resulting in the immediate formation of thin oxide films on their surface. Under natural conditions, these films typically reach a thickness of 0.01—0.02 μm and can be increased to 5 or 50 μm through chemical or anodic oxidation [27; 28].

The corrosion resistance of aluminum and its alloys in various aggressive environments significantly depends on the resistance of the oxide film. Additionally, it relies on the chemical composition of the alloy and the surface's heat treatment. It's worth noting that the presence of impurities such as iron, nickel, tin, lead, and other elements forming various phases adversely impacts this resistance [28]. Moreover, the corrosion resistance of such materials is influenced not only by their chemical composition but also by the crystallization nature of excessive phases that determine their structure and form of deposition. Modification (refinement) of binary and ternary eutectics in the alloy structure can substantially alter both mechanical properties and corrosion resistance.

Enhancing the characteristics of aluminum alloys is closely tied to the advancement of new materials and the implementation of sophisticated technological processes in melting and casting. These advancements ensure improved technical and economic indicators in production and the use of resulting products. The quality of these products is also contingent on the chemical composition and structure of the cast metal [27; 28].

The beneficial impact of lithium addition on the anodic properties of the AlTi0.1 aluminum conducting alloy cannot solely be attributed to the enhancement of electrochemical parameters during the anodic process or the densification of the protective phase layer of oxides by poorly soluble oxidation products. The corrosion resistance of aluminum is also affected by structural changes resulting from modification with titanium and lithium, specifically the size of crystal phases within the alloy structure. Metals characterized by low interatomic bonds, thus low melting points, strength, and hardness, can serve as modifiers for alloy structures. This category includes alkali metals.

Consequently, the positive influence of lithium addition on the anodic characteristics and corrosion rates of the AlTi0.1 aluminum conducting alloy in NaCl electrolyte has been confirmed. These observed patterns can be leveraged in developing new aluminum-based conductor alloys tailored for electrical engineering and cable technology requirements.

References

1. Snitovsky Yu.P. The influence of the composition of alloying elements on the physical and mechanical properties of aluminum. *Vestnik Yugorskogo gosudarstvennogo universiteta*. 2022;4(67):68—76. (In Russ.).
https://doi.org/10.18822/byusu20220468-76
Снитовский Ю.П. Влияние состава легирующих элементов на физико-механические свойства алюминия. *Вестник Югорского государственного университета*. 2022;4(67):68—76.
https://doi.org/10.18822/byusu20220468-76
2. Korotkova N.O., Belov N.A., Avksentyeva N.N., Aksenov A.A. The influence of calcium additives on the phase composition and physical and mechanical properties of the conductor alloy Al—0.5% Fe—0.2% Si—0.2% Zr—0.1%Sc. *Fizika metallov i metallovedenie*. 2020; 121(1):105—112. (In Russ.).
https://doi.org/10.31857/S001532302001009X
Короткова Н.О., Белов Н.А., Авксентьева Н.Н, Аксенов А.А. Влияние добавки кальция на фазовый со-

став и физико-механические свойства проводникового сплава Al—0,5% Fe—0,2% Si—0,2% Zr—0,1%Sc. *Физика металлов и металловедение*. 2020; 121(1): 105—112.
https://doi.org/10.31857/S001532302001009X

3. Belov N.A., Alabin A.N., Prokhorov A.Yu. The influence of zirconium additives on the strength and electrical resistance of cold-rolled aluminum sheets. *Izvestiya. Non-Ferrous Metallurgy*. 2009;(4):42—47. (In Russ.).
Белов Н.А., Алабин А.Н., Прохоров А.Ю. Влияние добавки циркония на прочность и электросопротивление холоднокатаных алюминиевых листов. *Известия вузов. Цветная металлургия*. 2009;(4):42—47.
4. Duan Yu., Xu G.F., Zhou L., Xiao D. Achieving high superplasticity of a traditional thermal—mechanical processed non-superplastic Al—Zn—Mg alloy sheet by low Sc additions. *Journal of Alloys and Compounds*. 2015;638:364—373.
https://doi.org/10.1016/j.jallcom.2015.03.090
5. Belov N.A., Alabin A.N., Teleulova A.R. Comparative analysis of alloying additives as applied to the production of heat-resistant aluminum-base wire. *Metal Science and Heat Treatment*. 2012;9:455—459.
https://doi.org/10.1007/s11041-012-9415-5
6. Bely D.I. Aluminum alloys for conductive cores of cable products. *Kabeli i provoda*. 2012;1:8—15. (In Russ.).
Белый Д.И. Алюминиевые сплавы для токопроводящих жил кабельных изделий. *Кабели и провода*. 2012;1:8—15.
7. Chao R.Z., Guan X.H., Guan R.G., Tie D., Lian C., Wang X. Effect of Zr and Sc on mechanical properties and electrical conductivities of Al wires. *Transactions of Non-Ferrous Metals Society of China* (Eng. Ed.). 2014;24:3164—3169. https://doi.org/10.1016/S1003-6326(14)63456-7
8. Fallah V., Langelier B., Ofori-Opoku N., Raeisinia B., Provatas N., Esmaeili S. Cluster evolution mechanisms during aging in Al—Mg—Si alloys. *Acta Materialia*. 2016;103:290—300.
https://doi.org/10.1016/j.actamat.2015.09.027
9. Mavlyutov A.M., Bondarenko A.S., Murashkin M.Y., Boltynjuk E.V., Valiev R.Z., Orlova T.S. Effect of annealing on microhardness and electrical resistivity of nanostructured SPD aluminium. *Journal of Alloys and Compounds*. 2017;698:539—546.
https://doi.org/10.1016/j.jallcom.2016.12.240
10. Ostanina T.V., Shveikin A.I., Trusov P.V. Refinement of the grain structure of metals and alloys under intense plastic deformation: experimental data and analysis of mechanisms. *Vestnik Permskogo natsional'nogo issledovatel'skogo politekhnicheskogo universiteta. Mekhanika*. 2020;2:85—111. (In Russ.).
https://doi.org/10.15593/perm.mech/2020.2.08
Останина Т.В., Швейкин А.И., Трусов П.В. Измельчение зеренной структуры металлов и сплавов при интенсивном пластическом деформировании: экспериментальные данные и анализ механизмов. *Вестник Пермского национального исследовательского политехнического университета. Механика*. 2020;2: 85—111. https://doi.org/10.15593/perm.mech/2020.2.08
11. Gloria A., Montanari R., Richetta M., Varone A. Alloys for aeronautic applications: state of the art and perspectives. *Metals*. 2019;9(6):662.
https://doi.org/10.3390/met9060662
12. Jarry P., Rappaz M. Recent advances in the metallurgy of aluminium alloys. Pt. I: *Solidification and Casting. C. R. Phys*. 2018;19:672—687.
https://doi.org/10.1016/j.crhy.2018.09.003
13. Deev V.B., Ri E.Kh., Prusov E.S., Ermakov M.A., Goncharov A.V. Modification of cast aluminum alloys of the Al—Mg—Si system by treating the liquid phase with nanosecond electromagnetic pulses. *Izvestiya. Non-Ferrous Metallurgy*. 2021;27(4):32—41. (In Russ.).
https://doi.org/10.17073/0021-3438-2021-4-32-41
Деев В.Б., Ри Э.Х., Прусов Е.С., Ермаков М.А., Гончаров А.В. Модифицирование литейных алюминиевых сплавов системы Al—Mg—Si обработкой жидкой фазы наносекундными электромагнитными импульсами. *Известия вузов. Цветная металлургия*. 2021;27(4):32—41.
https://doi.org/10.17073/0021-3438-2021-4-32-41
14. Dolgopolov V.G., Dubrovsky V.A., Simonov M.Yu., Simonov Yu.N., Yurchenko A.N., Shibanova K.A. Methods of influencing the structure and properties of aluminum alloys used in the aerospace industry. *Vestnik PNIPU*. 2016;18(2):50—62. (In Russ.).
https://doi.org/10.15593/2224-9877/2016.2.04
Долгополов В.Г., Дубровский В.А., Симонов М.Ю., Симонов Ю.Н., Юрченко А.Н., Шибанова К.А. Способы влияния на структуру и свойства алюминиевых сплавов, используемых в авиакосмической отрасли. *Вестник ПНИПУ*. 2016;18(2):50—62.
https://doi.org/10.15593/2224-9877/2016.2.04
15. Duyunova V.A., Trapeznikov A.V., Leonov A.A., Koreneva E.A. Modification of cast aluminum alloys (review). *Trudy VIAM*. 2023;4(122):14—26. (In Russ.).
https://doi.org/10.18577/2307-6046-2023-0-4-14-26
Дуюнова В.А., Трапезников А.В., Леонов А.А., Коренева Е.А. Модифицирование литейных алюминиевых сплавов (обзор). *Труды ВИАМ*. 2023;4(122):14—26.
https://doi.org/10.18577/2307-6046-2023-0-4-14-26
16. Grigorieva I.O., Dresvyannikov A.F., Khramova A.V., Mikhalishin I.O. Influence of anions on the electrochemical behavior of aluminum in salt solutions. *Vestnik tekhnologicheskogo universiteta*. 2018;21(7):46—50. (In Russ.).

Григорьева И.О., Дресвянников А.Ф., Храмова А.В., Михалишин И.О. Влияние анионов на электрохимическое поведение алюминия в растворах солей. *Вестник технологического университета*. 2018;21(7):46—50.

17. Grigorieva I.O., Dresvyannikov A.F., Khairullina L.R., Pechenina Yu.S. Features of anodic dissolution of a combined iron-titanium electrode in aqueous solutions containing halide ions. *Vestnik tekhnologicheskogo universiteta*. 2017;20(13):43—47. (In Russ.).
Григорьева И.О., Дресвянников А.Ф., Хайруллина Л.Р., Печенина Ю.С. Особенности анодного растворения комбинированного электрода железо-титан в водных растворах, содержащих галогенид-ионы. *Вестник технологического университета*. 2017;20(13):43—47.
18. Grigorieva I.O., Mezhevich Zh.V. Technology of electrochemical and chemical processing of metals. Kazan: KNRTU, 2019. 144 p. (In Russ.).
Григорьева И.О., Межевич Ж.В. Технология электрохимической и химической обработки металлов. Казань: КНИТУ, 2019. 144 с.
19. Dresvyannikov A.F., Grigoryeva I.O., Khayrullina L.R. Anodic behavior of a titanium-aluminum hybrid electrode: Formation of hydroxide-oxide compounds. *Protection of Metals and Physical Chemistry of Surfaces*. 2017;53(6):1050—1058.
https://doi.org/10.1134/S2070205117060090
20. Popova A. A. Methods of corrosion protection: Lecture course. Saint Petersburg: Lan, 2014. 271 p. (In Russ.).
https://e.lanbook.com/book/211634
Попова А. А. Методы защиты от коррозии: Курс лекций. Санкт-Петербург: Лань, 2014. 272 с.
https://e.lanbook.com/book/211634
21. Andrushevich A.A., Usherenko S.M. Corrosion resistance of dynamically loaded casting alloy AK12. *Lityo i metallurgiya*. 2017;2(87):70—75. (In Russ.).
https://rep.bntu.by/handle/data/31584
Андрушевич А.А., Ушеренко С.М. Коррозионная стойкость динамически нагруженного литейного сплава АК12. *Литье и металлургия*. 2017;2(87):70—75.
https://rep.bntu.by/handle/data/31584
22. Ganiev I.N., Rakhmatulloeva G.M., Zokirov F.Sh., Eshov B.B. The effect of sodium additives on the anodic behavior of AlTi0.1 aluminum conductor alloy in a medium of NaCl electrolyte. *Protection of Metals and Physical Chemistry of Surfaces*. 2023;59(4):451—455.
https://doi.org/10.1134/S2070205123700727
23. Ganiev I.N., Faizulloev R.J., Zokirov F.Sh. The influence of calcium on the anodic behavior of aluminum conductor alloy AlTi0.1 in a NaCl electrolyte environment. *Izvestiya SPbGTI (TU)*. 2021;58(84):33—37. (In Russ.).
https://doi.org/10.36807/1998-9849-2021-58-84-33-37
Ганиев И.Н., Файзуллоев Р.Дж., Зокиров Ф.Ш. Влияние кальция на анодное поведение алюминиевого проводникового сплава AlTi0.1 в среде электролита NaCl. *Известия СПбГТИ (ТУ)*. 2021; 58(84):33—37.
https://doi.org/10.36807/1998-9849-2021-58-84-33-37
24. Zokirov F.Sh., Ganiev I.N., Berdiev A.E., Sangov M.M. The effect of barium on the anodic behavior of the AK12M2 alloy. *Vestnik Tadzhikskogo tekhnicheskogo universiteta. Seriya: Inzhenernye Issledovaniya*. 2018;3(43):30—33. (In Russ.).
Зокиров Ф.Ш., Ганиев И.Н., Бердиев А.Э., Сангов М.М. Влияние бария на анодное поведение сплава АК12М2. *Вестник Таджикского технического университета. Серия: Инженерные исследования*. 2018;3(43):30—33.
25. Zokirov F.Sh., Ganiev I.N., Berdiev A.E., Sangov M.M. The effect of strontium on the anodic behavior of the AK12M2 alloy. *Doklady AN Respubliki Tadzhikistan*. 2019;62(2):93—98. (In Russ.).
Зокиров Ф.Ш., Ганиев И.Н., Бердиев А.Э., Сангов М.М. Влияние стронция на анодное поведение сплава АК12М2. *Доклады АН Республики Таджикистан*. 2019;62(2):93—98.
26. Ganiev I.N., Zokirov F.Sh., Amirov A.J. The influence of lanthanum on the anodic behavior of the aluminum conductor alloy AlTi0.1 in the NaCl electrolyte environment. *Vestnik PNIPU*. 2023;3:66—78. (In Russ.).
https://doi.org/10.15593/2224-9400/2023.3.05
Ганиев И.Н., Зокиров Ф.Ш., Амиров А.Дж. Влияние лантана на анодное поведение алюминиевого проводникового сплава AlTi0.1 в среде электролита NaCl. *Вестник ПНИПУ*. 2023;3:66—78.
https://doi.org/10.15593/2224-9400/2023.3.05
27. Stroganov G.B., Rotenberg V.A., Gershman G.B. Alloys of aluminum with silicon. Moscow: Metallurgiya, 1977. 272 p. (In Russ.).
Строганов Г.Б., Ротенберг В.А., Гершман Г.Б. Сплавы алюминия с кремнием. М.: Металлургия, 1977. 272 с.
28. Postnikov N.S. Corrosion-resistant aluminum alloys. Moscow: Metallurgiya, 1976. 301 p. (In Russ.).
Постников Н.С. Коррозионно-стойкие алюминиевые сплавы. М.: Металлургия, 1976. 301 с.

Information about the authors

Izatullo N. Ganiev – Dr. Sci. (Chem.), Academician of the National Academy of Sciences of Tajikistan, Professor of the Department of Chemical Production Technology, Tajik Technical University n.a. M.S. Osimi.
https://orcid.org/0000-0002-2791-6508
E-mail: ganievizatullo48@gmail.com

Gulnoza M. Rakhmatulloeva – Senior Researcher, Center for Research of Innovative Technologies of the National Academy of Sciences of Tajikistan.
https://orcid.org/0009-0002-2181-0347
E-mail: Golnoz.86@mail.ru

Furkatshoh Sh. Zokirov – Cand. Sci. (Eng.), Associate Professor of the Department of Physics, Tajik Technical University n.a. M.S. Osimi.
https://orcid.org/0009-0000-8174-2214
E-mail: Zokirov090514@mail.ru

Bakhtier B. Eshov – Dr. Sci. (Eng.), Director of the Center for Research of Innovative Technologies of the National Academy of Sciences of Tajikistan.
https://orcid.org/0009-0003-0512-9989
E-mail: Golnoz.86@mail.ru

Информация об авторах

Изатулло Наврузович Ганиев – д.х.н., академик Национальной академии наук (НАН) Таджикистана, профессор кафедры технологии химических производств Таджикского технического университета им. М.С. Осими.
https://orcid.org/0000-0002-2791-6508
E-mail: ganievizatullo48@gmail.com

Гулноза Мухриевна Рахматуллоева – ст. науч. сотрудник Центра по исследованию инновационных технологий НАН Таджикистана.
https://orcid.org/0009-0002-2181-0347
E-mail: Golnoz.86@mail.ru

Фуркатшох Шахриерович Зокиров – к.т.н., доцент кафедры физики Таджикского технического университета им. М.С. Осими.
https://orcid.org/0009-0000-8174-2214
E-mail: Zokirov090514@mail.ru

Бахтиер Бадалович Эшов – д.т.н., директор Центра по исследованию инновационных технологий НАН Таджикистана.
https://orcid.org/0009-0003-0512-9989
E-mail: ishov1967@mail.ru

Contribution of the authors

I.N. Ganiev – formulated the concept, objectives, and goals of the study; wrote the manuscript and contributed to formulating the conclusions.

G.M. Rakhmatulloeva – conducted calculations, wrote the manuscript, and performed sample testing.

F.Sh. Zokirov – supplied resources, organized and supervised experiments, contributed to defining the main concept, objectives, and goals of the study; wrote the manuscript and contributed to the conclusions.

B.B. Eshov – provided scientific oversight, reviewed the manuscript, and contributed to the conclusions.

Вклад авторов

И.Н. Ганиев – формирование основной концепции, постановка цели и задачи исследования, подготовка текста, формулировка выводов.

Г.М. Рахматуллоева – осуществление расчетов, проведение испытаний образцов, подготовка текста статьи.

Ф.Ш. Зокиров – обеспечение ресурсами, подготовка и проведение экспериментов, формирование основной концепции, постановка цели и задачи исследования, подготовка текста, формулировка выводов.

Б.Б. Эшов – научное руководство, корректировка текста, корректировка выводов.

The article was submitted 11.10.2022, revised 04.08.2023, accepted for publication 08.11.2023

Статья поступила в редакцию 11.10.2022, доработана 04.08.2023, подписана в печать 08.11.2023

METALLURGY OF RARE AND PRECIOUS METALS / МЕТАЛЛУРГИЯ РЕДКИХ И БЛАГОРОДНЫХ МЕТАЛЛОВ

UDC 662.7:662.242
https://doi.org/10.17073/0021-3438-2023-6-22-34

Research article
Научная статья

Prospects for refractory gold-sulfide ore processing

V.A. Grigoreva, A.Ya. Boduen

JSC NPO "RIVS"
11 lit. A Zheleznovodskaya Str., Saint Petersburg 199155, Russia

✉ Viktoriya A. Grigoreva (viktoriia.grigoreva98@mail.ru)

Abstract: Cyanide-refractory ores constitute 30 % of the world's gold mineral resource base. With the global decrease in the availability of high-grade and free-milling ores, low-quality ores, including those rich in sulfur and arsenic, are increasingly being processed. The authors have conducted an assessment of the primary factors complicating the leaching process of refractory gold. These factors include the influence of gold distribution within the ore, the presence of preg-robbing effects, and the impact of cyanicidal minerals, notably pyrrhotite, on the leaching process. Sulfide minerals significantly affect the kinetics of gold leaching and associated reagent costs. The behavior of Fe_5S_6 is elucidated through the concept of "chemical depression". Under cyanide leaching conditions, pyrrhotite actively and directly reacts with NaCN/KCN, undergoing surface oxidation by dissolved oxygen in the pulp. This leads to the formation of ferrocyanide complexes and rhodanides, which are unable to leach gold. Presently, there are two approaches to enhance the process parameters of refractory ore processing technology. The first approach involves the inclusion of preparation operations for cyanidation, aimed at liberating gold from the sulfide matrix (including hydrometallurgical and pyrometallurgical oxidation technologies and mechanical activation). An alternative approach is to use alternative reagents as leaching agents (notably thiourea, sodium and ammonium thiosulfates, and halides). The article explores means of modifying the technological process for gold extraction when ores contain substantial amounts of pyrrhotite or concentrates.

Keywords: gold, refractory ores, cyanidation, preg-robbing, pyrrhotite, pyrite, arsenopyrite, leaching.

For citation: Grigoreva V.A., Boduen A.Ya. Prospects for refractory gold-sulfide ore processing. *Izvestiya. Non-Ferrous Metallurgy.* 2023;29(6):22–34. https://doi.org/10.17073/0021-3438-2023-6-22-34

Перспективы переработки упорного золотосульфидного сырья

В.А. Григорьева, А.Я. Бодуэн

АО «НПО «РИВС»
199155, Россия, г. Санкт-Петербург, ул. Железноводская, 11, лит. А

✉ Виктория Александровна Григорьева (viktoriia.grigoreva98@mail.ru)

Аннотация: Мировая минерально-сырьевая база золота на 30 % представлена упорным по отношению к цианиду сырьем. На фоне глобальной тенденции к снижению добычи богатых и легкообогатимых руд в переработку вовлекается низкокачественное сырье, в том числе и с высоким содержанием серы и мышьяка. Авторами оценены основные факторы, затрудняющие процесс выщелачивания упорного золота: влияние форм нахождения золота в сырье, наличие эффекта прег-роббинга, влияние на процесс выщелачивания минералов-цианисидов, в частности пирротина. Сульфидные минералы оказывают значительное влияние на кинетику процесса выщелачивания золота, а также на расходы реагентов. Поведение Fe_5S_6 описывается понятием «химическая депрессия». В условиях цианидного выщелачивания пирротин активно вступает в прямое взаимодействие с NaCN/KCN, подвергается реакциям поверхностного окисления растворенным в пульпе кислородом с образованием ферроцианидных комплексов, роданидов, не проявляющих выщелачивающую способность в отношении золота. На сегодняшний день существуют два подхода к способам повышения технологических показателей технологии переработки упорного сырья. Первый метод предполагает включение в технологическую схему операций подготовки к цианированию, нацеленных на раскрытие заключенного в сульфидную матрицу золота (гидрометаллургические и пирометаллургические технологии окисления, механоактивация). Альтернативным подходом является использование в качестве выщелачивателя иных реагентов (наиболее известные из них – тиомочевина, тиосульфаты натрия и аммония, галоиды). В статье рассматриваются способы модификации технологического процесса извлечения золота при значительных содержаниях пирротина в составе руд или продуктов обогащения.

Ключевые слова: золото, упорные руды, цианирование, прег-роббинг, пирротин, пирит, арсенопирит, выщелачивание.

Для цитирования: Григорьева В.А., Бодуэн А.Я. Перспективы переработки упорного золотосульфидного сырья. *Известия вузов. Цветная металлургия*. 2023;29(6):22–34. https://doi.org/10.17073/0021-3438-2023-6-22-34

Introduction

Gold mining is a global industry with operations on every continent except Antarctica. It is recognized as one of the priority sectors in the global economy. However, as the annual production and consumption of gold continue to increase, the accessible reserves that can be economically processed using conventional methods are diminishing [1]. According to the state report titled “On the state and use of mineral resources of the Russian Federation in 2019” [2], China, which contributes 12 % of the world’s total gold production, holds the position of the largest gold producer globally. Russia ranks among the top three gold producers in the world, with a 10 % share of global production [2]. In 2020, the output of refined gold decreased to 340.2 tons, a decline of less than 1 % compared to the previous year (Fig. 1).

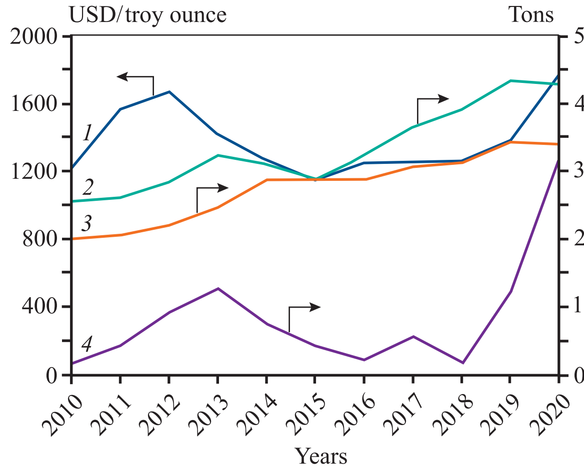

Fig. 1. Dynamics of the price (*1*), mining volumes (*2*), production from minerals and scrap (*3*), and gold exports (*4*) of the Russian Federation

Рис. 1. Динамика показателей цены (*1*), объемов добычи (*2*), производства из минерального сырья и скрапа (*3*) и экспорта золота (*4*) РФ

Over the past 25 years, significant advancements in gold cyanidation have been driven by a variety of factors. These include the diminishing quality of gold deposits, the shift from open-pit to underground mining, the increasing complexity of ore processing, and heightened concerns regarding environmental regulations. As shown in Fig. 2, the primary trends in gold mining innovation are closely tied to the utilization of three key chemical agents: thiosulfate, cyanide, and halides/HCl [3]. A comprehensive evaluation of gold recovery technologies employed at contemporary industrial facilities reveals that the use of cyanide remains the prevailing method.

Approximately 30 % of the world’s gold reserves are considered highly refractory, characterized by high NaCN consumption and suboptimal gold recovery rates. To tackle this issue, two primary approaches have been employed [4]:

— continuing with cyanide technology;

— employing alternative leaching reagents, to which the ore is less refractory.

Traditionally, the classical method involved oxidizing the sulfide component of the ores or concentrates through roasting. However, the high costs associated with purifying the resulting gases, which contain dust, arsenic, and sulfur, have raised questions about the feasibility of this technology [20]. Modern ore pre-treatment methods for cyanidation have shifted towards hydrometallurgical processes, such as autoclave oxidative leaching [5—7], bioleaching [8—10], and oxidation of materials after ultrafine grinding

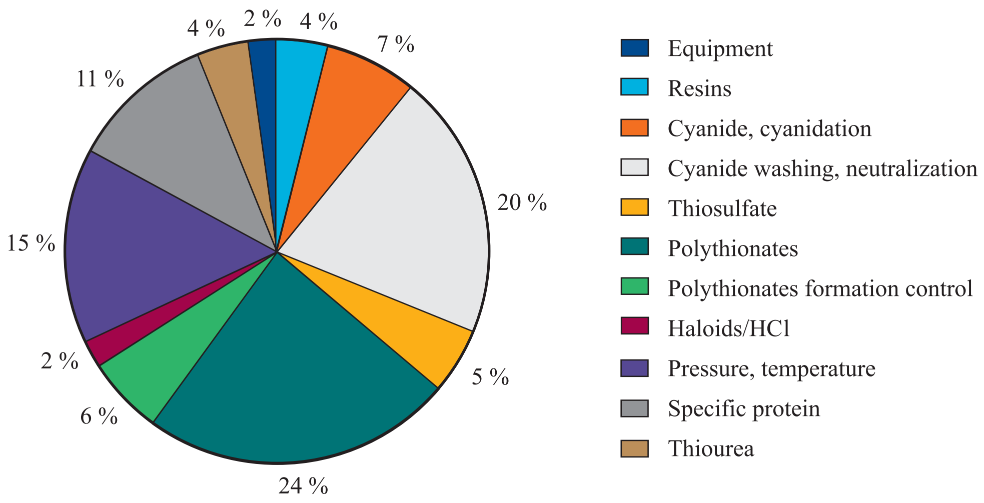

Fig. 2. Percentage of U.S. patents on gold leaching categorized by leaching approaches or reagents [3]

Рис. 2. Доля патентов США по теме выщелачивания золота, разделенных по заявленным подходам к выщелачиванию или реагентам [3]

under atmospheric conditions (Albion process, oxygen-lime treatment) [11; 12].

With the discovery of new deposits, the composition of ores has evolved, leading to challenges caused by a significant pyrrhotine content. To sustain growth in the gold mining industry and maintain metal production at current levels, it's essential to incorporate low-grade gold resources into processing.

However, pyrrhotite presents a challenge as it acts as a chemical depressant and a cyanicide, rendering the standard cyanidation process ineffective. Even concentrating on pyrrhotite-bearing ores through flotation is not straightforward. A study referenced in [13] highlights that the high rate of pyrrhotite oxidation under standard conditions for this method results in waste products that are rich in valuable components, causing significant losses during ore processing.

The low recovery of gold can be attributed to several factors. Firstly, the presence of minerals that absorb cyanide radicals and dissolved oxygen in the pulp inhibits the gold dissolution process. Additionally, the presence of sorption-active carbonaceous material leads to a preg-robbing effect [14]. Furthermore, some researchers have suggested that aurocyan ions are adsorbed by the surfaces of sulfide minerals (such as pyrite, pyrrhotite, and copper sulfides), quartz, and layered silicates [15]. Cyanicides readily dissolve in NaCN solutions and create secondary films on the surface of gold particles. Pyrrhotite, in addition to consuming cyanide, releases sulfide anions into the solution, similar to copper. For the reaction involving just 1 % (10 kg/t) of pyrrhotite in the ore or concentrate, the stoichiometric consumption of cyanide is 38.9 kg [16].

The diminishing quality of ores available for processing leads to increased waste from gold extraction operations, which can contaminate water and soil, resulting in environmental degradation [17]. The development of resource-saving technologies that reduce emissions, enhance working conditions for personnel, and improve the technical and economic efficiency of the processing is a key concern for professionals in the mining industry [18].

The objective of this research is to review existing studies on the processing of refractory gold-bearing ores and concentrates and to assess the effectiveness of well-established technologies for processing pyrrhotite ores.

Impact of ore compositional characteristics

A significant portion of gold-bearing ore deposits consists of a diverse range of minerals, including refractory quartz, carbonate, or sulfide ores. These minerals are notable for containing finely disseminated gold within the host minerals. To determine the direction of technological research for developing an efficient processing method, ore mineral composition is analyzed according to the framework depicted in Fig. 3. The anticipated influence of these factors on the process should be considered in the early stages of research to prevent adverse effects on the economics of a given process.

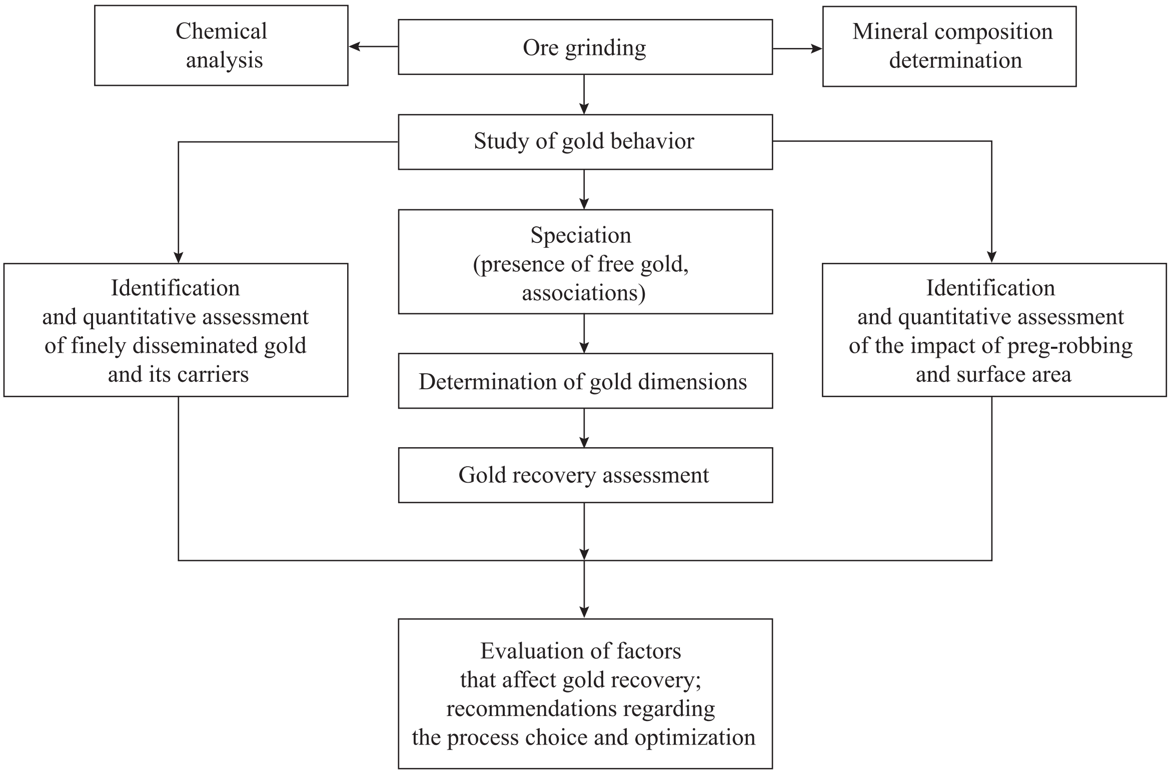

Fig. 3. Framework for gold-bearing ore preparation for investigation

Рис. 3. Блок-схема подготовки золотосодержащего сырья к исследованиям

During a scientific conference, V.V. Lodeishchikov [21] introduced a classification system for refractory gold-bearing ores, categorizing them into four distinct groups (Fig. 4). Group *А* includes ores that do not present complications and can be processed using conventional cyanide technology. They are considered readily cyanidable. Group *Б* consists of ores with finely disseminated gold occurring in other mineral forms, which hinders the penetration of the leaching solution and the contact with gold particles. Ores in Group *В* contain cyanicides, which consume cyanide during the dissolution process, forming inactive complexes that impede gold leaching. Additionally, this group may include minerals that promote the formation of films on the gold surface. And, finally, ores of Group *Г* contain substances of both organic and inorganic origin that exhibit heightened sorption activity.

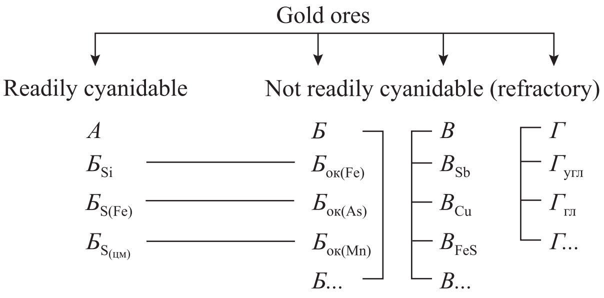

Fig. 4. Classification of gold ores by the degree and nature of their technological refractoriness [21]

Рис. 4. Классификация золотых руд по степени и характеру их технологической упорности [21]

When studying the compositional characteristics of ores, special attention is devoted to the phase analysis of gold deportment. The behavior of gold during cyanidation is influenced by various factors, with a significant focus on its association with ore and rock-forming minerals, and whether the composition includes organic carbon [21—23]. Metallic gold is primarily found in ores and concentrates in four distinct forms:

— free gold;

— associated with host minerals (gold is intergrown with host minerals);

— finely disseminated and submicroscopic (often within quartz and sulfides);

— covered with surface films.

Among sulfide minerals commonly found in refractory gold-bearing ores, arsenopyrite and pyrite are the most prevalent [24]. Any of the above conditions can result in under-recovery or increased reagent consumption [25; 26]. The presence of large, free gold grains may necessitate an extended leaching time for complete dissolution. When gold is disseminated within sulfides or quartz, it becomes less accessible to the leaching solution, causing cyanide and/or oxygen to be consumed in reactions with other mineral forms [27—29], including arsenopyrite, pyrrhotite, copper sulfides, stibnite, realgar, and orpiment.

The association of gold with arsenic-bearing minerals in the ores of the Kanowna Belle Gold Mine in Western Australia was determined, justifying the need to oxidize arsenic-bearing sulphide minerals prior to cyanidation.

Influence of pyrrhotite on cyanide leaching

Rapidly oxidizing iron sulfides, namely pyrite, marcasite, and pyrrhotite, fall into the category of active chemical depressors of the first class. Russian scientists, including V.Ya. Mostovich, G.V. Illyuvnieva, and I.N. Maslenitsky, have extensively studied the reactions of pyrrhotite in alkaline cyanide compound solutions.

Pyrrhotite is characterized by an excess of sulfur and a structurally defective composition. During ore mining, it is highly likely to undergo decomposition, resulting in the formation of sulfuric acid, sulfates, carbonates, basic iron sulfates, and hydrates. Pyrrhotite possesses one weakly bonded sulfur atom that readily reacts with cyanide to produce thiocyanide and iron sulfide. The iron sulfide is rapidly oxidized by oxygen to sulfate, which, in turn, reacts with cyanide to generate ferrocyanide:

$$\mathrm{Fe_5S_6 + NaCN \rightarrow NaCNS + 5FeS}, \tag{1}$$

$$\mathrm{FeS + 2O_2 \rightarrow FeSO_4}, \tag{2}$$

$$\mathrm{FeSO_4 + 6NaCN \rightarrow Na_4[Fe(CN)_6] + Na_2SO_4}. \tag{3}$$

As a result, pyrrhotite not only acts as a cyanicide mineral but also consumes oxygen necessary for the gold dissolution reaction in pulps and solutions (Fig. 5 and 6).

To mitigate these effects, the ore or concentrate can be aerated in an alkaline medium before processing. During this procedure, a protective film forms on the pyrrhotite surface, inhibiting its reaction with the cyanide solution.

Preg-robbing effect

Another common factor contributing to refractoriness in the standard cyanide process is the presence of sorption-active substances and clay minerals [31; 32]. Initially, the term “preg-robbing” [33; 34] referred to carbonaceous materials that competed with activated carbon for the adsorption of gold cyanide complexes. In recent decades, this concept has been expanded to en-

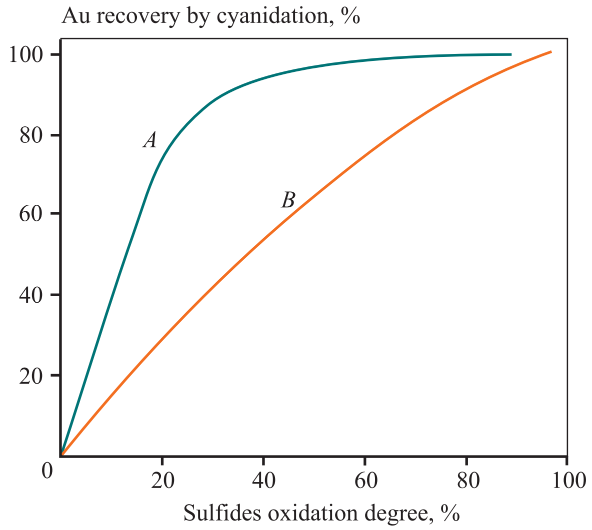

Fig. 5. Effect of oxidation rate on gold recovery, depending on the ore compositional varieties [30]

A: 82 % pyrite, 15 % arsenic pyrite, 3 % pyrrhotine, Au mostly with arsenic pyrite
B: 91 % pyrite, 6.5 % arsenic pyrite, 0.5 % pyrrhotine, 2 % sphalerite, Au is associated with pyrite and arsenic pyrite

Рис. 5. Влияние степени окисления на извлечение золота, в зависимости от минерального состава сырья [30]

A: 82 % пирит, 15 % арсенопирит, 3 % пирротин, Au преимущественно с арсенопиритом
B: 91 % пирит, 6,5 % арсенопирит, 0,5 % пирротин, 2 % сфалерит, Au ассоциировано с пиритом и арсенопиритом

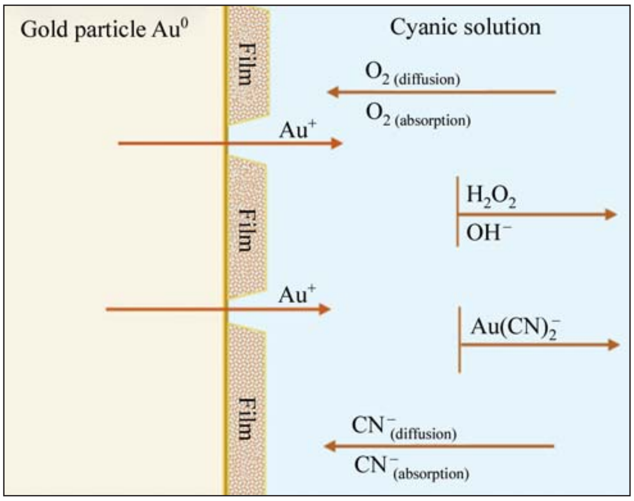

Fig. 6. Process of the gold particle dissolution

Рис. 6. Процесс растворения частицы золота

Table 1. **Mechanisms of preg-robbing depending on the material responsible for the effect**

Таблица 1. Описание механизма прег-роббинга в зависимости от материала, вызывающего данный эффект

Materials	Mechanism
Carbon	Surface adsorption from the gold complex solution
Heavy hydrocarbons	Slight reduction of the preg-robbing effect due to carbon coating
Organic acids (humic substances)	Formation of complexes with gold; low surface adsorption
Kerogen	Physical encapsulation of gold (cannot be considered actual preg-robbing)
Iron-bearing minerals (pyrite, chalcopyrite), silicates	Reduction to the elemental gold state and adsorption on the surface
Clays	Adsorption from rich solutions

compass minerals, clays, and other carbon compounds that, in addition to absorbing soluble gold, can also reduce it to its elemental form. The presence of organic carbon may necessitate roasting, a process that eliminates the sorption-active material that absorbs gold during cyanidation.

The mechanism by which gold dissolves during the cyanidation process varies depending on the nature of the substances causing this effect, as summarized in Table 1.

Another method is chloride preg-robbing, in which gold sorption during pressure oxidation forms the gold chloride complex $[AuCl_4]^-$) [35; 36].

Existing methods for refractory gold-sulfide ore processing

There is currently no universally applicable technology that ensures cost-effective processing of such ores [37]. This is primarily due to variations in the overall chemical, material, and phase composition of the ore, which includes the ratio of gold forms that can be leached by cyanide and those that cannot, as well as the presence of minerals that interfere with the process, such as cyanicides and chemical depressors. As a result, a tailored technological approach is often necessary for each specific deposit [38]. Given these distinctive characteristics, practical methods for ore dressing and metallurgical processing can vary significantly from one deposit to another.

At present, two main strategies are employed to overcome the challenge of processing refractory gold-bearing ores. The first method maintains the use of the cyanide process but includes additional steps to condition the ore or concentrate. Fig. 7 provides an overview of the most common and commercially utilized methods for ore preparation.

Another approach involves the special treatment or leaching of gold using non-cyanide media, where the material is less refractory [40—42].

Considerable attention is devoted to the conditioning and processing of refractory sulfide and carbonaceous ores [43], as well as gravity or flotation concentrates. Typically, fine and ultrafine grinding of refractory ores significantly reduces gold losses in tailings [44]. This process involves a mechanical impact that induces changes in the mineral structure at the molecular level, making it a mechanochemical method. However, fine grinding without subsequent oxidation treatment is suitable for non-sulfide materials only. The mechanochemical method for preparing arsenopyrite-pyrite ores for cyanidation proves inefficient due to incomplete liberation of finely dispersed gold particles and increased chemical reactivity of crushed sulfides.

The objective of oxidative disintegration of ores is to transform sulfides into oxides or sulfates [45]. This process disintegrates the sulfide matrix, allowing the leaching solution to reach previously inaccessible gold particles and dissolve them easily [46].

Table 2 outlines the primary methods for preparing sulfide concentrates for cyanidation, along with some operational characteristics. The economic viability of these technologies is often limited due to high rea-

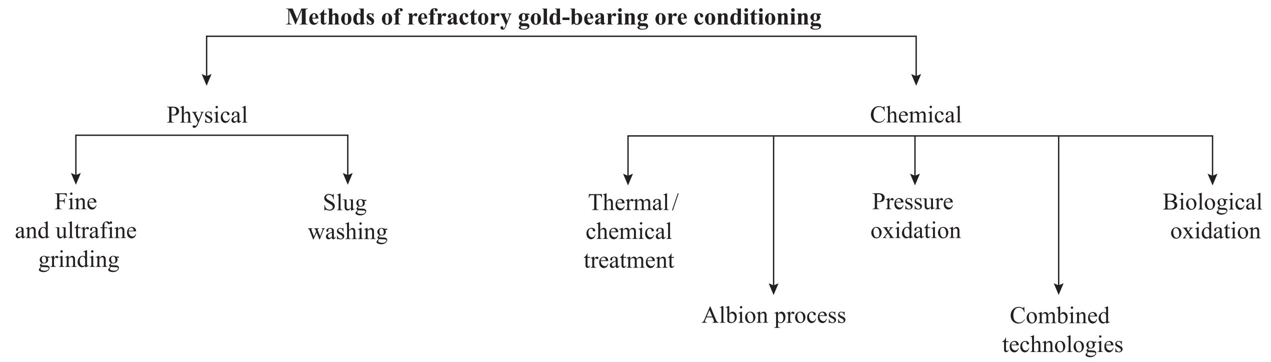

Fig. 7. Classification of conditioning methods [39]

Рис. 7. Классификация способов кондиционирования [39]

gent consumption, energy costs, extended processing times, and other factors. Recent research has been focused on developing alternative methods for extracting gold from refractory sulfide products, primarily based on ultrafine grinding of the material [47; 48]. For example, a study described in [48] presents the optimization of cyanide leaching of pyrrhotite concentrate, highlighting three critical factors influencing the gold leaching rate:

— the extent of pre-crushing to a particle size of P_{80} — 10 μm;

— the volume of oxygen introduced into the system;

— the addition of lead nitrate.

When gold miners select hydrometallurgical technologies for the initial preparation of ores for gold leaching operations, they consider several crucial technological factors [37]:

— a decline in the quality of the ores being processed, marked by an increased presence of detrimental components, particularly arsenic and sulfur;

— the utilization of pyrometallurgical processes for ore preparation, which necessitate costly gas cleaning systems and the management of flue gases and the heat generated during roasting/pyrolysis;

— the suboptimal technical and economic performance of refractory ore treatment when employing direct cyanide technology.

Pyrrhotite, frequently encountered in many gold ores alongside pyrite and/or arsenopyrite, poses numerous challenges during the processing of refractory ores. Unlike pyrite, pyrrhotite reacts most vigorously with cyanide and oxygen, often acting as a reactive anode [50].

Oxidative disintegration of gold-bearing minerals under alkaline conditions is a logical step. This approach eliminates the need for alkalinization after oxidation processes in an acidic medium, which is typically required when the pH is above 10.5 for cyanidation. The alkaline process is suitable for disintegrating minerals such as pyrite, arsenopyrite, selenides, or tellurides.

While investigating the oxidation process based on Albion technology (involving ultrafine grinding followed by oxidation), researchers have examined the reactions of sulfide minerals, particularly pyrite and arsenopyrite [51; 52]. However, the oxidation mechanism of pyrrhotite under these conditions has not been thoroughly explored. Earlier experimental studies have shown that the oxidation of arsenopyrite is more pronounced at a pH $\approx$ 7. These investigations differ from patented technologies related to oxidizing gold-bearing materials in an alkaline medium after preliminary ultrafine grinding [50; 53]. The mechanism of pyrrhotite oxidation remains underexplored, and further experimental studies are needed to describe the physicochemical model of the process.

The study [54] highlights that additional grinding of refractory gold-bearing material containing pyrrhotite inclusions, using ceramic media, significantly enhances gold recovery, with a threefold increase compared to when steel grinding media are employed. This improvement can be attributed to galvanic interactions between the forged steel medium and pyrrhotite, which can lead to the formation of iron hydroxide. Iron hydroxide subsequently reacts with free cyanide to produce ferrocyanide, which, in contrast to free cyanide, is incapable of dissolving gold (resulting in the conversion of 75 % of the free cyanide to ferrocyanide). Moreover, these galvanic interactions markedly reduce the levels of dissolved oxygen and cyanide, making the gold leaching process more complex. Enhanced mechanical activation, therefore, plays a crucial role in improving the recovery of this precious metal.

Table 2. **Methods for treating refractory gold-bearing ores [49]**

Таблица 2. Способы обработки упорного золотосодержащего сырья [49]

Processes		Basic principles	Notes
Pyrometallurgical	Standard roasting [55]	S, As and C in the ores are oxidized and volatilized, and the mineral structure, including gold, is destroyed	This process is dependable but demands significant investments and a rather intricate purification system to eliminate the off-gases
	Roasting by microwave radiation [56; 57]	The material composed of polar molecules is more effective at absorbing microwaves and converting them into heat	High impurities removal rate; thermal efficiency; complex and expensive equipment; off-gas generation
	Roasting with additives [58]	The introduction of additives alters the phase transformation or reaction process, resulting in the formation of new phases during roasting	Calcite voids and gold exposure increase, sulfur and arsenic are present in the calcine
Hydrometallurgical	Acid leaching [59]	Inclusions in minerals are destroyed by acid (e.g., sulfuric acid, hydrochloric acid)	This is typically followed by a roasting treatment; the operation is simple but poorly adapted to the ore
	Alkaline leaching [60; 61]	Sulfides or oxides, which have a significant impact on the gold leaching process and encapsulate the gold, are eliminated by the use of alkaline compounds, such as sodium hydroxide or sodium sulfide	The process is highly efficient, doesn't produce harmful gases, and has low energy consumption. However, it is not well-suited for oxide ores
	Pressure leaching [62; 63]	This is typically accomplished by raising the leaching pressure, often referred to as pressure oxidation (POX) leaching, and conducting fine grinding (mechanical activation)	It is well-suited to the ore and enhances gold recovery efficiency, but the equipment is complex and expensive
	Biological leaching [64]	Microorganisms dissolve sulfides or harmful elements in minerals to aid in the extraction of valuable elements	The method is cost-effective and generates minimal waste. Nevertheless, it is time-consuming, leading to excessive operating costs and may not be well-suited for certain types of ores

Conclusion

The trend of decreasing mined ore quality is persistently growing, necessitating the processing of ores with lower target component content and complex chemical and mineralogical compositions. Presently, the gold mining industry has seen considerable success in dealing with refractory ores in which gold is dispersed within pyrite and arsenopyrite. Bio- and pressure oxidation followed by cyanide leaching are commonly employed for this purpose. However, pyrrhotite is increasingly common in gold-bearing ores, in addition to the traditional sulfide minerals. The behavior of pyrrhotite in the technological process differs significantly from the extensively researched pyrite and arsenopyrite. During cyanide leaching, it reacts with NaCN/KCN and dissolved oxygen in the pulp, leading to increased reagent consumption, reduced gold dissolution rates, and decreased overall process efficiency.

Currently, lime-air pretreatment of the ore or concentrate is used to mitigate the adverse impact of pyrrhotite on the cyanidation process. This operation, although not highly intensive, enhances process performance but offers potential for improvement.

Upon reviewing available sources, it is apparent that the physicochemical transformations of pyrrhotite during oxidation in an alkaline medium remain insufficiently studied. A deeper understanding of this area will facilitate more effective process management and increased efficiency. Consequently, a more comprehensive investigation of the pyrrhotite oxidation mechanism, considering various technological parameters, emerges as an urgent scientific and practical task for the future.

References

1. Ince Ceren. Reusing gold-mine tailings in cement mortars: Mechanical properties and socio-economic developments for the Lefke-Xeros area of Cyprus. *Journal of Cleaner Production*. 2019;238.
https://doi.org/10.1016/j.jclepro.2019.117871
2. Petrov E.I., Teten'kin D.D. On the state and use of mineral resources of the Russian Federation in 2020: Gosudarstvennyi doklad. Moscow, 2021. (In Russ.). URL: https://www.mnr.gov.ru/docs/gosudarstvennye_doklady/gosudarstvennyy_doklad_o_sostoyanii_i_ispolzovanii_mineralno_syrevykh_resursov_2020/ (accessed: 28.04.2023).
Петров Е.И., Тетенькин Д.Д. О состоянии и использовании минерально-сырьевых ресурсов Российской Федерации в 2020 году. Государственный доклад. Москва, 2021. URL: https://www.mnr.gov.ru/docs/gosudarstvennye_doklady/gosudarstvennyy_doklad_o_sostoyanii_i_ispolzovanii_mineralno_syrevykh_resursov_2020/ (дата обращения: 28.04.2023).
3. Vainshtein M.B., Smolianinov V.V., Abashina T.N., Shehvatova G.V. Gold leaching: Trends and proposals. *Zoloto i tekhnologii*. 2015;1:100—103. (In Russ.).
Вайнштейн М.Б., Смолянинов В.В., Абашина Т.Н., Шехватова Г.В. Выщелачивание золота: тенденции и предложения. *Золото и технологии*. 2015;1:100—103.
4. Zakharov B. A., Meretukov M. A. Gold: Refractory ores. Moscow: Ruda i metally, 2013. 452 p. (In Russ.).
Захаров Б. А., Меретуков М. А. Золото: Упорные руды. М.: Руда и металлы, 2013. 452 с.
5. Adams M.D. Advances in gold ore processing. The Nederlands, Elsevier, 2005. Vol. 15. 1076 p.
6. Boginskaia A.S., Markelov A.V., Shneerson Ja.M., Petrov G.V. Application of the mathematical modeling method for calculating the process of autoclave oxidation of a persistent sulfide gold-containing flotation concentrate. *Fundamental'nye issledovaniya*. 2014;3-4: 706—710. (In Russ.).
https://doi.org/10.30906/0023-1134-2002-36-4-44-47
Богинская А.С., Маркелов А.В., Шнеерсон Я.М., Петров Г.В. Применение метода математического моделирования для расчета процесса автоклавного окисления упорного сульфидного золотосодержащего флотоконцентрата. *Фундаментальные исследования*. 2014;3-4:706—710.
https://doi.org/10.30906/0023-1134-2002-36-4-44-47
7. Strauss J.A., Bazhko V., Ventruti G., Liguo X., Gomez M.. Arsenic behavior during the treatment of refractory gold ores via POX: Characterization of Fe—AsO_4—SO_4 precipitates. *Hydrometallurgy*. 2021;203(2):11.
https://doi.org/10.1016/j.hydromet.2021.10561
8. Van Niekerk J.A., Van Buuren C.B., Olivier J.W. Bioprocessing of refractory gold ores: The BIOX, MesoTHERM, and ASTER processes. In: *Biomining Technologies: Extracting and Recovering Metals from Ores and Wastes*. Cham: Springer International Publishing, 2022. P. 67—88.
9. Van Aswegen P.C., Van Niekerk J., Olivier W. The BIOX™ process for the treatment of refractory gold concentrates. *Biomining*. 2007:1—33.
10. Cheng K.Y., Acuña C.C.R., Boxall N.J., Li J., Collinson D., Morris C., Plessis C.A., Streltsova N., Kaksonen A.H. Effect of initial cell concentration on biooxidation of pyrite before gold cyanidation. *Minerals*. 2021;11:834.
https://doi.org/10.3390/min11080834
11. Clary R., DiNuzzo P., Hunter T., Varghese S. Making the right selection: a comparative analysis for the treatment of refractory gold concentrates. *The Minerals, Metals & Materials Series*. 2021:1327—1338.
https://doi.org/10.1007/978-3-319-95022-8_108
12. Khmel'nickaya O.D., Chikina T.V., Lanchakova O.V., Sidorov I.A. A method for extracting precious metals from persistent sulfide-containing raw materials: Patent 2598742 (RF). 2014. (In Russ.).
Хмельницкая О.Д., Чикина Т.В., Ланчакова О.В., Сидоров И.А. Способ извлечения благородных металлов из упорного сульфидсодержащего сырья: Патент 2598742 (РФ). 2014.

13. Chen Y., Shi Q., Feng Q., Lu Y., Zhang W. The effect of conditioning on the flotation of pyrrhotite in the presence of chlorite. *Minerals*. 2017;7(7):125.
https://doi.org/10.3390/min7070125
14. Van den Berg R. Inhibition of the pregrobbing phenomenon in gold ores: Theses of Dissertations. Cape Town, Mowbray, Cape Peninsula University of Technology 2000. 135 p. URL: https://core.ac.uk/download/pdf/148364834.pdf (accessed: 28.04.2023).
15. Ng W.S., Wang Q., Chen M. A review of Preg-robbing and the impact of chloride ions in the pressure oxidation of double refractory ores. *Mineral Processing and Extractive Metallurgy Review*. 2022;43(1):1—28.
https://doi.org/69-96.10.1080/08827508.2020.1793142
16. Processing of refractory ores. URL:https://zolotodb.ru/article/12832 (accessed: 28.04.2023).
Переработка упорных руд. URL: https://zolotodb.ru/article/12832 (дата обращения: 28.04.2023).
17. Sivtseva A. V., Stepanova K.V. The possibility of using gold mining waste for the manufacture of welding materials. *Vestnik Severo-Vostochnogo federal'nogo universiteta im. M.K. Ammosova*. 2009;6(2):138—140. (In Russ.).
Сивцева А.В., Степанова К.В. Возможности использования отходов добычи золота для изготовления сварочных материалов. *Вестник Северо-Восточного федерального университета им. М.К. Аммосова*. 2009; 6(2):138—140.
18. Litvinenko V., Bowbrick I., Naumov I., Zaitseva Z. Global guidelines and requirements for professional competencies of natural resource extraction engineers: Implications for ESG principles and sustainable development goals. *Journal of Cleaner Production*. 2022:130530.
https://doi.org/10.1016/j.jclepro.2022.130530
19. Duryagina A.M., Talovina I.V., Libervirt H., Ilalova R.K. Morphometric parameters of sulfide ores as a basis for selective ore preparation of raw materials. *Zapiski Gornogo Instituta*. 2022;256:527—538. (In Russ.).
https://doi.org/10.31897/PMI.2022.76
Дурягина А.М., Таловина И.В., Либервирт Х., Илалова Р.К. Морфометрические параметры сульфидных руд как основа селективной рудоподготовки сырья. *Записки Горного института*. 2022;256:527—538.
https://doi.org/10.31897/PMI.2022.76
20. Kachor O.L., Sarapulova G.I., Bogdanov A.V. Investigation of the possibility of immobilization of mobile forms of arsenic in technogenic substrates. *Zapiski Gornogo instituta*. 2019;239:596—602. (In Russ.).
https://doi.org/10.31897/pmi.2019.5.596
Качор О.Л., Сарапулова Г.И., Богданов А.В. Исследование возможности иммобилизации подвижных форм мышьяка в техногенных субстратах. *Записки Горного института*. 2019;239:596—602.
https://doi.org/10.31897/pmi.2019.5.596
21. Lodeishchikov V.V. Hydrometallurgy of gold. Moscow: Nauka, 1980. 194 p. (In Russ.).
Лодейщиков В.В. Гидрометаллургия золота. М.: Наука, 1980. 194 с.
22. Hui Li, Zhihang Li, Jianping Jin, Yuexin Han, Yanjun Li. Pore evolution in refractory gold ore formed by oxidation roasting and the effect on the cyanide leaching process. *ACS Omega*. 2022;7(4):3618—3625.
https://doi.org/10.1021/acsomega.1c06248
23. Kaksonen A.H., Perrot F., Morris C., Rea S., Benvie B.Э., Austin P., Hackl R. Evaluation of submerged bio-oxidation concept for refractory gold ores. *Hydrometallurgy*. 2014;141:117—125.
24. Ahtiainen R., Liipo J., Lundström M. Simultaneous sulfide oxidation and gold dissolution by cyanide-free leaching from refractory and double refractory gold concentrates. *Minerals Engineering*. 2021;170:1—8.
https://doi.org/10.1016/j.mineng.2021.107042
25. Afanasova A.V., Aburova V.A., Prohorova E.O., Lushina E.A. Investigation of the effect of depressors on photoactive rock-forming minerals during flotation of sulfide gold-bearing ores. *Gornyi informatsionno-analiticheskii byulleten'*, 2022; (6-2):161. (In Russ.).
https://doi.org/10.25018/0236_1493_2022_62_0_161
Афанасова А.В., Абурова В.А., Прохорова Е.О., Лушина Е.А. Исследование влияния депрессоров на флотоактивные породообразующие минералы при флотации сульфидных золотосодержащих руд. *Горный информационно-аналитический бюллетень*. 2022;(6-2):161.
https://doi.org/10.25018/0236_1493_2022_62_0_161
26. Aleksandrova T., Nikolaeva N., Afanasova A., Romashev A., Aburova V., Prokhorova E. Extraction of low-dimensional structures of noble and rare metals from carbonaceous ores using low-temperature and energy impacts at succeeding stages of raw material transformation. *Minerals*. 2023;13(1):84.
https://doi.org/10.3390/min13010084
27. Bulaev A., Melamud V., Boduen A. Bioleaching of non-ferrous metals from arsenic-bearing sulfide concentrate. *Diffusion and Defect Data. Pt.B: Solid State Phenomena*. 2020;299:1064—1068.
https://doi.org/10.4028/www.scientific.net/SSP.299.1064
28. Bulaev A.G, Boduen A.Ja., Ukraincev I.V. Biooxidation

of persistent gold-containing concentrate of the Bestobe deposit. *Obogashhenie rud*. 2019;6:9—15. (In Russ.). https://doi.org/10.17580/or.2019.06.02
Булаев А.Г, Бодуэн А.Я., Украинцев И.В. Биоокисление упорного золотосодержащего концентрата месторождения Бестобе. *Обогащение руд*. 2019;6: 9—15. https://doi.org/10.17580/or.2019.06.02

29. Bulaev A., Boduen A. Carbon sources as a factor determining the resistance of microbial population oxidizing sulfide concentrate biooxidation to thermal stress. *Minerals*. 2021;12:110. https://doi.org/10.3390/min12020110
30. Marsden J., House I. The chemistry of gold extraction. 2006. SME. 682 p.
31. Dyson D., Yopps S., Langhans J., Dimov S., Brian Hart. Near-technical limit gold recovery from a double refractory carlin-type ore after pre-treatment by high-temperature pressure oxidation. *Mining, Metallurgy & Exploration*. 2022;39:1563—1570. https://doi.org/10.1007/s42461-022-00638-5
32. Seisembayev R.S., Kozhakhmetov S.M., Kvyatkovsky S.A., Semenova A.S. Extraction of gold from refractory gold-bearing ores by means of reducing pyrometallurgical selection. *Metallurgist*. 2020;64(7-8):788—795. https://doi.org/10.1007/s11015-020-01055-z
33. Elkina Y., Melamud V. Effect of carbon sources on pyrite-arsenopyrite concentrate biooxidation and growth of microbial population in stirred tank reactors. *Microorganisms*. 2021;9:2350. https://doi.org/10.3390/microorganisms9112350
34. Ahtiainen R., Lundström M., Liipo J. Preg-robbing verification and prevention in gold chloride-bromide leaching. *Minerals Engineering*. 2018;128:153—159. https://doi.org/10.1016/j.mineng.2018.08.037
35. Ofori-Sarpong G., Osseo-Asare K. Preg-robbing of gold from cyanide and non-cyanide complexes: Effect of fungi pretreatment of carbonaceous matter. *International Journal of Mineral Processing*. 2013;119:27—33. https://doi.org/10.1016/j.minpro.2012.12.007
36. Adams M.D., Burger A.M. Characterization and blinding of carbonaceous preg-robbers in gold ores. *Minerals Engineering*. 1998;11(10):919—927. https://doi.org/10.1016/S0892-6875(98)00079-X
37. Zalesov M.V., Grigoreva V.A., Trubilov V.S., Boduen A.Ya. Designing of engineering solutions to enhance efficiency of high-copper gold-bearing ore processing. *Gornaya promyshlennost'*. 2021;5:51—56. (In Russ.). https://doi.org/10.30686/1609-9192-2021-5-51-56
Залесов М.В., Григорьева В.А., Трубилов В.С., Бодуэн А.Я.. Разработка технических решений для повышения эффективности переработки высокомедистой золотосодержащей руды. *Горная промышленность*. 2021;5:51—56. https://doi.org/10.30686/1609-9192-2021-5-51-56
38. Lee S., Sadri F., Ghahreman A. Enhanced gold recovery from alkaline pressure oxidized refractory gold ore after its mechanical activation followed by thiosulfate leaching. *Journal of Sustainable Metallurgy*. 2022;8:186—196. https://doi.org/10.1007/s40831-021-00476-7
39. Kotljar Ju.A., Meretukov M.A., Strizhko L.S. Metallurgy of precious metals. Vol. 1. Moscow: Ruda i metally, 2005. 432 p.
Котляр Ю.А., Меретуков М.А., Стрижко Л.С. Металлургия благородных металлов. Т. 1. М.: Руда и металлы, 2005. 432 с.
40. Xie Feng, Chen J., Jian W., We W. Review of gold leaching in thiosulfate-based solutions. *Transactions of Nonferrous Metals Society of China* (Eng. Ed.). 2021;31(11):3506—3529. https://doi.org/10.1016/S1003-6326(21)65745-X
41. Wang J., Xie F., Wang W., Bai Y., Fu Y., Dreisinger D. Eco-friendly leaching of gold from a carbonaceous gold concentrate in copper-citrate-thiosulfate solutions. *Hydrometallurgy*. 2019;105204. https://doi.org/10.1016/j.hydromet.2019.10520
42. Liu X., Jiang T., Xu B., Zhang Y., Li Q., Yang Y., He Y. Thiosulphate leaching of gold in the $Cu—NH_3—S_2O_3—H_2O$ system: An updated thermodynamic analysis using predominance area and species distribution diagrams. *Minerals Engineering*. 2021;151:106336. https://doi.org/10.1016/j.mineng.2020.106336
43. Qiang Y., Mei L., Zhong Y., Jin Y. The oxidation pretreatment of a sulfidic refractory gold ore with pyrolusite. *Advanced Materials Research*. 2012;454: 285—291. https://doi.org/10.4028/www.scientific.net/AMR.550-553.2891
44. Lichter J.K.R., Davey G. Selection and sizing of ultrafine and stirred grinding mills. Mineral Processing Plant Design, Practice and Control. 2002. 1807 p.
45. Ljubetic K., Liu W. limitations of gold leaching in ferric chloride media. Pt. I: Batch reactor studies. *Minerals Engineering*. 2022;178: 107397. https://doi.org/10.1016/j.mineng.2022.107397
46. Deschênes G. Advances in the cyanidation of gold. In: *Gold Ore Processing*. 2016. P. 429—445. https://doi.org/10.1016/b978-0-444-63658-4.00026-8
47. Dosmukhamedov N., Kaplan V., Zholdasbay E., ArgynA.,

Kuldeyev E., Koishina G., Tazhiev Y. Chlorination treatment for gold extraction from refractory gold-copper arsenic-bearing concentrates. *Sustainability*. 2022;14:11019. https://doi.org/10.3390/su141711019

48. González-Anaya J.A., Nava-Alonso F., Pecina-Treviño E.T. Gold recovery optimization of a refractory concentrate by ultrafine grinding — A laboratory study. *Mining, Metallurgy & Exploration*. 2011; 28(2):94—101. https://doi.org/10.1007/bf03402394
49. Qin H., Guo X., Tian Q., Yu D., Zhang L. Recovery of gold from sulfide refractory gold ore: Oxidation roasting pretreatment and gold extraction. *Minerals Engineering*. 2021;164:106822. https://doi.org/10.1016/j.mineng.2021.106822
50. Ofori-Sarpong G., Osseo-Asare K. Preg-robbing of gold from cyanide and non-cyanide complexes: Effect of fungi pretreatment of carbonaceous matter. *International Journal of Mineral Processing*. 2013;119:27—33. https://doi.org/10.1016/j.minpro.2012.12.007
51. Jakhontova L.K., Grudev A.P. On the mechanism of arsenopyrite oxidation. *Novye dannye o mineralakh SSSR*. 1973;22:172—181. (In Russ.).
    Яхонтова Л.К., Грудев А.П. О механизме окисления арсенопирита. *Новые данные о минералах СССР*. 1973;22:172—181.
52. Plaksin I.N. Hydrometallurgy. Selected works. Moscow: Nauka, 1972. 278 p. (In Russ.).
    Плаксин И.Н. Гидрометаллургия. Избранные труды. М.: Наука. 1972. 278 с.
53. Vasiliev A.A. Development of technology for processing gold-containing finely ground raw materials using atmospheric oxidation: Abstract of dissertation of Cand. Sci. (Eng.). Irkutsk: Irgiredmet, 2011. (In Russ.).
    Васильев А.А. Разработка технологии переработки золотосодержащего тонкоизмельченного сырья с использованием атмосферного окисления: Автореферат дис. канд. техн. наук. Иркутск: Иргиредмет, 2011.
54. Rabieh A., Eksteen J.J., Albijanic B. The effect of grinding chemistry on cyanide leaching of gold in the presence of pyrrhotite. *Hydrometallurgy*. 2017;173:115—124. https://doi.org/10.1016/j.hydromet.2017.08.013
55. Hammerschmidt J., Güntner J., Kerstiens B. Roasting of gold ore in the circulating fluidized-bed technology. In: *Gold Ore Processing* (Second Edition). 2016. P. 393—409. https://doi.org/10.1016/B978-0-444-63658-4.00024-4
56. Nanthakumar B., Pickles C. A., Kelebek S. Microwave pretreatment of a double refractory gold ore. *Minerals Engineering*. 2017;20 (11):1109—1119. https://doi.org/10.1016/j.mineng.2007.04.003
57. Amankwah R.K., Pickles C.A. Microwave roasting of a carbonaceous sulphidic gold concentrate. *Minerals Engineering*. 2009;22(13):1095—1101. https://doi.org/10.1016/j.mineng.2009.02.012
58. Liu X., Li Q., Zhang Y., Jiang T., Yang Y., Xu B., He Y. Improving gold recovery from a refractory ore via Na_2SO_4 assisted roasting and alkaline Na_2S leaching. *Hydrometallurgy*. 2019;185:133—141. https://doi.org/10.1016/j.hydromet.2019.02.008
59. Zhang S.H., Zheng Y.J., Cao P., Li C.H., Lai S.Z., Wang X.J. Process mineralogy characteristics of acid leaching residue produced in low-temperature roasting-acid leaching pretreatment process of refractory gold concentrates. *International Journal of Minerals, Metallurgy, and Materials*. 2018; 25:1132—1139. https://doi.org/10.1007/s12613-018-1664-x
60. Ubaldini S., Veglio F., Fornari P., Abbruzzese C. Process flow-sheet for gold and antimony recovery from stibnite. *Hydrometallurgy*. 2000; 57 (3): 187—199. https://doi.org/10.1016/S0304-386X(00)00107
61. Celep O., Alp İ., Paktunç D., Thibault Y. Implementation of sodium hydroxide pretreatment for refractory antimonial gold and silver ores. *Hydrometallurgy*. 2011;108(1-2):109—114. https://doi.org/10.1016/j.hydromet.2011.03.005
62. Celep O., Yazici E.Y. Ultra fine grinding of silver plant tailings of refractory ore using vertical stirred media mill. *Transactions of the Nonferrous Metals Society of China*. 2013;23(11):3412—3420. https://doi.org/10.1016/S1003-6326(13)62882-4
63. Guzman I., Thorpe S.J., Papangelakis V.G. Redox potential measurement during pressure oxidation (POX) of a refractory gold ore. *Canadian Metallurgical Quarterly*. 2018;57(4):382—389. https://doi.org/10.1080/00084433.2017.1386363
64. Konadu K.T., Mendoza D.M., Huddy R.J., Harrison S.T., Kaneta T., Sasaki K. Biological pretreatment of carbonaceous matter in double refractory gold ores: A review and some future considerations. *Hydrometallurgy*. 2020;196:105434. https://doi.org/10.1016/j.hydromet.2020.105434

Information about the authors

Viktoriya A. Grigoreva – Engineer-Technologist of the Hydrometallurgy Department, JSC NPO "RIVS".
https://orcid.org/0000-0002-3039-1925
E-mail: viktoriia.grigoreva98@mail.ru

Anna Ya. Boduen – Cand. Sci. (Eng.), Director of the Hydrometallurgy Department, JSC NPO "RIVS".
https://orcid.org/0000-0003-3580-4394
E-mail: bodyen-anna@mail.ru

Информация об авторах

Виктория Александровна Григорьева – инженер-технолог 1-й категории департамента гидрометаллургии АО «НПО «РИВС».
https://orcid.org/0000-0002-3039-1925
E-mail: viktoriia.grigoreva98@mail.ru

Анна Ярославовна Бодуэн – к.т.н., директор департамента гидрометаллургии АО «НПО «РИВС».
https://orcid.org/0000-0003-3580-4394
E-mail: bodyen-anna@mail.ru

Contribution of the authors

V.A. Grigoreva – work with literature, analysis, accumulation and systematization of data, preparation of graphic material, writing the manuscript, manuscript design.

A.Ya. Boduen – creation and validation of the concept of the work (formulation of the idea), annotation of data, formulation of the conclusion, revision of the manuscript text.

Вклад авторов

В.А. Григорьева – работа с литературой, анализ, аккумулирование и систематизация данных, подготовка графического материала, написание текста рукописи, оформление рукописи.

А.Я. Бодуэн – создание и обоснование концепции работы (формулирование идеи), аннотирование данных, формулировка заключения, редактирование текста рукописи.

The article was submitted 18.05.2023, revised 24.09.2023, accepted for publication 25.09.2023

Статья поступила в редакцию 18.05.2023, доработана 24.09.2023, подписана в печать 25.09.2023

UDC 539.261, 620.187, 691.75
https://doi.org/10.17073/0021-3438-2023-6-35-43

Research article
Научная статья

Effect of severe plastic deformation on the structure and properties of the Zn–1%Li–2%Mg alloy

V.D. Sitdikov[1,2], **E.D. Khafizova**[2,3], **M.V. Polenok**[2,3]

[1] **LLC RN-BashNIPIneft**
86/1 Lenina Str., Ufa 450006, Russia

[2] **Institute of Physics of Molecules and Crystals of Ufa Research Center of the Russian Academy of Sciences**
151 Oktyabrya Prosp., Ufa 450075, Russia

[3] **Ufa University of Science and Technologies**
32 Zaki Validi Str., Ufa 450076, Russia

✉ Vil' D. Sitdikov (svil@ugatu.su, SitdikovVD@bnipi.rosneft.ru)

Abstract: Through the optimization of processing parameters, including pressure, temperature, and deformation degree, a high pressure torsion (HPT) regime was identified. This regime allows for the creation of a unique microstructure in the biodegradable Zn–1%Li–2%Mg alloy, which exhibits exceptional physical and mechanical properties. Following 10 revolutions of HPT treatment (resulting in an accumulated deformation degree, $\gamma = 571$) at the temperature of 150 °C and an applied pressure of 6 GPa, the Zn–1%Li–2%Mg alloy displayed notable mechanical characteristics, including a high yield strength (~385 MPa), ultimate tensile strength (~490 MPa), and ductility (44 %) during tensile tests. To elucidate the underlying reasons for these remarkable mechanical properties, an examination of the alloy's microstructure was conducted employing electron microscopy and X-ray phase analysis (XPA). The study revealed the formation of a distinct microstructure characterized by alternating bands of the α-phase Zn, a mixture of Zn and ~$LiZn_3$ phases, as well as the α-phase Zn containing Mg_2Zn_{11} particles, as a consequence of HPT treatment. Additionally, it was observed that HPT treatment induced a dynamic strain aging process, leading to the precipitation of Zn particles in the $LiZn_3$ phase and the precipitation of Mg_2Zn_{11} and β-$LiZn_4$ particles in the Zn phase. These precipitated particles exhibited a nearly spherical shape. The application of the XPA method helped to confirm that the Zn phase becomes the predominant phase during HPT treatment, and microscopy data showed the formation of an ultra-fine grained (UFG) structure within this phase. A comprehensive analysis of the hardening mechanisms, based on the newly acquired microstructural insights, revealed that enhanced strength and ductility of the Zn–1%Li–2%Mg UFG alloy can be attributed primarily to the effects of dispersion, grain boundary, and hetero-deformation-induced hardening, including dislocation strengthening.

Keywords: zinc alloy, severe plastic deformation, strength, ductility, microstructure, phase composition, *X*-ray diffraction analysis, hardening mechanisms.

Acknowledgments: The research was conducted with the support of the Russian Science Foundation Grant No. 23-29-00667, https://rscf.ru/project/23-29-00667

For citation: Sitdikov V.D., Khafizova E.D., Polenok M.V. Effect of severe plastic deformation on the structure and properties of the Zn–1%Li–2%Mg alloy. *Izvestiya. Non-Ferrous Metallurgy.* 2023;29(6):35–43.
https://doi.org/10.17073/0021-3438-2023-6-35-43

Влияние интенсивной пластической деформации на структуру и свойства сплава Zn–1%Li–2%Mg

В.Д. Ситдиков[1,2], **Э.Д. Хафизова**[2,3], **М.В.Поленок**[2,3]

[1] **ООО «РН-БашНИПИнефть»**
450006, Россия, Республика Башкортостан, г. Уфа, ул. Ленина, 86/1

[2] **Институт физики молекул и кристаллов**
Уфимского научного центра Российской академии наук
450075, Россия, Республика Башкортостан, г. Уфа, пр-т Октября, 151

[3] **Уфимский университет науки и технологий**
450076, Россия, Республика Башкортостан, г. Уфа, ул. Заки Валиди, 32

✉ Виль Даянович Ситдиков (svil@ugatu.su, SitdikovVD@bnipi.rosneft.ru)

Аннотация: Путем оптимизации параметров процессинга (давление, температура, степень деформации) найден режим интенсивной пластической деформации кручения (ИПДК), позволяющий сформировать в биоразлагаемом сплаве Zn–1%Li–2%Mg необычную микроструктуру, проявляющую уникальные физико-механические свойства. Так, после 10 оборотов ИПДК (степень накопленной деформации $\gamma = 571$), реализованной при температуре 150 °C и приложенном давлении 6 ГПа, сплав Zn–1%Li–2%Mg при испытаниях на растяжение продемонстрировал высокие показатели предела текучести (~385 МПа), предела прочности (~ 490 МПа) и пластичности (44 %). Для объяснения причин уникальных механических характеристик данного материала проанализирована его микроструктура методами электронной микроскопии и рентгенофазового анализа (РФА). Показано, что в сплаве в результате ИПДК формируется особая микроструктура, состоящая из чередующихся полос α-фазы Zn, смеси фаз Zn и ~$LiZn_3$, а также α-фазы Zn, содержащей частицы Mg_2Zn_{11}. Установлено, что при обработке ИПДК также реализуется процесс динамического старения, в результате которого в фазе ~$LiZn_3$ выпадают частицы Zn, а в фазе Zn – Mg_2Zn_{11} и β-$LiZn_4$. При этом показано, что эти частицы по форме близки к сфере. Методом РФА также установлено, что при обработке ИПДК основной становится фаза Zn, в которой, по данным микроскопии, формируется ультрамелкозернистая (УМЗ) структура. Анализ механизмов упрочнения, основанный на полученных новых сведениях о микроструктуре, показал, что основными причинами повышения прочности и пластичности УМЗ-сплава Zn–1%Li–2%Mg являются воздействия дисперсионного, зернограничного и гетеродеформационного типов упрочнения, включая дислокационный тип.

Ключевые слова: цинковый сплав, интенсивная пластическая деформация, прочность, пластичность, микроструктура, фазовый состав, рентгеноструктурный анализ, механизмы упрочнения.

Благодарности: Исследование выполнено за счет гранта Российского научного фонда № 23-29-00667, https://rscf.ru/project/23-29-00667

Для цитирования: Ситдиков В.Д., Хафизова Э.Д., Поленок М.В. Влияние интенсивной пластической деформации на структуру и свойства сплава Zn–1%Li–2%Mg. *Известия вузов. Цветная металлургия*. 2023;29(6):35–43.
https://doi.org/10.17073/0021-3438-2023-6-35-43

Introduction

In recent years, there has been a growing focus among specialists on research aimed at developing and optimizing the physical and mechanical properties of new biodegradable zinc-based alloys for medical applications [1—5]. These materials possess the unique characteristic of complete dissolution within the body, obviating the need for repeated surgical interventions to remove implanted devices [6; 7].

Zinc, as a base material, is well-known for its relatively low ultimate tensile strength (σ_{ut} ~ 34 MPa) and low ductility (δ ~ 1.2 %) [8]. Consequently, substantial strengthening measures are required to ensure that the material meets the stringent clinical trial criteria for biodegradable stents. These criteria demand an ultimate tensile strength exceeding 300 MPa and a minimum ductility of 15 % [6]. To achieve these specifications, a range of techniques is employed, including alloying methods involving various impurity elements (such as Li, Mg, Mn, Ca, Cu), heat treatments, and different plastic deformation schemes [9—11].

Specifically, a study referenced in [10] established that the ultimate strength of zinc can be substantially enhanced, reaching 213 MPa, by alloying it with 0.8 wt.% of Li. The authors further demonstrated that a combination of alloying and extrusion processes can elevate the ultimate strength of the same alloy (Zn—0.8 wt.%[1] Li) to ~ 500 MPa, placing it on par with the strength level of stainless steel. Moreover, the study discovered that additional alloying of the Zn—Li alloy with Mg, followed by 4 cycles of hot extrusion, can push the ultimate tensile strength to a remarkable 647 MPa [10], marking an all-time high for zinc alloys.

Conversely, another study [12] demonstrated that by increasing the degree of zinc alloying with lithium to 6 at.% and employing a different deformation scheme (warm rolling), samples with enhanced ultimate strength (560 MPa) can be obtained. However, it's essential to note that in all of these studies [10; 12], the zinc alloys exhibited extremely low ductility, not exceeding 5 %. This limitation significantly restricts the range of potential applications for these materials.

In pursuit of enhancing the properties of zinc alloys, researchers are actively exploring novel approaches and thermomechanical processing techniques. These methods include severe plastic deformation (SPD) processes, such as Equal Channel Angular Pressing (ECAP) and High-Pressure Torsion (HPT), as mentioned in [13; 14]. The primary objective of these deformation schemes is to enhance the ductility of zinc alloys, while simultaneously refining the grain structure to the nanometer level, thereby creating high-strength materials. For example, as indicated in [15], the application of HPT treatment, even to pure zinc, results in a notable increase in ultimate strength, reaching 140 MPa, and an impressive ductility of 40 %. In a related study [14], it was observed that subjecting a doped zinc alloy, Zn—0.6Mg—0.1Ca, to ECAP (12 cycles) elevated its ultimate tensile strength to 300 MPa, along with an improved ductility of 20 %.

The paper referenced in [13] details the development of a high-strength alloy, boasting an ultimate tensile strength of 318 MPa and a remarkable ductility of 34 %, following four ECAP cycles of the Zn—1Cu—0.5Mg alloy. Furthermore, the authors demonstrated that by increasing the Cu doping level in the alloy to 3 % while applying the same processing methods, the ultimate tensile strength (σ_{ut}) rise to 358 MPa, was elevated to 358 MPa, and the ductility (δ) increased to an impressive 51 %.

The concise review highlights the capability to significantly enhance the ductility of zinc alloys by adjusting the degree of impurity element doping and optimizing the conditions and methods of SPD. Consequently, this paper aims to identify the specific conditions, including pressure, temperature, and degree of deformation, required for the high-pressure torsion method to create a unique ultra-fine-grained (UFG) structure in the Zn—1Li—2Mg alloy. This UFG structure is integral to achieving not only high strength but also exceptionally high ductility in the material.

Materials and methods

The research involved the casting of high-purity Zn—1Li—2Mg bioresorbable zinc alloy ingots. These ingots were then subjected to HPT to achieve optimal mechanical properties. The HPT was carried out at a pressure of 6 GPa, with the upper striker rotating at a speed of 1 revolution per minute. This resulted in the formation of disk-shaped samples, each 1.1 mm thick and with a radius of 10 mm. Furthermore, the level of deformation was adjusted by varying the number of HPT revolutions, ranging from 0.5 to 10, and the temperature, which was set between 27 °C and 150 °C. The accumulated deformation degree was calculated using the formula [16]:

$$\gamma = 2\pi Nr/h,$$

where h and r represent the thickness and the radius of the sample, respectively, mm, N is the number of revolutions applied in the HPT process.

To determine the mechanical properties of the alloy, small flat samples with a gauge length of 4 mm, a thickness of 1.0 mm, and a width of 1.0 mm were tested for elongation. These tests were conducted using a specialized testing machine, the Instron 8801 (UK). To assess the ductility of the alloy, the total extension of the sample was calculated using the following formula:

$$\delta = \Delta l \cdot 100\,\%/l,$$

where l is the length of the sample's gauge part, mm, Δl is the in the length of the sample's gauge part after the sample's destruction, mm.

During the alloy elongation tests, the incremental step was set at 10^{-4} mm, and the deformation rate was maintained at $4 \cdot 10^{-4}$ mm/s. Mechanical tests were conducted at least three times for each structural state of the alloy to ensure consistent and reliable results.

The microstructure of the alloy was analyzed using a Q250 scanning electron microscope (SEM) (Thermo Fisher Scientific, USA). The SEM operated with

---

[1] Hereinafter the content of alloy components is given in wt.%.

an accelerating voltage of electrons reaching 25 kV. The electron beam diameter was adjustable within the range of 1 to 5 μm, and the focal length was varied within the 8—10 mm range. During the analysis, the pressure in the chamber did not exceed 10^{-3} Pa.

To estimate the parameters of the alloy's fine structure, the *X*-ray diffraction (XRD) patterns were recorded and analyzed using a D8 Advance diffractometer (Bruker, Germany) in Bragg-Brentano geometry. The *X*-ray diffraction patterns were captured in the continuous mode at a rate of 1°/min, covering angles $2\theta = 15°\div155°$. The *X*-ray radiation source used was CuK_α, generated from a wide-focus *X*-ray tube with settings of $U = 40$ kV and $I = 40$ mA.

Qualitative *X*-ray phase analysis (XPA) was carried out using the EVAplus program (www.bruker.com) with reference to the PDF-2 diffractometric database. Additionally, quantitative analysis was performed to determine the phase ratios with the identified phases using the Rietveld method in TOPAS v.4.2 (www.bruker.com) [17].

Results and discussion

The results of mechanical tensile tests demonstrated that the parent Zn—1Li—2Mg alloy had the following properties: a yield strength σ_y ~ 150 MPa, an ultimate tensile strength σ_{ut} ~ 155 MPa, and a ductility $\delta \le 0.5$ % (See Table). HPT treatment at the room temperature with 10 revolutions ($\gamma = 571$) significantly improved the alloy's mechanical properties, increasing σ_y to 330 MPa and σ_{ut} to 409 MPa, while also enhancing ductility to 47 %.

By further varying the temperature and HPT degree, a specific regime (150 °C, 10 revolutions, $\gamma = 571$), at which the alloy exhibited remarkable mechanical properties (σ_y ~ 385 MPa, σ_{ut} ~ 490 MPa, and $\delta = 44$ %), was identified. Notably, during the initial HPT stages (up to 0.5—1.0 revolutions, $\gamma = 28.5\div57.1$), the samples also exhibited increased strength, reaching up to 500 MPa, but their ductility did not surpass 7 %.

Mechanical properties of the Zn–Li–2Mg alloy in the initial state and after HPT treatment

Механические свойства сплава Zn–1Li–2Mg в исходном состоянии и после обработки

State	σ_y, MPa	σ_{ut}, MPa	δ, %
Initial	149	155	0.4
HPT 10 rev., $\gamma = 571$, $t = 27$ °C	330	409	47
HPT 10 rev., $\gamma = 571$, $t = 150$ °C	385	490	44

To investigate the simultaneous increase in strength and ductility of the studied alloy, a microstructure analysis using SEM and XPA methods was conducted.

In the initial (cast) state, the alloy's microstructure exhibits both light and dark regions (Fig. 1, *a*, *b*). Based on the Zn—Li phase diagram [18] and the characteristics of SEM and XPA methods, we identify the light regions (oval shape and layered structure) as a mixture of Zn and β-$LiZn_4$ eutectic phases, while the dark regions correspond to the primary β-$LiZn_4$ phase. At the interface between these phases, bright regions (inset in Fig. 1, *b*) are occasionally observed, which, according to elemental mapping data, indicate the presence of the $MgZn_2$ phase. Furthermore, a detailed analysis of impurity atom distribution was conducted through linear mapping along the yellow line (Fig. 1, *c*). The results, showing the mass distribution of Mg and Zn atoms along the selected line, are depicted in Fig. 1, *d*. The graph reveals a slight increase in Mg atom content in the dark regions. According to the Zn—Mg phase diagram at 2 wt.% Mg in Zn at room temperature, the mixture should contain the Zn and Mg_2Zn_{11} phases [19]. However, our XPA data, as presented below, did not detect the Mg_2Zn_{11} phase in the initial alloy state. This suggests that, in addition to the $MgZn_2$ phase, Mg atoms may exist as impurities within the primary β-$LiZn_4$.

After HPT treatment at both room temperature and 150 °C (Fig. 2, *a*, *b*), significant changes occur in the microstructure of the analyzed alloy, leading to the emergence of a banded structure. According to XPA data and existing literature [13, 20], this structure is formed by Zn phases, as well as mixtures of α-Zn + ~$LiZn_3$ and α-Zn + Mg_2Zn_{11}. Magnified images of the detected phases in the post-HPT states are presented in Fig. 2, *c*, *d*. Following HPT at 150 °C, spherically shaped Mg_2Zn_{11} phase particles (dark regions) are observed falling out in bright bands that correspond to the Mg_2Zn_{11} phase (upper right inset in Fig. 2, *d*), in agreement with prior research [7; 13]. After HPT treatment at room temperature, the structure retains remnants of lamellar eutectics, consisting of alternating light Zn lamellae and dark Mg_2Zn_{11} lamellae (inset in Fig. 2, *c*) with an average thickness of 360 nm and 140 nm, respectively (Fig. 2, *c*). Meanwhile, the diameter of spherical Mg_2Zn_{11} particles in the Zn phase was ~300 nm.

According to the sources [21; 22], warm rolling of the Zn—Li alloy results in the formation of string-like β-$LiZn_4$ particles, creating a fine-scale network in the Zn phase, with needle-like Zn particles precipitating in the β-$LiZn_4$ phase. Our research revealed that HPT

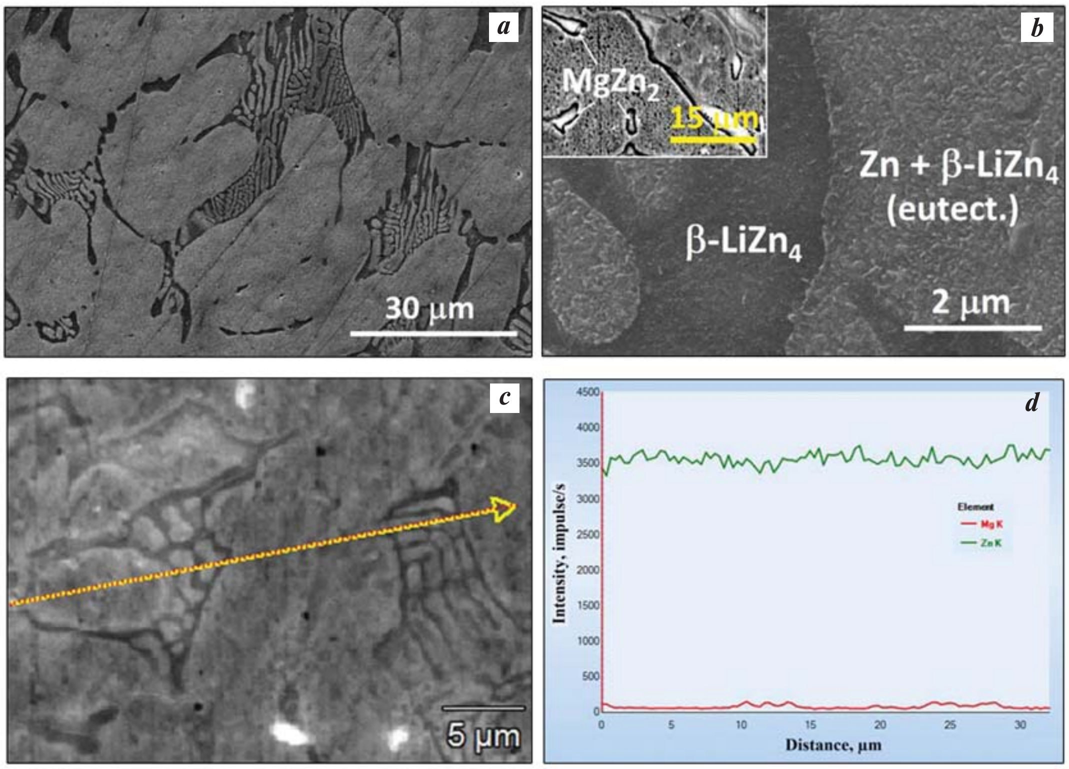

Fig. 1. SEM images of the Zn–1Li–2Mg initial alloy microstructure

a – magnification 4000$^{\times}$, ***b*** – 50 000$^{\times}$, ***c*** – linear mapping region, ***d*** – distribution of Mg and Zn atoms along the line highlighted in Fig. ***c***

Рис. 1. РЭМ-изображения микроструктуры Zn–1Li–2Mg исходного сплава

a – увеличение 4000$^{\times}$, ***b*** – 50 000$^{\times}$, ***c*** – участок проведения линейного картирования,
d – распределение атомов Mg и Zn вдоль выделенной на рис. ***c*** линии

treatment of the alloy leads to the precipitation of spherically shaped β-LiZn$_4$ particles in the Zn phase (inset in Fig. 2, *a*, *b*).

In the β-LiZn$_4$ phase, apart from the large cylindrical Zn particles, small spherical Zn particles (lower inset in Fig. 2, *c*) with a diameter of ~ 80 nm also precipitate. Similar-shaped precipitations were previously observed in the lightly doped Zn—0.8Li—0.1Mg alloy subjected to HPT [23]. Detailed analysis reveals that HPT treatment at room temperature is more effective in refining the grain structure of the Zn phase compared to HPT at 150 °C (see Fig. 2, *a*, *b* and insets). In the former case, the Zn phase consists of equiaxial nanoscale grains, with an average size of 360 nm after HPT at 27 °C, while it reaches 610 nm after HPT at 150 °C.

Figure 3 displays the *X*-ray diffraction patterns of the alloy in its initial (cast) state and after 10 revolutions of HPT ($\gamma = 571$) at different temperatures. Qualitative XPA analysis reveals responses related to Zn, ~LiZn$_3$, β-LiZn$_4$, Mg$_2$Zn$_{11}$, and MgZn$_2$ phases. in the *X*-ray diffraction patterns of the zinc alloy. Quantitative XPA analysis indicates that in the initial state, the Zn phase constitutes 31.3 % of the alloy, while the fractions of ~LiZn$_3$, β-LiZn$_4$, and MgZn$_2$ phases are 45, 11.8, and 11.9 %, respectively. After 10 revolutions of HPT ($\gamma = 571$) at $t = 27$ °C, the Zn content significantly increases to 52.4 %, while the ~LiZn$_3$ phase decreases to 21.7 %. Furthermore, the fractions of β-LiZn$_4$ and MgZn$_2$ phases decrease to 7.2 % and 0.5 %, respectively. Notably, in contrast to the initial alloy, HPT treatment at this temperature results in the formation of the Mg$_2$Zn$_{11}$ phase, with a relatively high concentration of 18.2 % in the alloy.

When the deformation temperature is increased to 150 °C and 10 revolutions of HPT processing are applied ($\gamma = 571$), the mass fractions of Zn and Mg$_2$Zn$_{11}$ phases further increase to 57.7 % and 21.5 %, respectively. Simultaneously, the contents of other phases continue to decrease: ~LiZn$_3$ (16.3 %), β-LiZn$_4$ (4.2 %), and MgZn$_2$ (0.3 %). Quantitative phase ratios were determined by analyzing the *X*-ray diffraction patterns using the Rietveld method. An example of the processed region of the alloy's *X*-ray diffraction pattern after 10 revolutions of HPT ($\gamma = 571$, $t = 150$ °C) is shown in Fig. 3, *b*.

The unique mechanical properties observed in samples subjected to HPT can be attributed to hardening

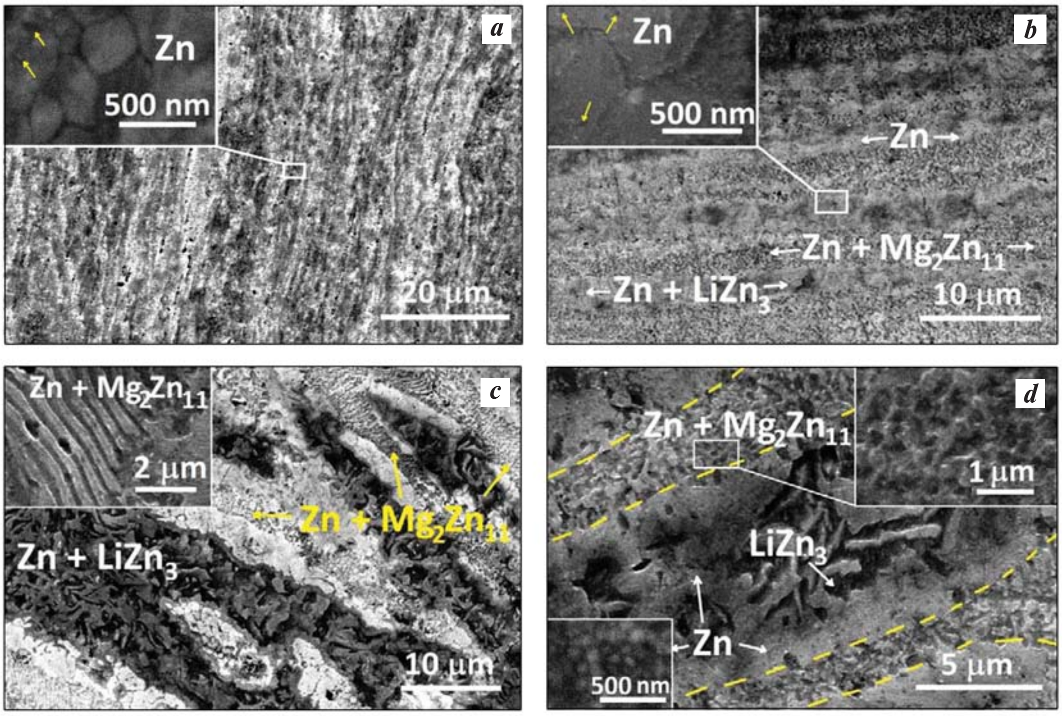

Fig. 2. SEM images of the Zn–1Li–2Mg alloy microstructure after HPT treatment:
a – HPT ($t = 27$ °C, 10 rev., $\gamma = 571$), magnification 5000$^\times$, the insert shows the Zn phase;
b – HPT (150 °C, 10 rev., $\gamma = 571$), magnification 10 000$^\times$, the insert shows the Zn phase;
c – HPT ($t = 27$ °C, 10 rev., $\gamma = 571$), magnification 8000$^\times$, the insert shows Zn and Mg_2Zn_{11} phases;
d – HPT (150°C, 10 rev., $\gamma = 571$), magnification 20 000$^\times$, inserts show Zn and Mg_2Zn_{11} particles

Рис. 2. РЭМ-изображения микроструктуры сплава Zn–1Li–2Mg после обработки
a – ИПДК ($t = 27$ °C, 10 об., $\gamma = 571$), увеличение 5000$^\times$, на вставке – фаза Zn;
b – ИПДК (150 °C, 10 об., $\gamma = 571$), 10 000$^\times$, на вставке – фаза Zn;
c – ИПДК ($t = 27$ °C, 10 об., $\gamma = 571$), 8000$^\times$, на вставке – пластины фаз Zn и Mg_2Zn_{11};
d – ИПДК (150 °C, 10 об., $\gamma = 571$), 20 000$^\times$, на вставках – частицы Zn и Mg_2Zn_{11}

mechanisms, as supported by the microstructure analysis described earlier. SEM and XRD studies revealed the precipitation of Zn, β-$LiZn_4$, and Mg_2Zn_{11} particles during HPT treatment of the Zn-alloy. It was noted that at higher deformation temperatures, such as 150 °C, the quantity and size of these precipitates increase compared to room temperature HPT. This suggests increased diffusion processes' activity at elevated HPT temperatures, leading to more comprehensive dynamic. In general, it can be concluded that the dispersion mechanism significantly contributes to alloy hardening during HPT, and this effect intensifies with a higher precipitate content [3; 5].

Additionally, another hardening mechanism at play in the zinc alloy is grain boundary strengthening resulting from grain structure refinement. Grains ground to nanometer sizes not only enhance strength but can also increase the alloy's ductility by activating grain boundary sliding processes [25; 26]. This mechanism, well-documented in literature [25], is known to be the predominant superductility mechanism in UFG zinc alloys and is typically activated at grain sizes less than 1 µm.

In a study by [26], refining the grain structure of the Zn—22Al alloy to 700—900 nm using the ECAP method led to a remarkable increase in ductility, reaching 280 %. Our research has similarly shown that the primary phase in HPT treatment is zinc with nanometer-sized grains (Fig. 2, *a*, *b*), with an increased fraction of grain boundaries contributing to enhanced ductility. This suggests that the grain refinement in the zinc phase not only strengthens the alloy but also explains its improved ductility.

Another notable strengthening mechanism in UFG metallic materials is hetero-deformation induced hardening [27]. This mechanism is observed in metals and alloys where heterostructured materials form, comprising separate domains that vary significantly in strength. Extreme plastic deformations generate back stress within the material structure due to the superposition of forward and reverse stresses from hard and soft domains in

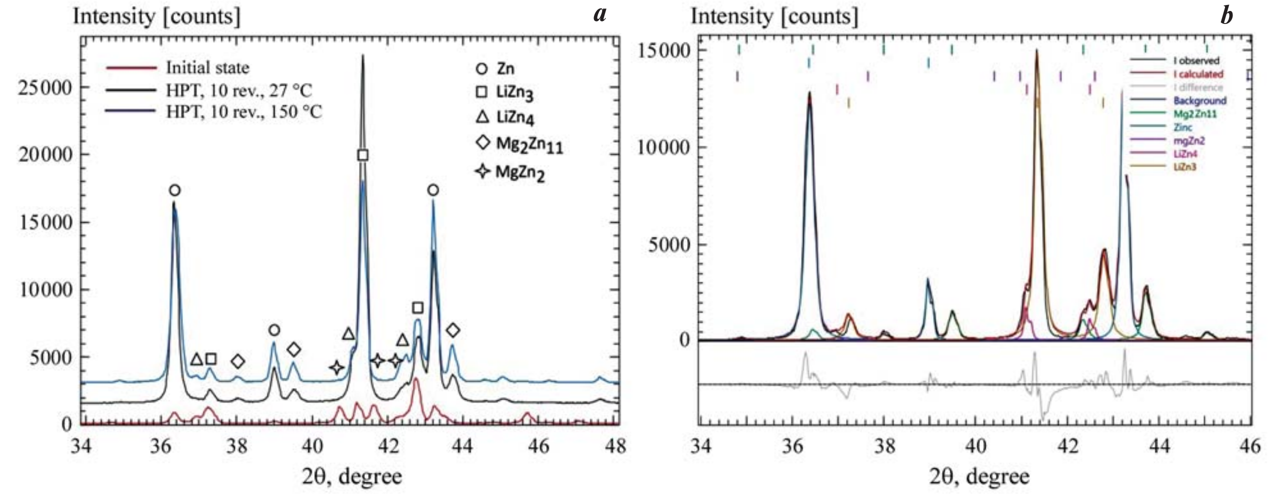

Fig. 3. *X*-ray diffraction patterns of the initial and HPT-processed alloys (***a***), as well as the analyzed section of the *X*-ray diffraction pattern after HPT treatment (10 rev., $\gamma = 571$, $t = 150$ °C) (***b***)

Рис. 3. Дифрактограммы исходного и ИПДК-обработанного сплавов (***a***), а также проанализированный участок дифрактограммы образца после ИПДК (10 об., $\gamma = 571$, $t = 150$ °C) (***b***)

the microstructure [27]. Long-range back stresses, created by clusters and pile-ups of dislocations, strengthen the soft domains, contributing to an overall increase in strength [27].

In cases where HPT is performed at high RPM, a band structure forms, including α-Zn phases, a mixture of α-Zn phases and the ~$LiZn_3$ phase, as well as the α-Zn phase with Mg_2Zn_{11} particles precipitating. These phases exhibit different microhardness levels and can be considered as soft and hard domains or phases. Our studies [23] have shown that the soft phase of Zn in the Zn—Li—Mg alloy is characterized by an increased dislocation density. Consequently, the mechanism of hetero-deformation induced hardening, which includes dislocation strengthening, is also an active force at high RPMs during HPT.

Conclusion

After optimizing the HPT parameters, a unique regime (pressure 6 GPa, temperature 150 °C, 10 revolutions, $\gamma = 571$) was discovered, resulting in the Zn—1Li—2Mg alloy exhibiting exceptional mechanical properties. These properties include a yield strength of ~385 MPa, an ultimate tensile strength of ~ 490 MPa, and ductility reaching 44 %.

Detailed analysis of the alloy's microstructure revealed the formation of a distinctive band structure. This structure comprises the α-Zn phase, a mixture of α-Zn phase and ~$LiZn_3$ phases, as well as the α-Zn phase with Mg_2Zn_{11} particles. Notably, Zn particles were found to precipitate in the ~$LiZn_3$ phase, while Mg_2Zn_{11} and β-$LiZn_4$ particles precipitated in the Zn phase. Additionally, the application of HPT treatment resulted in the formation of an UFG structure in the primary Zn phase.

The analysis of hardening mechanisms identified the key factors contributing to the enhanced strength of the Zn—1Li—2Mg alloy with a UFG structure. These mechanisms include dispersion, grain boundary strengthening, and hetero-deformation induced hardening, which involves dislocation strengthening. Moreover, the alloy's improved ductility can be attributed to the extremely small grain size of the Zn phase, which promotes the activation of grain boundary sliding processes.

References

1. Hernández-Escobar D., Champagne S., Yilmazer H., Dikici B., Boehlert C.J., Hermawan H. Current status and perspectives of zinc-based absorbable alloys for biomedical applications. *Acta Materialia*. 2019;(97):1—22. https://doi.org/10.1016/j.actbio.2019.07.034
2. Huang S., Wang L., ZhengY., Qiao L., Yan Y. In vitro degradation behavior of novel Zn—Cu—Li alloys: Roles of alloy composition and rolling processing. *Materials & Design*. 2021;(212):110288. https://doi.org/10.1016/j.matdes.2021.110288
3. Li W., Dai Y., Zhang D., Lin J., Biodegradable Zn—0.5Li alloys with supersaturated solid solution-aging treatment for implant applications. *Journal of Materials Research and Technology*. 2023;(24):9292—9305. https://doi.org/10.1016/j.jmrt.2023.05.136

4. Yang L., Li X., Yang L., Zhu X., Wang M., Song Z., Liu H.H., Sun W., Dong R., Yue J. Effect of Mg contents on the microstructure, mechanical properties and cytocompatibility of degradable Zn—0.5Mn—*x*Mg alloy. *Journal of Functional Biomaterials.* 2023;(14):195. https://doi.org/10.3390/jfb14040195
5. Ye L., Huang H., Sun C., Zhuo X., Dong Q., Liu H., Ju J., Xue F., Bai J., Jiang J. Effect of grain size and volume fraction of eutectic structure on mechanical properties and corrosion behavior of as-cast Zn—Mg binary alloys. *Journal of Materials Research and Technology.* 2022;(16):1673—1685. https://doi.org/10.1016/j.jmrt.2021.12.101
6. Yuan W., Xia D., Wu S., Zheng Y., Guan, Z., Rau J.V. A review on current research status of the surface modification of Zn-based biodegradable metals. *Bioactive Materials.* 2022;(7):192—216. https://doi.org/10.1016/j.bioactmat.2021.05.018
7. García-Mintegui C., Córdoba L.C., Buxadera-Palomero J., Marquina A., Jiménez-Piqué E., Ginebra M.P., Cortina J.L., Pegueroles M. Zn—Mg and Zn—Cu alloys for stenting applications: From nanoscale mechanical characterization to in vitro degradation and biocompatibility. *Bioactive Materials.* 2021;6(12):4430—4446. https://doi.org/10.1016/j.bioactmat.2021.04.015
8. Tong X., Zhang D., Zhang X., Su Y., Shi Z., Wang K., Lin J., Li Y., Lin J., Wen C. Microstructure, mechanical properties, biocompatibility, and in vitro corrosion and degradation behavior of a new Zn—5Ge alloy for biodegradable implant materials. *Acta Biomaterialia.* 2018;(82):197—204. https://doi.org/10.1016/j.actbio.2018.10.015
9. Yang H., Jia B., Zhang Z., Qu X., Li G., Lin W., Zhu D., Dai K., Zheng Y. Alloying design of biodegradable zinc as promising bone implants for load-bearing applications. *Nature Communications.* 2020;(11):401. https://doi.org/10.1038/s41467-019-14153-7
10. Li Zh., Shi Zh.-Zh., Hao Y., Li H., Zhang H., Liu X., Wang L.-N. Insight into role and mechanism of Li on the key aspects of biodegradable Zn—Li alloys: Microstructure evolution, mechanical properties, corrosion behavior and cytotoxicity. *Materials Science and Engineering: C.* 2020;(114):111049. https://doi.org/10.1016/j.msec.2020.111049
11. Ye L., Liu H., Sun C., Zhuo X., Ju J.; Xue F., Bai J., Jiang J., Xin Y. Achieving high strength, excellent ductility, and suitable biodegradability in a Zn—0.1Mg alloy using room-temperature ECAP. *Journal of Alloys and Compounds.* 2022;(926):166906. https://doi.org/10.1016/j.jallcom.2022.166906
12. Zhao S., McNamara C.T., Bowen P.K., Verhun N., Braykovich J.P., Goldman J., Drelich J.W. Structural characteristics and in vitro biodegradation of a novel Zn—Li alloy prepared by induction melting and hot rolling. *Metallurgical and Materials Transactions A.* 2017;(48): 1204—1215. https://doi.org/10.1007/s11661-016-3901-0
13. Liu H., Ye L., Ren K., Sun C., Zhuo X., Yan K., Ju J., Jiang J., Xue F., Bai J. Evolutions of $CuZn_5$ and Mg_2Zn_{11} phases during ECAP and their impact on mechanical properties of Zn—Cu—Mg alloys. *Journal of Materials Research and Technology.* 2022;(21):5032—5044. https://doi.org/10.1016/j.jmrt.2022.11.095
14. Huang H., Liu H., Wang L., Yan K., Li Y., Jiang J., Ma A., Xue F., Bai J. Revealing the effect of minor Ca and Sr additions on microstructure evolution and mechanical properties of Zn—0.6 Mg alloy during multi-pass equal channel angular pressing. *Journal of Alloys and Compounds.* 2020;(844):155923. https://doi.org/10.1016/j.jallcom.2020.155923
15. Polenok M.V., Khafizova E.D., Islamgaliev R.K. Influence of severe plastic deformation on the mechanical properties of pure zinc. *Frontier Materials & Technologies.* 2022;(3—2):25—31. https://doi.org/10.18323/2782-4039-2022-3-2-25-31
16. Valiev R.Z., Islamgaliev R.K., Alexandrov I.V. Bulk nanostructured materials from severe plastic deformation. *Progress Materials Science.* 2000;45(2):103—189. https://doi.org/10.1016/S0079-6425(99)00007-9
17. Rietveld H.M. A profile refinement method for nuclear and magnetic structures. *Journal of Applied Crystallography.* 1969;2(2):65—71. https://doi.org/10.1107/S0021889869006558
18. Pelton A. The Li—Zn (Lithium—Zinc) system. *Journal of Phase Equilibria.* 1991;(12):42—45. https://doi.org/10.1007/BF02663672
19. Liu S., Kent D., Doan N., Dargusch M., Wang G. Effects of deformation twinning on the mechanical properties of biodegradable Zn—Mg alloys. *Bioactive Materials.* 2018;4(1):8—16. https://doi.org/10.1016/j.bioactmat.2018.11.001
20. Zhang Y., Yan Y., Xu X., Lu Y., Chen L., Li D., Dai Y., Kang Y., Yu K., Investigation on the microstructure, mechanical properties, in vitro degradation behavior and biocompatibility of newly developed Zn—0.8%Li—(Mg, Ag) alloys for guided bone regeneration. *Materials Science and Engineering: C.* 2019;(99):1021—1034. https://doi.org/10.1016/j.msec.2019.01.120
21. Shi Z.Z., Gao X.X., Zhang H.J., Liu X.F., Li H.Y., Zhou C., Yin Y.X., Wang L.N. Design biodegradable Zn alloys: Second phases and their significant influences on alloy properties. *Bioactive Materials.* 2020;5(2):210—218. https://doi.org/10.1016/j.bioactmat.2020.02.010
22. Li Zh., Shi Zh.-Zh., Zhang H.-J., Li H.-F., Feng Y., Wang L.-N. Hierarchical microstructure and two-stage corro-

sion behavior of a high-performance near-eutectic Zn—Li alloy. *Journal of Materials Research and Technology.* 2021; 80:50—65. https://doi.org/10.1016/j.jmst.2020.10.076

23. Sitdikov V.D., Kulyasova O.B., Sitdikova G.F., Islamgaliev R.K., Yufeng J. Structural-phase transformations in a Zn—Li—Mg alloy subjected to severe plastic deformation by torsion. *Frontier Materials & Technologies.* 2022;(3—2): 44—55. https://doi.org/10.18323/2782-4039-2022-3-2-44-55
24. Zhuo X., Wu Y., Ju J., Liu H., Jiang J., Hu Z., Bai J., Xue F. Recent progress of novel biodegradable zinc alloys: from the perspective of strengthening and toughening. *Journal of Materials Research and Technology.* 2022;(17):244—269. https://doi.org/10.1016/j.jmrt.2022
25. Demirtas M., Yanar H., Saray O., Pürçek G. Room temperature superplasticity in fine/ultrafine-grained Zn—Al alloys with different phase compositions. *Defect and Diffusion Forum.* 2018;(85):72—77. https://doi.org/10.4028/www.scientific.net/ddf.385.72
26. Kumar P., Xu C., Langdon T.G. Mechanical characteristics of a Zn—22%Al alloy processed to very high strains by ECAP. *Materials Science and Engineering A.* 2006; (429): 324—328. https://doi.org/10.1016/j.msea.2006.05.044
27. Zhu Y.T., Wu X.L. Perspective on hetero-deformation induced (HDI) hardening and back stress. *Materials Research Letters.* 2019;(7): 393—398. https://doi.org/10.1080/21663831.2019.1616331

Information about the authors

Vil' D. Sitdikov – Dr. Sci. (Phys.-Math.), Expert of RN-BashNIPIneft LLC; Senior Researcher at the Institute of Physics of Molecules and Crystals of the Ufa Scientific Center of the Russian Academy of Sciences (IPMC USC RAS).
https://orcid.org/0000-0002-9948-1099
E-mail: svil@ugatu.su, SitdikovVD@bnipi.rosneft.ru

El'vira D. Khafizova – Cand. Sci. (Eng.), Senior Researcher of IPMC USC RAS; Associate Professor of the Department of Materials Science and Physics of Metals, Senior Researcher at the Research Laboratory "Metals and Alloys under Extreme Impacts", Ufa University of Science and Technologies.
https://orcid.org/0000-0002-4618-412X
E-mail: ela.90@mail.ru

Milena V. Polenok – Laboratory Assistant of IPMC USC RAS; Undergraduate, Research Engineer at the Research Laboratory "Metals and Alloys under Extreme Impacts", Ufa University of Science and Technologies.
https://orcid.org/0000-0001-9774-1689
E-mail: renaweiwei.179@mail.ru

Информация об авторах

Виль Даянович Ситдиков – д.ф.-м.н., эксперт ООО «РН-БашНИПИнефть»; ст. науч. сотрудник Института физики молекул и кристаллов Уфимского научного центра Российской академии наук (ИФМК УНЦ РАН).
https://orcid.org/0000-0002-9948-1099
E-mail: svil@ugatu.su, SitdikovVD@bnipi.rosneft.ru

Эльвира Динифовна Хафизова – к.т.н., ст. науч. сотрудник ИФМК УНЦ РАН; доцент кафедры материаловедения и физики металлов, ст. науч. сотрудник НИЛ «Металлы и сплавы при экстремальных воздействиях» Уфимского университета науки и технологий (УУНиТ).
https://orcid.org/0000-0002-4618-412X
E-mail: ela.90@mail.ru

Милена Владиславовна Поленок – лаборант ИФМК УНЦ РАН; инженер-исследователь НИЛ «Металлы и сплавы при экстремальных воздействиях» УУНиТ.
https://orcid.org/0000-0001-9774-1689
E-mail: renaweiwei.179@mail.ru

Contribution of the authors

V.D. Sitdikov – determined the purpose of the work, analyzed the experiments, wrote the article.

E.D. Khafizova – conducted *X*-ray phase analysis, conducted SEM analysis, participated in the discussion of the results.

M.V. Polenok – preparation of samples, carried out HPT processing, carried out mechanical tests, participated in the discussion of the results.

Вклад авторов

В.Д. Ситдиков – определение цели работы, анализ экспериментов, написание текста статьи.

Э.Д. Хафизова – проведение рентгенофазового и РЭМ анализов, участие в обсуждении результатов.

М.В. Поленок – подготовка образцов, проведение ИПДК-обработки и механических испытаний, участие в обсуждении результатов.

The article was submitted 10.07.2023, revised 20.09.2023, accepted for publication 25.09.2023

Статья поступила в редакцию 10.07.2023, доработана 20.09.2023, подписана в печать 25.09.2023

PHYSICAL METALLURGY AND HEAT TREATMENT / МЕТАЛЛОВЕДЕНИЕ И ТЕРМИЧЕСКАЯ ОБРАБОТКА

UDC 669.24; 620.196.5; 621.791.669
https://doi.org/10.17073/0021-3438-2023-6-44-53

Research article
Научная статья

Structure and properties of welds in electron beam welding of iron-chromium-nickel alloy EP718

S.L. Isaev[1], **D.A. Baranov**[1], **E.Yu. Shchedrin**[1], **V.S. Muratov**[2], **K.V. Nikitin**[2], **S.S. Zhatkin**[2]

[1] **JSC "UEC-Kuznetsov"**
29 Zavodskoe shosse, Samara 443022, Russia

[2] **Samara State Technical University**
244 Molodogvardeyskaya Str., Samara 443100, Russia

✉ Konstantin V. Nikitin (kvn-6411@mail.ru)

Abstract: This article presents the results of a study focused on the formation of structural characteristics and properties of welded joints in the EP718 alloy with a 13 mm thickness (accounting for a 3 mm technological substrate). The study explores variations in electron beam welding parameters, such as beam current and the speed of its movement across the specimen's surface, to determine the optimal welding mode for this alloy. This alloy is crucial in the production of high-pressure stators for aircraft engines, as the component operates under low-cycle loads at high stress levels, making its performance critical. Specimens that were welded with a beam speed (v) of 0.0042 m/s and a beam current (i) of 85 mA exhibited a minimum tensile strength of 1160 MPa. On the other hand, specimens welded with $v = 0.006$ m/s and $i = 65$ mA demonstrated a maximum tensile strength of 1270 MPa. However, it's noteworthy that specimens welded at 0.006 m/s with beam currents of 120 mA and 75 mA experienced fracture along the weld, while specimens welded at 0.006 m/s with a beam current of 65 mA and at 0.0042 m/s with a beam current of 85 mA exhibited fracture in the heat-affected zone at a distance of 0.5–3.0 mm from the weld. Examination of the structure of specimens welded at $v = 0.006$ and 0.0042 m/s and $i = 120$ mA, 75 mA, and 85 mA revealed expanded grain boundaries in the heat-affected zone. Consequently, the optimal welding mode was identified as having a beam speed of 0.006 m/s and a beam current of 65 mA. In this mode, no thickened grain boundaries were detected, and a maximum tensile strength of 1270 MPa was achieved.

Keywords: electron beam welding, heat resistant nickel alloys, heat affected zone, structure, properties.

For citation: Isaev S.L., Baranov D.A., Shchedrin E.Yu., Muratov V.S., Nikitin K.V., Zhatkin S.S. Structure and properties of welds in electron beam welding of iron-chromium-nickel alloy EP718. *Izvestiya. Non-Ferrous Metallurgy.* 2023;29(6):44–53.
https://doi.org/10.17073/0021-3438-2023-6-44-53

Структура и свойства сварных швов при электронно-лучевой сварке железохромоникелевого сплава ЭП718

С.Л. Исаев[1], **Д.А. Баранов**[1], **Е.Ю. Щедрин**[1], **В.С. Муратов**[2], **К.В. Никитин**[2], **С.С. Жаткин**[2]

[1] **ПАО «ОДК-Кузнецов»**
Россия, 443022, г. Самара, Заводское шоссе, 29

[2] **Самарский государственный технический университет**
Россия, 443100, г. Самара, ул. Молодогвардейская, 244

✉ Константин Владимирович Никитин (kvn-6411@mail.ru)

Аннотация: Приведены результаты исследований особенностей формирования структуры и свойств сварных соединений сплава ЭП718 толщиной 13 мм (с учетом технологической подкладки 3 мм) за счет варьирования параметров электронно-лучевой сварки (тока луча и скорости его перемещения по поверхности образца) и определения оптимального режима сварки для данного сплава, используемого при изготовлении статора высокого давления авиационного двигателя. Деталь является ответственным крупногабаритным изделием сложной профильной формы и работает в условиях малоцикличных нагрузок при высоком уровне напряжений. Минимальный предел прочности 1160 МПа имеют образцы, сваренные при скорости перемещения луча по поверхности образца $v = 0{,}0042$ м/с и токе луча 85 мА. Для образцов, сваренных при $v = 0{,}006$ м/с и $i = 65$ мА, характерен максимальный предел прочности, равный 1270 МПа. При определении временного сопротивления у образцов, сваренных при $v = 0{,}006$ м/с, $i = 120$ и 75 мА, разрушение произошло по сварному шву, а у образцов, сваренных при $v = 0{,}006$ м/с, $i = 65$ мА и $v = 0{,}0042$ м/с, $i = 85$ мА, – по зоне термического влияния на расстоянии 0,5–3,0 мм от сварного шва. При микроисследовании структуры образцов, сваренных при $v = 0{,}006$ и 0,0042 м/с и $i = 120$, 75 и 85 мА соответственно, выявлены расширенные границы зерен в зоне термического влияния. Таким образом, оптимальным является режим сварки при скорости перемещения луча по поверхности образца 0,006 м/с и токе луча 65 мА. На данном режиме утолщенных границ зерен не обнаружено и достигается максимальный предел прочности 1270 МПа.

Ключевые слова: электронно-лучевая сварка, жаропрочные никелевые сплава, зона термического влияния, структура, свойства.

Для цитирования: Исаев С.Л., Баранов Д.А., Щедрин Е.Ю., Муратов В.С., Никитин К.В., Жаткин С.С. Структура и свойства сварных швов при электронно-лучевой сварке железохромоникелевого сплава ЭП718. *Известия вузов. Цветная металлургия*. 2023;29(6):44–53. https://doi.org/10.17073/0021-3438-2023-6-44-53

Introduction

In recent years, the use of heat-resistant alloys in heavy-duty, large-scale power units and assemblies within aviation engineering has significantly expanded. These components often operate under low cycle loads at high stress levels. Among the most compelling alloys are those with tensile strengths ranging from 980 to 1200 MPa [1]. One such alloy, KhN45VMTYUBR-ID (EP718), has gained attention due to its application in parts operating in temperature ranges of up to 700—800 °C. Welding plays a pivotal role in the production of these components.

Welded joints possess distinct mechanical and operational characteristics, which can markedly differ from those of the base metal. The reliability and longevity of welded structures are predominantly influenced by the quality and structure of the weld metal, the heat-affected zone, and the joint's design. Welding heat-resistant alloys introduces unique challenges, including the propensity for defect formation, such as cracks [2; 3].

Electron beam welding (EBW) has emerged as a method offering minimal remelted material, minimal product deformation, and strength on par with the base material. However, achieving high-quality welded joints through EBW requires precise control of edge penetration, as well as minimizing chemical and structural inhomogeneities in the weld metal and heat affected zone (HAZ) while reducing residual stresses and eliminating defects like cracks and pores [4; 5].

Analysis of scientific publications from both foreign and domestic scientists reveals that various methods for creating defect-free permanent joints in the heat-resistant alloy EP718 are actively under investigation worldwide. For example, in [6], defect-free joints on 5 mm thick sheet specimens were achieved using CO_2 laser welding. In another study, laser welding (LW) of 1.3 mm thick EP718 alloy revealed defects in the root part of the weld, such as pores [7]. [8] explored welds of 3.4 mm thick specimens made by additive growth through electric arc welding (EAW) using a non-melting tungsten electrode in a shielding gas environment. Although a fine-grained structure was obtained after heat treatment, cracks were found in the HAZ. In [9; 10], the influence of heat input during electron beam welding on the possibility of eliminating microcracks in the weld and the HAZ of 2 mm thick specimens was investigated. Furthermore, [11—13] examined welds of Inconel 718 heat-resistant alloy produced through EBW, EAW, and LW technologies at various welding modes, showcasing the impact of grain size on mechanical properties. The effects of stirring during friction welding on the mechanical properties of EP718 alloy welds were explored in [14], as were the electric arc modes for welding 2 mm thick specimens [15]. Additionally, [16] delved into the intricacies of weld formation on 3 mm thick specimens using EBW, while [17] analyzed the welding of consumable electrodes by a magnetically compressed arc on 2 mm thick sheet material of the EP718 alloy.

Some publications have focused on investigating the unique aspects related to the geometry and microstructure of welds, as well as the formation of defects in both the weld and the heat-affected zone, examining ultra-high frequency and conventional EBW, as well as microwave welding [18—20].

In the studies conducted by Russian researchers [21; 22], the structure and properties of welds created through various welding methods, such as robotic welding with a consumable electrode and LW, were thoroughly examined.

For the fabrication of permanent joints using the heat-resistant alloy KhN45MVTYUBR-ID (EP718), concentrated energy flows, including electron beam welding, show promise due to their ability to produce narrow welds and high-quality joints [23]. Nevertheless, the EBW process comes with its set of challenges and unresolved issues, including the potential for cracks, pores, and other defects within the welded metal, which can compromise the reliability and performance characteristics of the final product [24].

The primary objective of this study was to investigate the specific factors influencing the structure and properties of welded joints crafted from the EP718 alloy, featuring a thickness of 13 mm (accounting for a technological substrate of 3 mm). This was achieved by varying the parameters of electron beam welding, such as beam current and the speed of its movement across the specimen's surface, to identify the optimal welding mode. This alloy is extensively used in the production of high-pressure stators for aircraft engines, where the components are of significant size, possess intricate profiles, and operate under low cycle loads at high stress levels. Remarkably, this study considered these critical operational conditions, which were not always accounted for in previous research [6—22].

Materials and methods

The high-pressure stator is fabricated through the welding of two components: the rear flange, which is constructed from a solid rolled ring following Industry standard OST 1.90396-91, and the middle ring, crafted from EP718 sheet material in accordance with Specifications TU 14-1-5095-92. Following the welding process, the component undergoes heat treatment to relieve stress and attain the necessary mechanical properties.

The investigation of welding parameters and the examination of microstructure and mechanical properties were conducted using simulator specimens measured 200 mm in length, 50 mm in width, and 13 mm in thickness. They are constructed from a solid rolled ring (Fig. 1, loc. *1*) and EP718 heat-resistant alloy sheet material (Fig. 1, loc. *2*).

The local chemical composition of the alloy was assessed through qualitative and quantitative *X*-ray spectral microanalysis using a scanning electron microscope. Spectral analysis was conducted to determine the chemical composition of the specimens, and the results are provided in Table 1. The material grade of the specimens matches the EP718 alloy.

Permanent connections were created using an electron beam welding facility. Various EBW modes were employed, involving adjustments to the specimen's movement speed relative to the beam and the beam current strength.

Following the welding process, the specimens underwent heat treatment. Hardening was conducted in an elevator, and ageing was carried out in a shaft electric furnace. The specific heat treatment modes, including hardening and ageing, are detailed Table 2.

To assess the mechanical properties of welded joints, specimens were prepared based on simulator specimens

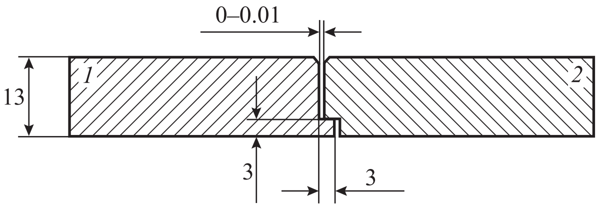

Fig. 1. Sketch of a simulator specimen
1 – solid rolled ring; ***2*** – sheet material
Dimensions are given in mm

Рис. 1. Эскиз образца-имитатора
1 – цельнокатаное кольцо, ***2*** – листовой материал
Размеры указаны в мм

Table 1. **Chemical composition (wt.%) of simulator specimens' material**
Таблица 1. Химический состав (мас.%) материала образцов-имитаторов

Cutting location (Fig. 1)	C	Si	Mn	S	P	Cr	Ni	W	Mo	Ti	Al	Nb
Location 1	0.055	0.007	0.07	0.0016	0.004	15.6	45.24	3.44	4.45	2.08	0.99	1.13
Location 2	0.058	0.08	0.24	0.0016	0.01	15.9	44.73	3.23	4.11	2.17	0.98	1.01
Specifications TU-14-1-5095-92	≤0.1	≤0.3	≤0.6	≤0.01	≤0.015	14–16	43–47	2.5–3.5	4.0–5.2	1.9–2.4	0.9–1.4	0.8–1.5

Table 2. **Heat treatment modes for specimens before and after welding**

Таблица 2. Режимы термической обработки образцов до и после сварки

Heat treatment before welding	Heat treatment after welding		
Quenching	Quenching (stress relieving)	Ageing 1	Ageing 2
t = 1100 °C, τ = 2 h, cooling in air	Heating in air t = 1100 °C, τ = 1 h, cooling to 500–600°C in a container in air with argon supply, further – without argon supply	t = 780 °C, τ = 5 h, cooling in air	t = 650 °C, τ = 16 h, cooling in air

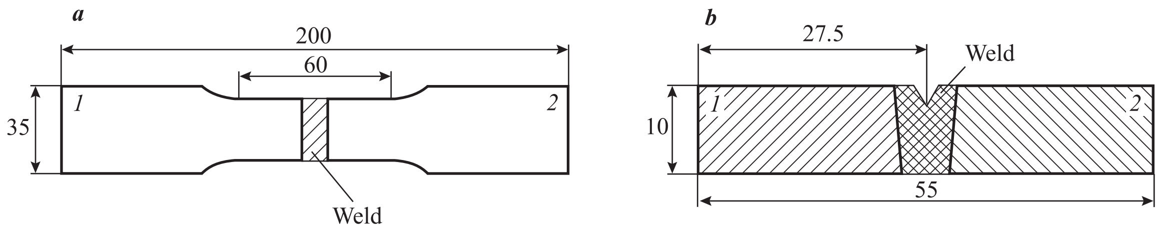

Fig. 2. Sketches of specimens for evaluatng mechanical properties: ultimate tensile strength, yield strength, elongation, and contraction (***a***) and impact strength (***b***)

1 – solid rolled ring, *2* – sheet material. Dimensions are given in mm

Рис. 2. Эскизы образцов для оценки механических свойств: временного сопротивления, предела текучести, относительного удлинения и сужения (***а***) и ударной вязкости (***b***)

1 – цельнокатаное кольцо, *2* – листовой материал. Размеры указаны в мм

to determine the tensile strength (σ_u), yield strength ($\sigma_{0.2}$), relative elongation (δ), and contraction (ψ) as per State Standard GOST 6996-66 (type XIII, Fig. 2, *a*). Impact strength (*KCU*) was also evaluated in accordance with the standard (type IX, Fig. 2, *b*). Notably, the weld was situated at the center of each specimen.

Grain size was determined by measuring chord lengths in accordance with State Standard GOST 5639-82 using specialized software. Microstructure analysis was conducted using an optical microscope equipped with a solid surface microstructure analyzer at various magnifications. Microhardness measurements were performed under a 50 g load.

Results and discussion

Prior to welding, the tensile strength of specimens from a solid rolled ring was determined to be σ_u = = 930 MPa, while the sheet material exhibited a tensile strength of σ_u = 990 MPa. Due to the higher strength of the latter, which exceeded 980 MPa, a quenching process was carried out before welding. Fig. 3 provides insight into the microstructure of a 13 mm thick sheet of the heat-resistant dispersion-hardening nickel alloy EP718 in its as-delivered state and after quenching at 1100 °C, with a 2-hour hold, followed by air cooling. The microstructure of the base material post-heat treatment consists of austenite grains, carbides, and the γ' phase (Fig. 3, *a*). In both scenarios, the average grain size falls within the range of 3—6, in accordance with State Standard GOST 5639-82.

A series of simulator specimens was produced under different welding modes (Table 3). These modes involved variations in the speed of beam movement along the specimen's surface (ν) and the beam current (i). The selection of these parameters was guided by the specifications and aimed to ensure full penetration of specimens with a thickness of 13 mm. The results of the mechanical tests are provided in Table 4.

In modes *1* and *2*, failure during the determination of time resistance occurred along the weld, whereas in other tested specimens, failure took place in the HAZ at a distance of 0.5—3.0 mm from the weld.

Table 3. **Welding modes**

Таблица 3. Режимы сварки образцов

Mode No.	ν, m/s	i, mA
1	0.006	120
2	0.006	75
3	0.006	65
4	0.0042	85

Table 4. **Mechanical properties of welded joints**

Таблица 4. Механические свойства сварных соединений

Mode No.	σ_u, MPa	σ_y, MPa	δ, %	ψ, %	*KCU*, MJ/m^2	Microhardness, kg/mm^2
1	1160	760	17.2	15.5	0.42	308
2	1170	770	17.8	19.0	0.41	329
3	1270	920	21.0	21.7	0.93	348
4	1160	810	15.4	15.5	0.81	335
Specifications TU 14-1-1059-2004	≥1080	≥790	≥13	–	≥0.35	293–363
Specifications TU 14-1-3905-85	≥1080	≥790	≥12	≥14	≥0.35	285–415

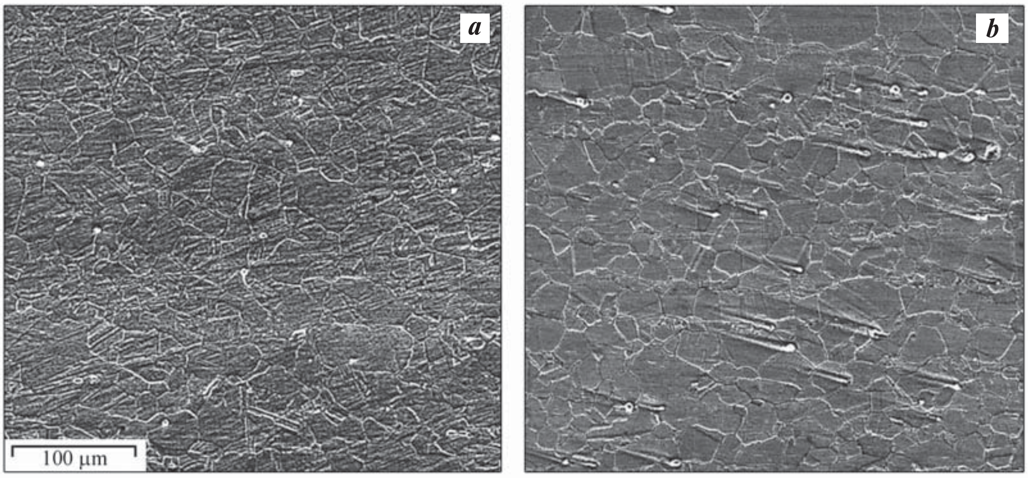

Fig. 3. Microstructure (×400) of EP 718 sheet alloy in as-delivered condition (***a***) and after heat treatment (quenching) (***b***)

Рис. 3. Микроструктура (×400) листового сплава ЭП718 в состоянии поставки (***a***) и после термической обработки (закалки) (***b***)

In the studied welds obtained in modes *1—3*, complete penetration was achieved (Fig. 4, *a—c*). However, in the welded joint of mode 4, a minor lack of penetration of 0.1 mm was observed, with a single pore of 1.0 mm in diameter detected in one section (indicated by arrows in Fig. 4, *d*). According to specifications (RTM 1.4.1703-87), for this material thickness, pores of up to 1.5 mm are permissible. No cracks or other welding defects were identified during the micro-examination of sections of the welded specimens.

The macrostructure of the welds exhibits characteristic zones associated with EBW, including the "mushroom" zone (dimensions *h* and *b*), the knife zone (*e* and *d*), and the weld root in the locking part of the joints (Fig. 4, *c* and *d*) and in the lining area (Fig. 4, *a*). The overall dimensions of the weld for each mode are presented in Table 5.

The highest weld penetration was achieved at a welding current of 120 mA, while specimens in modes *1—3* achieved the required depth. In welding mode *4*, Table 5 shows the widest bath width (*b*) in the 'mushroom' zone and the shallowest depth of penetration. Mode *1* exhibits the highest "mushroom" zone height (*h*), which can lead to additional heating, potential grain boundary thickening, and microcrack formation. Modes *2* and *3* yield the same "mushroom" zone height, but mode *2* has a narrower width. However, mode *3*, with a beam current of 65 mA, provides the shallowest required weld depth, reducing heat input into the metal, minimizing grain boundary thickening in the heat-affected zone, and lowering the risk of crack formation.

In specimens welded in modes *1*, *2*, and *4*, thickened grain boundaries are observed in HAZ before heat treat-

Table 5. **Dimensions of the welds**

Таблица 5. Габаритные размеры сварного шва

Mode No.	*h*, mm	*b*, mm	*e*, mm	*d*, mm	Penetration depth, mm
1	4.0–4.8	8.3–9.0	2.7–3.0	2.1–2.3	13.0
2	3.5–3.7	6.4–7.6	2.6–2.7	2.0–2.3	12.6
3	3.5–3.7	8.0–8.1	2.6–3.0	2.5	11.4
4	4.0–4.6	8.9–9.5	2.7–3.0	0.2–0.8	9.8
Specifications RTM 1.4.1703-87	Optional		1.5–3.5	1.5–2.5	≥10.5

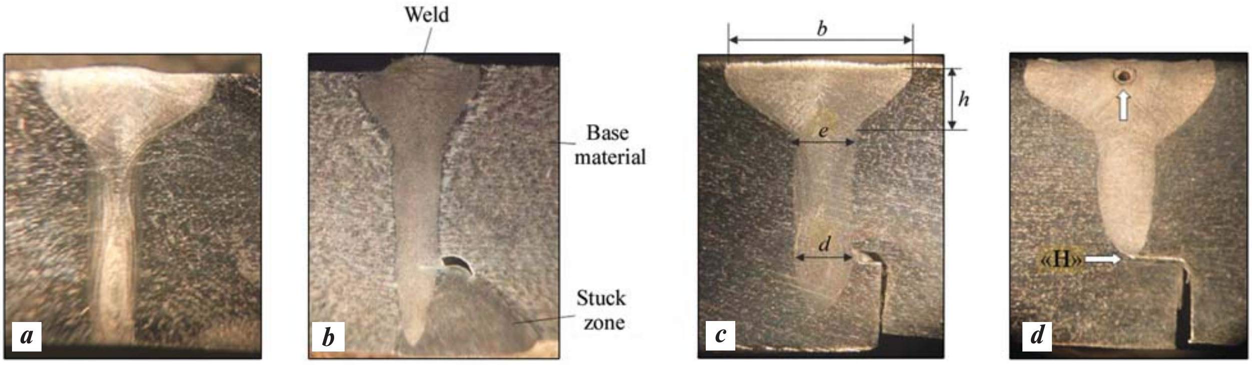

Fig. 4. Macrostructure of welds (×6) obtained in modes ***1*** (***a***), ***2*** (***b***), ***3*** (***c***), and ***4*** (***d***)

Рис. 4. Макроструктура сварных швов (×6), полученных в режимах ***1*** (***a***), ***2*** (***b***), ***3*** (***c***) и ***4*** (***d***)

ment, likely due to carbide phase precipitation during welding and subsequent cooling, accelerating diffusion along grain boundaries, which can lead to crack formation [25]. After heat treatment, the number of thickened grain boundaries increases.

The microstructure of the base material of all specimens is heterogeneous, with varying grain sizes, mainly corresponding to 3—4 points on the GOST 5639-82 scale. In some areas and the heat-affected zone, individual grains with 2—3 points are observed. The microstructure of the specimen from welding mode *3*, shown in Fig. 8, displays no defects in the form of cracks or lack of penetration.

In mode *3*, optimal geometric weld parameters are achieved with no defects. This mode uses the lowest

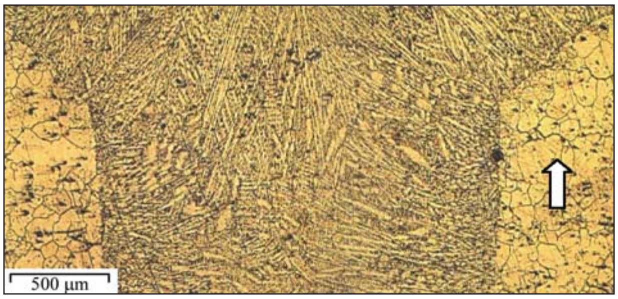

Fig. 5. Microstructure of the weld (×50) obtained in welding mode ***1***

Рис. 5. Микроструктура сварного шва (×50), полученного в режиме сварки ***1***

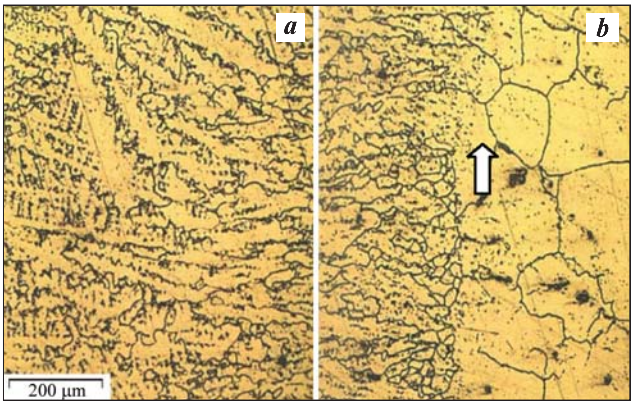

Fig. 6. Microstructure of the specimen (×200) obtained in welding mode ***2***

a – weld, ***б*** – heat-affected zone

Рис. 6. Микроструктура образца (×200), полученного в режиме сварки ***2***

a – сварной шов, ***б*** – околошовная зона

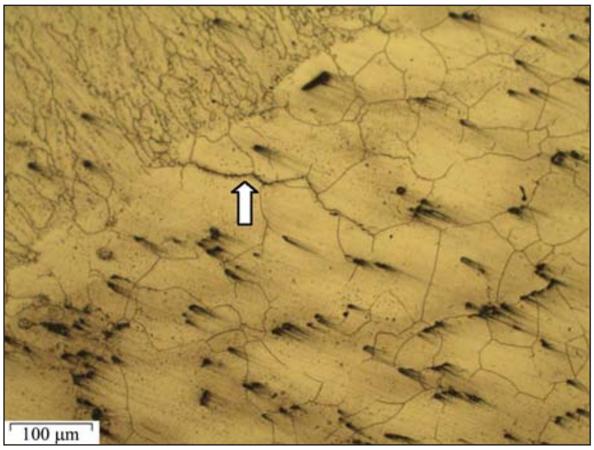

Fig. 7. Microstructure (×100) of the specimen in the heat-affected zone with thickened grain boundaries, obtained in welding mode *4*

Рис. 7. Микроструктура (×100) образца в околошовной зоне с утолщенными границами зерен, полученного в режиме сварки *4*

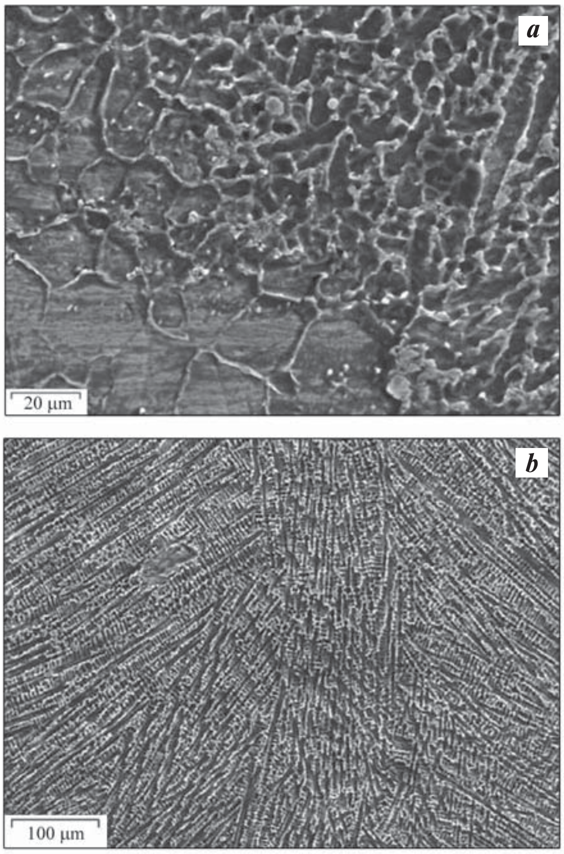

Fig. 8. Microstructure of the base metal sample in the heat-affected zone (***a***) and the weld (***b***) during welding mode *3*

a –600$^\times$ magnification, ***b*** – 250$^\times$ magnification

Рис. 8. Микроструктура образца основного металла в районе околошовной зоны (***a***) и сварного шва (***b***) при сварке в режиме *3*

a – увеличение 600$^\times$, ***b*** – 250$^\times$

beam current, which minimizes base material heating while ensuring complete penetration of the edges. The resulting weld exhibits a columnar structure of a cast alloy, with thread-like crystals closer to the center, enhancing the material's heat resistance in the permanent joint.

The intense heat transfer during EBW conditions results in a reduction of the HAZ size and the formation of a fine dendritic structure along the weld's edge (refer to Fig. 8). The base metal in the HAZ maintains a uniform coarse-grained structure, incorporating carbonitrides, carbides, and a finely dispersed intermetallic γ′ phase. In the microstructure of the HAZ, larger grains are observed compared to the base material.

Conclusions

When studying welds in simulator specimens made of the alloy KhN45MVTYUBR-ID (EP718) with a thickness of 13 mm, the following observations were made:

1. The minimum tensile strength of 1160 MPa is recorded in specimens welded at $\nu = 0.0042$ m/s and a beam current (i) of 85 mA (mode *4*). Conversely, specimens welded at $\nu = 0.006$ m/s and $i = 65$ mA (mode *3*) demonstrated a maximum tensile strength of 1270 MPa.

2. Specimens welded at $\nu = 0.006$ m/s, with $i = 120$ and 75 mA (modes *1* and *2*), exhibited fractures along the weld during tensile testing. In contrast, when using welding modes *3* and *4*, destruction was observed along the HAZ at a distance of 0.5—3.0 mm from the weld.

3. Micro-examination of sections from specimens welded in modes *1*, *2*, and *4* revealed expanded grain boundaries in the HAZ.

4. Based on the obtained data, it was determined that welding mode *3*, with parameters $\nu = 0.006$ m/s and $i = 65$ mA, is optimal. This mode exhibited no thickened grain boundaries and achieved an ultimate tensile strength of 1270 MPa.

References

1. Lomberg B.S., Ovsepyan S.V., Bakradze M.M., Mazalov I.S. High-temperature-resistant wrought nickel alloys for advanced gas turbine engines and gas turbine plants. *Vestnik MGTU im. N.E. Baumana. Ser. Mashinostroenie*. 2011;1—10. (In Russ.).
Ломберг Б.С., Овсепян С.В., Бакрадзе М.М., Мазалов И.С. Высокожаропрочные деформируемые никелевые сплавы для перспективных газотурбинных двигателей и газотурбинных установок. *Вестник МГТУ им. Н.Э. Баумана. Сер. Машиностроение*. 2011;1—10.

2. Kablov E.N. Innovative developments of FSUE “VIAM” of the State Scientific Center of the Russian Federation for the implementation of the “Strategic Directions for the Development of Materials and Technologies for Their Processing for the Period up to 2030”. *Aviacionnye materialy i tekhnologii*. 2015;1(34):3—33. (In Russ.).
Каблов Е.Н. Инновационные разработки ФГУП «ВИАМ» ГНЦ РФ по реализации «Стратегических направлений развития материалов и технологий их переработки на период до 2030 года». *Авиационные материалы и технологии*. 2015;1(34):3—33.
3. Kablov E.N., Antipov V.V., Sviridov A.V., Gribkov M.S. Features of electron-beam welding of heat-resistant alloys EI698-VD and EP718-ID with steel 45. *Trudy VIAM*. 2020;9(91):3—14. (In Russ.).
https://dx.doi.org/ 10.18577/2307-6046-2020-0-9-3-14
Каблов Е.Н., Антипов В.В., Свиридов А.В., Грибков М.С. Особенности электронно-лучевой сварки жаропрочных сплавов ЭИ698-ВД и ЭП718-ИД со сталью 45. *Труды ВИАМ*. 2020;9(91):3—14.
4. Nazarenko O.K., Kajdalov A.A., Kovbasenko S.N. Electron beam welding red. (Ed. B.E. Paton). Kiev: Naukova dumka, 1987. 256 p. (In Russ.).
Назаренко О.К., Кайдалов А.А., Ковбасенко С.Н. Электронно-лучевая сварка (Под ред. Б.Е. Патона). Киев: Наукова думка, 1987. 256 с.
5. Makarov E.L., Yakushin B.F. Theory of weldability of steels and alloys. Moscow: MGTU im. N.E. Baumana, 2014. 487 p. (In Russ.).
Макаров Э.Л., Якушин Б.Ф. Теория свариваемости сталей и сплавов. М.: МГТУ им. Н.Э. Баумана, 2014. 487 с.
6. Hong J.K., Park J.H., Park N.K., Eom I.S., Kim M.B., Kang C.Y. Microstructures and mechanical properties of Inconel 718 welds by CO_2 laser welding. *Journal of Materials Processing Technology*. 2008;1:515—520.
https://doi.org/10.1016/j.jmatprotec.2007.11.224
7. Patela V., Salia A., Hyderb J., Corlissb M., Hyderb D., Hunga W. Electron beam welding of inconel 718 procedia manufacturing. In: *Proc. 48th SME North American Manufacturing Research Conference* (Ohio, USA). 2020. Vol. 1. P. 428—435.
https://doi.org/10.1016/j.promfg.2020.05.065
8. Raza T., Andersson J., Svensson L.E. Varestraint weldability testing of additive manufactured alloy 718. *Science and Technology of Welding and Joining*. 2018;23(7): 606—611. https://doi.org/10.1080/13621718.2018.1437338
9. Agilan M., Venkateswaran T., Sivakumar D., Pant B. Effect of heat input on microstructure and mechanical properties of Inconel-718 EB welds. *Procedia Materials Science*. 2014;5:656—662.
https://doi.org/ 10.1016/j.mspro.2014.07.312
10. Mei Y., Liu Y., Liu C., Li C., Yu L., Guo Q., Li H. Effect of base metal and welding speed on fusion zone microstructure and HAZ hot-cracking of electron-beam welded Inconel 718. *Materials and Design*. 2016;89:964—977.
https://doi.org/ 10.1016/j.matdes.2015.10.082
11. Peng G., Zhang K.F., Zhang B.G., Jiang S.S., Zhang B.W. Microstructures and high temperature mechanical properties of electron beam welded Inconel 718 superalloy thick plate. *Transactions of Nonferrous Metals Society of China*. 2011;21:315—322.
https://doi.org/ 10.1016/S1003-6326(11)61598-7
12. Manikandan S., Sivakumar D., Rao K.P., Kamaraj M. Effect of enhanced cooling on microstructure evolution of alloy 718 using the gas tungsten arc welding process. Weld World. 2016. 18 p.
https://doi.org/10.1007/s40194-016-0349-1
13. Zhang Y.N., Cao X., Wanjara P. Microstructure and hardness of fiber laser deposited Inconel 718 using filler wire. *The International Journal of Advanced Manufacturing Technology*. 2013;69:9—12.
https://doi.org/10.1007/s00170-013-5171-y
14. Song K.H., Kim W.Y., Nakata K. Investigation of microstructure and mechanical properties on surface-modified Inconel 718 alloy. *Materials Transactions*. 2013;(54)10:2032—2036.
https://doi.org/10.2320/matertrans.M2013096
15. Sonar T., Balasubramanian V., Malarvizhi S., Venkateswaran T., Sivakumar D. Effect of Delta current and Delta current frequency on microstructure and tensile properties of gas tungsten constricted arc (GTCA) welded Inconel 718 alloy joints. *Journal of the Mechanical Behavior of Materials*. 2019;28(1):186—200.
https://doi.org/10.1515/jmbm-2019-0020
16. Sumit K. Sharma, Prashant Agarwal, J. Dutta Majumdar. Studies on electron beam welded Inconel 718 similar joints: Proceedings of the International Conference on Sustainable Materials Processing and Manufacturing (23—25 January 2017, Kruger National Park). *Procedia Manufacturing*. 2017;7:654—659. https://doi.org/10.1016/j.promfg.2016.12.097
17. Tushar S., Visvalingam B., Sudersanan M., Thiruvenkatam V., Dhenuvakonda S. Influence of magnetically constricted arc traverse speed (MCATS) on tensile properties and microstructural characteristics of welded Inconel 718 alloy sheets. *Defence Technology*. 2020. P. 40.
https://doi.org/10.1016/j.dt.2020.07.009
18. Kwon S.I., Bae S.H., Do J.H., Jo C.Y., Hong H.U. Characterization of the microstructures and the cryogenic mechanical properties of electron beam welded Inconel 718. *Metallurgical and Materials Transactions*. 2015;47(2):77—87.
https://doi.org/10.1007/s11661-015-3269-6
19. Jia Z., Wan X., Guo D. Study on microstructure and me-

chanical properties of Inconel718 components fabricated by UHFP-GTAW technology. *Materials Letters.* 2019;261: 1—9. https://doi.org/10.1016/j.matlet.2019.127006

20. Bansal A., Sharma A.K., Das S., Kumar P. Characterization of microstructure and strength of microwave welded Inconel 718 joints at 2.45 GHz frequency. *Kovove materialy.* 2016;54:27—35.
https://doi.org/10.4149/km_2016_1_27

21. Nikiforov R.V., Galimov V.R., Hisamutdinov E.R., Kamaletdinova R.R., Basharov R.R. Structure and properties of welded joints of EP718 alloy produced by robotic consumable electrode welding. *Vestnik UGATU.* 2021;4(94):10—18. (In Russ.).
Никифоров Р.В., Галимов В.Р., Хисамутдинов Э.Р., Камалетдинова Р.Р., Башаров Р.Р. Структура и свойства сварных соединений сплава ЭП718, полученных роботизированной сваркой плавящимся электродом. *Вестник УГАТУ.* 2021;4(94):10—18.

22. Baranov D.A., Parkin A.A., Zhatkin S.S. Peculiarities of weld seam formation in KhN45VMTYuBR heat-resistant alloy depending on laser welding modes. *Izvestiya Samarskogo nauchnogo centra Rossiyskoy akademii nauk.* 2018;4(2):170—176. (In Russ.).
Баранов Д.А., Паркин А.А., Жаткин С.С. Особенности формирования сварного шва жаропрочного сплава ХН45ВМТЮБР в зависимости от режимов лазерной сварки. *Известия Самарского научного центра Российской академии наук.* 2018;4(2):170—176.

23. Kaydalov A.A. Electron beam welding and related technologies. Kiev: Ekotekhnologiya, 2004. 260 p. (In Russ.).
Кайдалов А.А. Электронно-лучевая сварка и смежные технологии. Киев: Экотехнология, 2004. 260 с.

24. Sorokin L.I. Formation of hot cracks in the near-weld zone during welding of heat-resistant nickel alloys. *Svarochnoe proizvodstvo.* 2005;8:4—18. (In Russ.).
Сорокин Л.И. Образование горячих трещин в околошовной зоне при сварке жаропрочных никелевых сплавов. *Сварочное производство.* 2005;8:4—18.

25. Parshukov L.I., Gilmutdinov F.Z. Electron-beam welding and local heat treatment of welds from heat-resistant alloys. *Trudy VIAM.* 2017;5(53):23—31. (In Russ.).
http://dx.doi.org/10.18577/2307-6046-2017-0-5-3-3
Паршуков Л.И., Гильмутдинов Ф.З. Электронно-лучевая сварка и локальная термообработка сварных швов из жаропрочных сплавов. *Труды ВИАМ.* 2017;5(53):23—31.

Information about the authors

Sergey L. Isaev – Deputy Chief Welder for Production, PJSC "ODK-Kuznetsov".
https://orcid.org/0009-0006-6329-4685
E-mail: isl231083@yandex.ru

Dmitry A. Baranov – Cand. Sci.(Eng.), Deputy Chief Welder for New and Repair Technologies, PJSC "ODK-Kuznetsov".
https://orcid.org/0009-0009-8955-8556
E-mail: D.Baranov91@mail.ru

Evgeny Yu. Shchedrin – Chief Welder, PJSC "ODK-Kuznetsov".
https://orcid.org/0009-0004-0406-915X
E-mail: Chiefwelder24@yandex.ru

Vladimir S. Muratov – Dr. Sci. (Eng.), Professor of the Department of Metallurgy, Powder Metallurgy, Nanomaterials, Samara State Technical University (SamSTU).
https://orcid.org/0000-0001-8637-1096
E-mail: muratov1956@mail.ru

Konstantin V. Nikitin – Dr. Sci. (Eng.), Dean of the Faculty of Metallurgy, Mechanical Engineering and Transport, SamSTU.
https://orcid.org/0000-0001-7061-0144
E-mail: kvn-6411@mail.ru

Sergey S. Zhatkin – Cand. Sci.(Eng.), Professor of the Department of Foundry and High-Efficiency Technologies, SamSTU.
https://orcid.org/0000-0001-5625-848X
E-mail: Sergejat@mail.ru

Информация об авторах

Сергей Леонидович Исаев – зам. гл. сварщика по производству, ПАО «ОДК-Кузнецов».
https://orcid.org/0009-0006-6329-4685
E-mail: isl231083@yandex.ru

Дмитрий Александрович Баранов – к.т.н., зам. гл. сварщика по новым и ремонтным технологиям,
ПАО «ОДК-Кузнецов».
https://orcid.org/0009-0009-8955-8556
E-mail: D.Baranov91@mail.ru

Евгений Юрьевич Щедрин – гл. сварщик,
ПАО «ОДК-Кузнецов».
https://orcid.org/0009-0004-0406-915X
E-mail: Chiefwelder24@yandex.ru

Владимир Сергеевич Муратов – д.т.н., профессор кафедры «Металловедение, порошковая металлургия, наноматериалы», Самарский государственный технический университет (СамГТУ).
https://orcid.org/0000-0001-8637-1096
E-mail: muratov1956@mail.ru

Константин Владимирович Никитин – д.т.н., декан факультета металлургии, машиностроения и транспорта, СамГТУ.
https://orcid.org/0000-0001-7061-0144
E-mail: kvn-6411@mail.ru

Сергей Сергеевич Жаткин – к.т.н., профессор кафедры «Литейные и высокоэффективные технологии», СамГТУ.
https://orcid.org/0000-0001-5625-848X
E-mail: Sergejat@mail.ru

Contribution of the authors

S.L. Isaev – determined the purpose of the work, conducted experiments, wrote an article.

D.A. Baranov – prepared the initial samples, participated in the discussion of the results.

E.Yu. Shchedrin – participated in the metallographic study of the structure of welds, participated in the discussion of the results.

V.S. Muratov – determined the methodology of experiments, participated in the discussion of the results, wrote the article.

K.V. Nikitin – participated in writing the article and discussing the results

S.S. Zhatkin – carried out a literature review, participated in the discussion of the results.

Вклад авторов

С.Л. Исаев – определение цель работы, проведение экспериментов, написание текста статьи.

Д.А. Баранов – подготовка исходных образцов, участие в обсуждении результатов.

Е.Ю. Щедрин – участие в проведении металлографического исследования структуры сварных швов и в обсуждении результатов.

В.С. Муратов – определение методики экспериментов, участие в обсуждении результатов, написание текста статьи.

К.В. Никитин – участие в написании статьи и обсуждении результатов

С.С. Жаткин – литературный обзор, участие в обсуждении результатов.

The article was submitted 11.07.2023, revised 02.10.2023, accepted for publication 04.10.2023

Статья поступила в редакцию 11.07.2023, доработана 02.10.2023, подписана в печать 04.10.2023

PHYSICAL METALLURGY AND HEAT TREATMENT / МЕТАЛЛОВЕДЕНИЕ И ТЕРМИЧЕСКАЯ ОБРАБОТКА

UDC 669.295:669.018.9
https://doi.org/10.17073/0021-3438-2023-6-54-65

Research article
Научная статья

Influence of partial titanium substitution by its hydride on structure and mechanical properties of TNM-B1 heat-resistant alloy, obtained by SHS powder hot isostatic pressing

G.M. Markov[1], **P.A. Loginov**[1], **N.V. Shvyndina**[1],
F.A. Baskov[1,2], **E.A. Levashov**[1]

[1] **National University of Science and Technology "MISIS"**
4 build. 1 Leninskiy Prosp., Moscow 119049, Russia

[2] **JSC "Composite"**
4 Pionerskaya Str., Moscow region, Korolev 141074, Russia

✉ Georgy M. Markov (markov.sci@gmail.com)

Abstract: This paper investigates the influence of partial substitution of titanium by its hydride on the microstructure and mechanical properties of TNM-B1 alloy obtained by powder metallurgy technology. The impact of the Ti:TiH_2 ratio in the reaction mixture and heat treatment modes on the microstructure and mechanical properties of TNM-B1+1%Y_2O_3 alloy, obtained using high-energy ball milling (HEBM), self-propagating high-temperature synthesis (SHS), and hot isostatic pressing (HIP) methods, has been examined. It was observed that a 10 % substitution of titanium with its hydride in the reaction mixtures reduces the oxygen content in SHS products from 1 % to 0.8 % due to the generation of a reducing atmosphere during the decomposition of TiH_2 in the combustion wave. When the Ti : TiH_2 ratio is 90 : 10, highest mechanical properties of TNM-B1+1%Y_2O_3 alloy were achieved: a compressive strength (σ_u) of 1200±15 MPa and a yield strength (YS) of 1030±25 MPa. An increase in the proportion of TiH_2 results in a higher content of oxygen impurity, leading to the formation of Al_2O_3, which reduces the strength and ductility of the material. With additional heat treatment of TNM-B1+1%Y_2O_3 alloy, the globular structure transforms into a partially lamellar one, leading to an increase in σ_u by 50–300 MPa, depending on the TiH_2 content. This attributed to a decrease in the average grain size and a reduction in dislocation mobility during deformation.

Keywords: titanium alloys, titanium hydride, powder metallurgy, high energy machining (HEBM), self-propagating high temperature synthesis (SHS), hot isostatic pressing (HIP), mechanical properties.

Acknowledgments: This work received support from the Ministry of Science and Higher Education of the Russian Federation (Project No. 0718-2020-0034).

For citation: Markov G.M., Loginov P.A., Shvyndina N.V., Baskov F.A., Levashov E.A. Influence of partial titanium substitution by its hydride on structure and mechanical properties of TNM-B1 heat-resistant alloy, obtained by SHS powder hot isostatic pressing. *Izvestiya. Non-Ferrous Metallurgy*. 2023;29(6):54–65.
https://doi.org/10.17073/0021-3438-2023-6-54-65

Влияние частичного замещения титана его гидридом на структуру и свойства жаропрочного сплава TNM-B1, полученного методом горячего изостатического прессования СВС-порошка

Г.М. Марков[1], **П.А. Логинов**[1], **Н.В. Швындина**[1], **Ф.А. Басков**[1,2], **Е.А. Левашов**[1]

[1] **Национальный исследовательский технологический университет «МИСИС»**
Россия, 119049, г. Москва, Ленинский пр-т, 4, стр. 1

[2] **АО «Композит»**
Россия, 141074, Московская обл., г. Королев, ул. Пионерская, 4

✉ Георгий Михайлович Марков (markov.sci@gmail.com)

Аннотация: В работе исследовано влияние частичного замещения титана его гидридом на микроструктуру и механические свойства сплава TNM-B1, полученного по технологии порошковой металлургии. Рассмотрено влияние соотношения Ti:TiH$_2$ в реакционной смеси и режимов термообработки на микроструктуру и механические свойства сплава TNM-B1+1%Y$_2$O$_3$, полученного с использованием методов высокоэнергетической механической обработки (ВЭМО), самораспространяющегося высокотемпературного синтеза (СВС) и горячего изостатического прессования (ГИП). Установлено, что 10 %-ное замещение титана его гидридом в реакционных смесях позволяет уменьшить содержание кислорода в СВС-продуктах с 1 до 0,8 % благодаря созданию восстановительной атмосферы при разложении TiH$_2$ в волне горения. При соотношении Ti : TiH$_2$ = = 90 : 10 достигнуты максимальные механические свойства сплава TNM-B1+1%Y$_2$O$_3$: прочность при сжатии $\sigma_в$ = 1200±15 МПа и предел текучести $\sigma_{0,2}$ = 1030±25 МПа. Рост доли TiH$_2$ увеличивает содержание примесного кислорода, приводящего к образованию Al$_2$O$_3$, который снижает прочность и пластичность материала. За счет дополнительной термообработки сплава TNM-B1+1%Y$_2$O$_3$ глобулярная структура преобразуется в частично ламеллярную, что приводит к увеличению $\sigma_в$ на 50–300 МПа в зависимости от содержания TiH$_2$. Получаемый эффект обусловлен уменьшением среднего размера зерен и снижением подвижности дислокаций при деформации.

Ключевые слова: титановые сплавы, гидрид титана, порошковая металлургия, высокоэнергетическая механическая обработка (ВЭМО), самораспространяющийся высокотемпературный синтез (СВС), горячее изостатическое прессование (ГИП), механические свойства.

Благодарности: Работа выполнена при финансовой поддержке Министерства науки и высшего образования РФ в рамках государственного задания (проект 0718-2020-0034).

Для цитирования: Марков Г.М., Логинов П.А., Швындина Н.В., Басков Ф.А., Левашов Е.А. Влияние частичного замещения титана его гидридом на структуру и свойства жаропрочного сплава TNM-B1, полученного методом горячего изостатического прессования СВС-порошка. *Известия вузов. Цветная металлургия.* 2023;29(6):54–65.
https://doi.org/10.17073/0021-3438-2023-6-54-65

Introduction

Heat-resistant alloys based on TiAl/Ti3Al intermetallic compounds represent an independent class of materials, the main feature of which is high strength at elevated temperatures and heat resistance. These alloys find applications in the field of engine construction, where materials capable of enduring high-temperature loads for extended periods are essential [1]. Their relatively low density (3.9—4.2 g/cm^3) results in higher specific strength when compared to nickel superalloys. Combined with exceptional creep resistance, this makes them promising candidates for use as materials in low-pressure turbine blades [2; 3].

Most industrial alloys based on TiAl/Ti$_3$Al contain between 43 to 48 atomic percent aluminum. The optimal aluminum concentration depends on the presence of dopants that influence the position of the γ and $\alpha + \gamma$ phase regions on the Ti—Al phase diagram. Several generations of alloys based on titanium aluminides have been developed [4]. The 1st generation includes the Ti—48Al—2Cr—2Nb alloy, known as GE4822, as well as low-alloy analogues like Ti—47Al—2Cr—2Nb and Ti—48Al—2Cr—2Mn [4; 5]. The complexity of the alloying system using V, Zr, W, Ta, Mn, and other elements has led to the creation of 2nd generation alloys [6]. The 3rd generation alloys represent the most advanced materials within the TiAl-based family. They are characterized by a high content of niobium, molybdenum, and the presence of boron, with the primary structural component consisting of $\alpha_2 + \gamma$ eutectoid colonies [7; 8].

Conventional methods for producing intermetallic alloys based on TiAl include casting technologies, such as vacuum induction melting [9]. These methods compete with powder metallurgy techniques [10], which encompass additive manufacturing allowing the production of items with complex geometries from powder [11]. Additionally, a combination of methods involving high-energy ball milling (HEBM) of elemental powder mixtures, self-propagating high-temperature synthesis (SHS), and hot isostatic pressing (HIP) [12—14] are utilized [12—14]. The key advantages of the latter approach are the ability to produce materials with a homogeneous, fine-grained structure and the suppression of the β phase formation, which is characteristic of high-niobium alloys. A non-uniform distribution of the β phase reduces creep resistance and high-temperature strength [15].

In multicomponent alloys, the distribution of elements can be uneven due to their low solubility. The use of HEBM can address this issue by enhancing the uniformity of the element distribution in the reaction mixture, as well as increasing the reactivity of the charge, which positively impacts the degree of conversion during SHS [14].

The SHS process can be implemented in the layer-by-layer combustion mode, resulting from local thermal initiation [16; 17], or in the mode of volumetric combustion (thermal explosion) [6]. This method is widely employed for obtaining intermetallic materials, including titanium aluminides [13; 18].

Challenges in the production of intermetallic alloys through powder metallurgy methods include an increased content of impurity oxygen and microstructural heterogeneity, leading to a decrease in high-temperature strength characteristics [19; 20]. One solution to this issue could be the partial substitution of metallic titanium in the powder reaction mixture with its hydride (TiH_2). TiH_2 is easily ground in a planetary centrifugal mill due to its high brittleness [19], uniformly distributed as individual particles that are insoluble in the matrix [20], and decomposes to metallic titanium at relatively low temperatures (400—750 °C) [21]. TiAl-based alloys with TiH_2 are not produced using conventional casting technology because titanium hydride promotes active pore formation during decomposition and the release of accompanying gases. However, in powder technology, due to the staged nature and flexibility of consolidation modes, the use of TiH_2 is of interest. In this case, it is important to determine the optimal Ti : TiH_2 ratio in the reaction mixture, considering the composition of oxygen impurities, microstructure, and mechanical properties of consolidated and heat-treated samples.

The objective of this research was to study the effect of partial substitution of titanium with its hydride on the microstructure and mechanical properties of the TNM-B1 powder alloy.

Materials and methods

Initial materials

The following powder materials, produced in Russia, were used in this study:

- titanium grade PTOM-1 (AO Polema, particle size $d = 40$ μm);
- TiH_2 powder obtained through the hydrogenation of titanium sponge (ZAO "Plasmoterm", $d \sim 12$ μm);
- aluminum PA-4 (AO "Polema", $d \sim 10$ μm);
- niobium NbP-3a (OOO "GK SMM", $d < 40$ μm);
- molybdenum PM-99.95 (AO "Polema", $d = 5$ μm);
- boron grade V-99A (OOO "NPK Ermakhim", $d \sim 0.2$ μm);
- yttrium oxide nanopowder (ZAO "Plazmoterm", $d \sim 20 \div 100$ nm).

These components were combined in the necessary ratios to produce the well-known 3rd generation TNM-B1 alloy based on TiAl [13, 14], hereafter referred to as TNM-B1+1%Y_2O_3 in the text. The Ti : TiH_2 ratio in the mixture was varied as follows (wt.%): 90 : 10, 80 : 20, 70 : 30, and 60 : 40.

High-energy ball milling

Powder mixtures were prepared in two stages. In the first stage, Ti, TiH_2, Nb, Mo, B, and Y_2O_3 powders were mixed in an Activator-4M planetary centrifugal mill (PCM) (OOO "Machine Building Plant Activator", Russia). The grinding jars were rolled at a speed of 694 rpm for a duration of 10 min. The weight ratio of materials to grinding media was 1 : 15, and the jars were filled with argon to protect the mixture against oxidation. Subsequently, aluminum was added to the Ti/TiH_2—Nb—Mo—B—Y_2O_3 alloy obtained after HEBM, and it was mixed using a rotating ball mill for 2 h. The weight ratio of the mixture components to grinding media was 1 : 10. The use of this mixer in the second stage was necessary to prevent oxidation and the adhesion of plastic aluminum to the jar walls and grinding media.

Self-propagating high-temperature synthesis

Briquetted powder mixtures, following HEBM, were inserted into a tube furnace by advancing crucible with briquettes into a hot zone heated to 900 °C to initiate the SHS process in thermal explosion mode within an argon atmosphere. Following SHS, annealing was conducted in a furnace for 30 min at the same temperature to homogenize the chemical composition of the synthesis products. Subsequent to sintering, the SHS workpieces were crushed using a jaw crusher and a PCM to achieve a powder with a particle size of less than 100 μm. The desired fraction was then separated using sieve classification.

Hot isostatic pressing

The resulting powder was consolidated by the HIP method using an HIRP10/26—200 gas static extruder (ABRA AG, Switzerland). Pre-forming workpieces, which were cylindrical titanium capsules, were annealed in a vacuum at a temperature of 1030 °C for 1 hour to eliminate gas impurities. The HIP process was conducted at 1250 °C and a pressure of 160 MPa, with argon serving as the pressure transfer medium. For the samples consolidated via the HIP method, a heat treatment (HT) was carried out for 2 h at a temperature of 1380 °C in a Termionik T1 vacuum furnace (OOO “Termionika”, Russia).

Research procedures for structure and mechanical properties

Powder materials and compact samples were subjected to *X*-ray diffraction analysis (XRD) using a D2 PHASER diffractometer (Bruker AXS GmbH, Germany). CuK_α radiation was employed in the diffraction angle range of $2\theta = 20°\div100°$, with an exposure time of 0.6 s.

The microstructure of both powder and consolidated samples was examined using an S-3400 N scanning electron microscope (Hitachi, Japan), equipped with a NORAN attachment for energy dispersive *X*-ray spectroscopy (EDX). The oxygen content in the mixtures following each technological operation was determined by incinerating the material in an inert atmosphere using a TC-600 device (Leco, USA), in accordance with ASTM E1019-18. Mechanical tests were conducted using uniaxial compression on cylindrical samples (∅6 × 9.0 mm) with a strain rate of ~0.001 s^{-1}. These tests were performed on an LF-100 kN universal testing machine (Walter + Bai AG, Switzerland).

Results and discussion

High-energy ball milling

Figure 1 illustrates the microstructures of powders with different Ti : TiH_2 ratios obtained using the HEBM method. The base of powder agglomerates, formed during processing due to intense plastic deformation, consists of titanium and its hydride. The primary components are arranged in the form of alternating layers, up to 3 μm thick (Fig. 1, *e*). As the TiH_2 content increases, the degree of their agglomeration into larger particles also increases. The dopants, Nb, and Mo, are uniformly distributed inside the particles in the form of thin layers. This distribution enhances their dissolution rate within the γ-TiAl/α_2-Ti_3Al-based matrix during the SHS process [13].

In the *X*-ray diffraction patterns obtained from the ligature immediately after HEBM, only peaks corresponding to the initial powder materials, including α-Ti, TiH_2, Nb, and Mo, are evident (Fig. 2). The intensity of the TiH_2 peaks increases in proportion to the fraction of hydride in the master alloy, indicating that it remains intact during the HEBM process and does not decompose into metallic titanium and hydrogen. Niobium and molybdenum, characterized by a BCC lattice with an $Im3m$ space group, are observed in granular form as independent phases. This can be attributed to the low solubility of these components in titanium, which has an HCP lattice, owing to differences in crystal structure as well as their high hardness and low plasticity.

Study of synthesis products and their consolidation via hot isostatic pressing

After further mixing of Ti/TiH2—Nb—Mo—B—Y_2O_3 master alloys with aluminum and conducting syntheses in thermal explosion mode, SHS-sintered samples were obtained, and their microstructure and phase composition were examined. It was observed that the samples following SHS possess a uniform microstructure with localized regions enriched in the alloying components Nb and Mo, as depicted in Fig. 3. No unreacted Ti and Al particles were detected. An increase in the TiH_2 concentration in the initial mixture resulted in a reduction in the grain size of the synthesis products. This effect is attributed to the intense hydrogen evolution and, consequently, the disruption of the briquettes’ integrity, leading to increased porosity in the SHS-sintered samples.

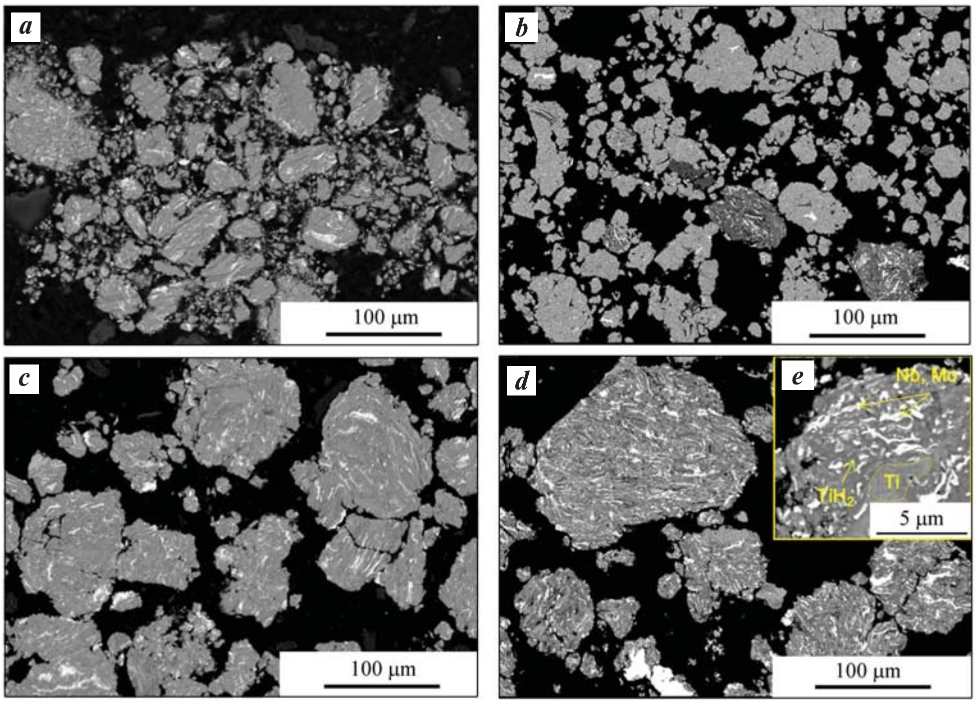

Fig. 1. Structure of Ti/TiH_2–Nb–Mo–B–Y_2O_3 powder particles after HEBM
TiH_2, wt.%: 10 (***a***), 20 (***b***), 30 (***c***), 40 (***d***, ***e***)

Рис. 1. Структура порошковых частиц Ti/TiH_2–Nb–Mo–B–Y_2O_3 после ВЭМО
TiH_2, мас.%: 10 (***a***), 20 (***b***), 30 (***c***), 40 (***d***, ***e***)

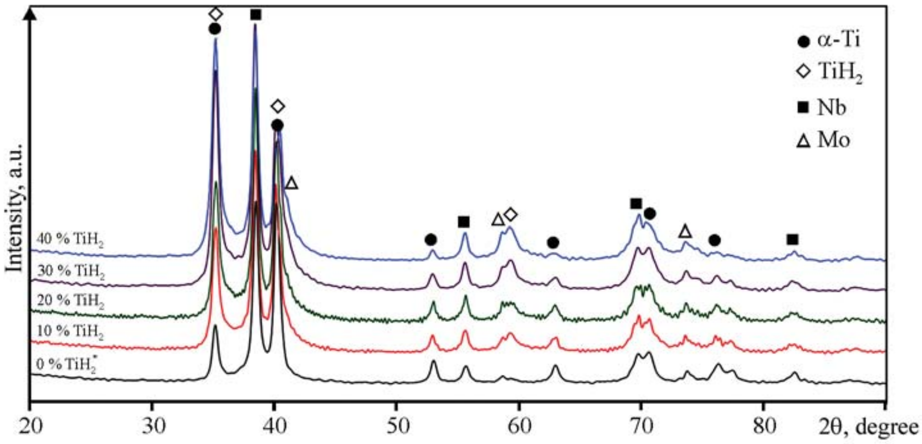

Fig. 2. *X*-ray diffraction patterns of Ti/TiH_2–Nb–Mo–B–Y_2O_3 powders after HEBM
(0%TiH_2 XRD pattern based on the data published in [13])

Рис. 2. Рентгенограммы лигатур Ti/TiH_2–Nb–Mo–B–Y_2O_3 после ВЭМО
(на основе материалов, опубликованных в работе [13])

According to the XRD data (Fig. 4), the resulting SHS powder consists of 78 % γ-TiAl (*P*4/*mmm*), 19 % α_2-Ti_3Al (*P*63/*mmc*), and 3 % solid solution (Nb) (*Im*-3*m*). The absence of TiH_2 peaks suggests that during the SHS process, this phase underwent complete decomposition, and the resulting metallic titanium reacted with aluminum. The formation of γ-TiAl and α_2-Ti_3Al follows a reaction diffusion mechanism. Initially, aluminum melts and spreads over the titanium surface, accompanied by the creation of the $TiAl_3$ phase. As the liquid phase diminishes and diffusion interaction between Ti and $TiAl_3$ becomes active, intermetallic compounds form in the following sequence: $TiAl_2 \rightarrow \rightarrow TiAl \rightarrow Ti_3Al$ [24—26]. The powder particles obtained via the SHS method exhibit a microgradient structure based on the α_2-Ti_3Al and γ-TiAl phases (Fig. 3).

Compact samples of the TNM-B1+1%Y_2O_3 alloy were produced using the HIP method. To achieve a lamellar microstructure, the alloys were further subjected to HT. The resulting microstructures of the alloy are depicted in Fig. 5. The sample after HIP exhibits a fine-grained globular structure inherited from SHS powders, with the primary structural components taking the form of γ-TiAl and α_2-Ti_3Al phases. Fine aluminum oxide particles are also observable in SEM images, but their concentration in the alloy with 10 % TiH_2 is minimal. *X*-ray diffraction patterns indicate that the intensity of the peaks corresponding to the Al_2O_3 phase

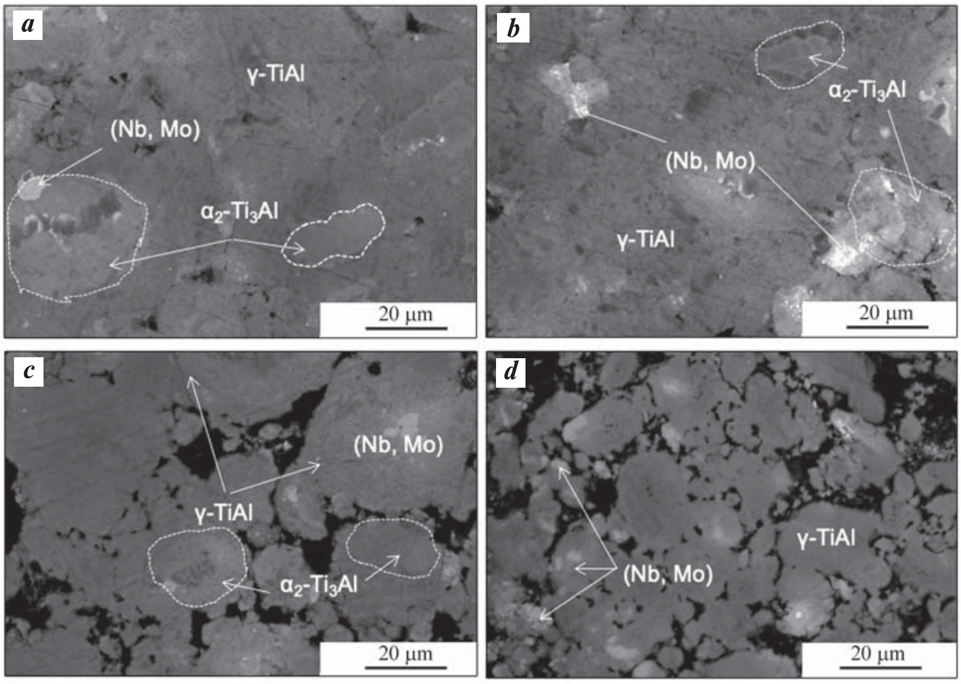

Fig. 3. SHS-sintered samples' structure after the addition of TiH_2 to the reaction mixtures
TiH_2, wt.%: 10 (***a***), 20 (***b***), 30 (***c***), 40 (***d***)

Рис. 3. Структура СВС-спеков, полученных из реакционных смесей с добавлением TiH_2
TiH_2, мас.%: 10 (***a***), 20 (***b***), 30 (***c***), 40 (***d***)

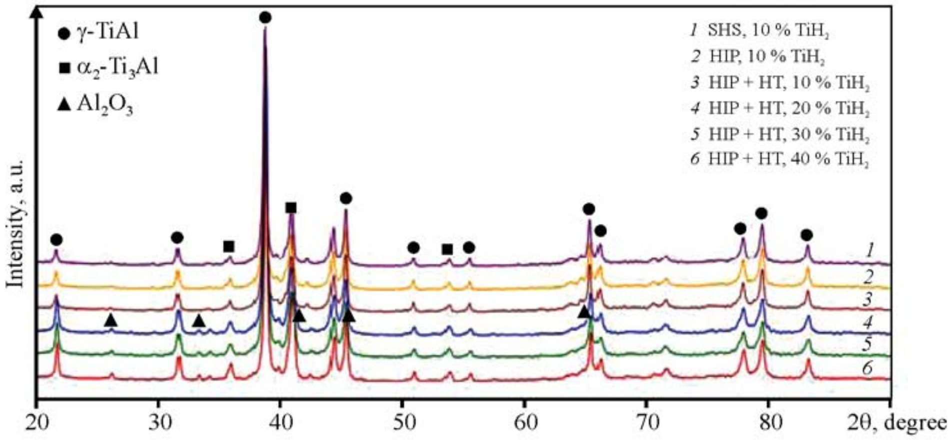

Fig. 4. *X*-ray diffraction patterns of alloy with varying TiH_2 content after SHS, HIP and HIP + HT

Рис. 4. Рентгенограммы сплава с различным содержанием TiH_2 после СВС, ГИП и ГИП + ТО

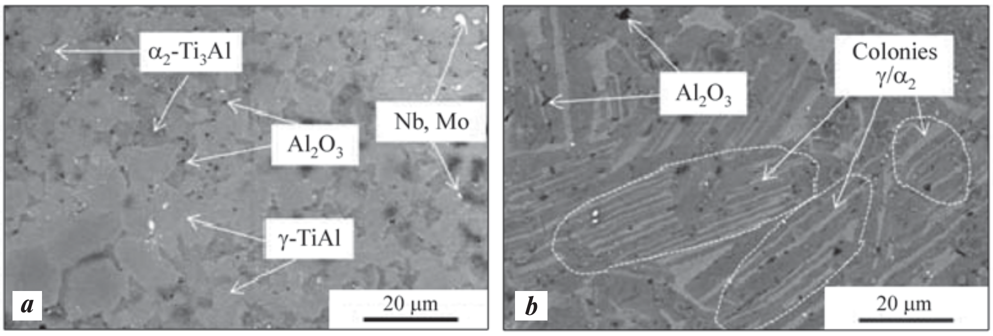

Fig. 5. Structure of the TNM-B1+1%Y_2O_3 alloy with 10% TiH_2 after HIP (***a***) and HIP + HT (***b***)

Рис. 5. Структура сплава TNM-B1+1%Y_2O_3 с 10 % TiH_2 после ГИП (***a***) и ГИП + ТО (***b***)

increases in samples with the addition of 20 % TiH_2 and higher.

Heat treatment of the TNM-B1+1%Y_2O_3 alloy enabled the transformation of its structure from globular to partially lamellar. During heating to 1380 °C, the alloy transitions from the two-phase region ($\alpha + \gamma$) of the phase diagram to the single-phase region (α-Ti), where the γ-TiAl phase dissolves and becomes saturated with aluminum. Upon cooling below the eutectoid transformation temperature, the α phase disintegrates into alternating dispersed lamellae of γ-TiAl and α_2-Ti_3Al, forming colonies. In between these colonies, a small portion of equiaxed grains of the γ-TiAl and α_2-Ti_3Al phases remains.

Structure and mechanical properties of TNM-B1+1%Y_2O_3 alloy after HIP and HIP + HT

The microstructures of TNM-B1+1%Y_2O_3 alloy samples after HIP and HIP + HT, which vary in the TiH_2 content in the initial powders, are depicted in Fig. 6. The alloys exhibit the presence of γ-TiAl and α_2-Ti_3Al phases with equiaxed and lamellar structures, respectively. Additionally, a small amount of dispersed solid solution particles (Nb, Mo) can be observed. As the quantity of TiH_2 in the initial powder mixtures increases, there is a tendency for the occurrence and an increase in the content of Al_2O_3. These Al_2O_3 particles are presented in the form of dispersed particles located along the boundaries of the coarse grains of γ-TiAl and α_2-Ti_3Al.

To ascertain the reasons for the formation of Al_2O_3 in compositions with a high TiH_2 concentration as a precursor, the oxygen and nitrogen contents were analyzed after each technological procedure (HEBM, SHS, and HIP). In this experiment, powder mixtures, SHS products, and consolidated samples served as reference samples, prepared using only metallic titanium as the initial material.

It was found that the oxygen concentration after HEBM exhibited a weak dependence on the TiH_2 content and measured at 0.67 %, 0.57 %, 0.59 %, 0.68 %, and 0.65 %, while the nitrogen concentration was 0.049 %, 0.039 %, 0.043 %, 0.046 %, and 0.052 % for compositions with 0 %, 10 %, 20 %, 30 %, and 40 % TiH_2, respectively. The most substantial increase in impurity oxygen was recorded at the SHS stage, rising from 0.8 % to 2.8 % (Fig. 7). Following the HIP stage, the amount of gas impurities remained nearly unchanged.

Regarding the chemical purity of the alloys, the optimal Ti : TiH_2 ratio was found to be 90 : 10 (Fig. 7). The nature of the dependence of impurity oxygen content on the TiH_2 amount in the initial charge can be explained by two competing factors. On one hand, the presence of TiH_2 in the charge creates a localized reducing atmosphere due to the release of hydrogen during its decomposition in the SHS process. On the other hand, as shown earlier, excessive gas evolution leads to increased residual porosity in SHS-sintered products, an increase in the specific surface area of synthesis products, and adsorption.

The impact of TiH_2 content in the reaction mixtures on the mechanical properties of alloys after HIP and HIP + HT was evaluated using strain diagrams depicting "true compressive stress — logarithmic strain" (Fig. 8). The test results (refer to Table 1) demonstrated that the alloy with a Ti : TiH_2 ratio of 90 : 10 exhibited the highest level of strength properties, with $\sigma_u =$ $= 1200 \pm 15$ MPa and YS = 1030 ± 25 MPa. The reduction in strength and increased brittleness in samples with higher TiH_2 content can be attributed to the embrittling effect of Al_2O_3 particles.

In TNM-B1+1%Y_2O_3 alloys, an improvement in

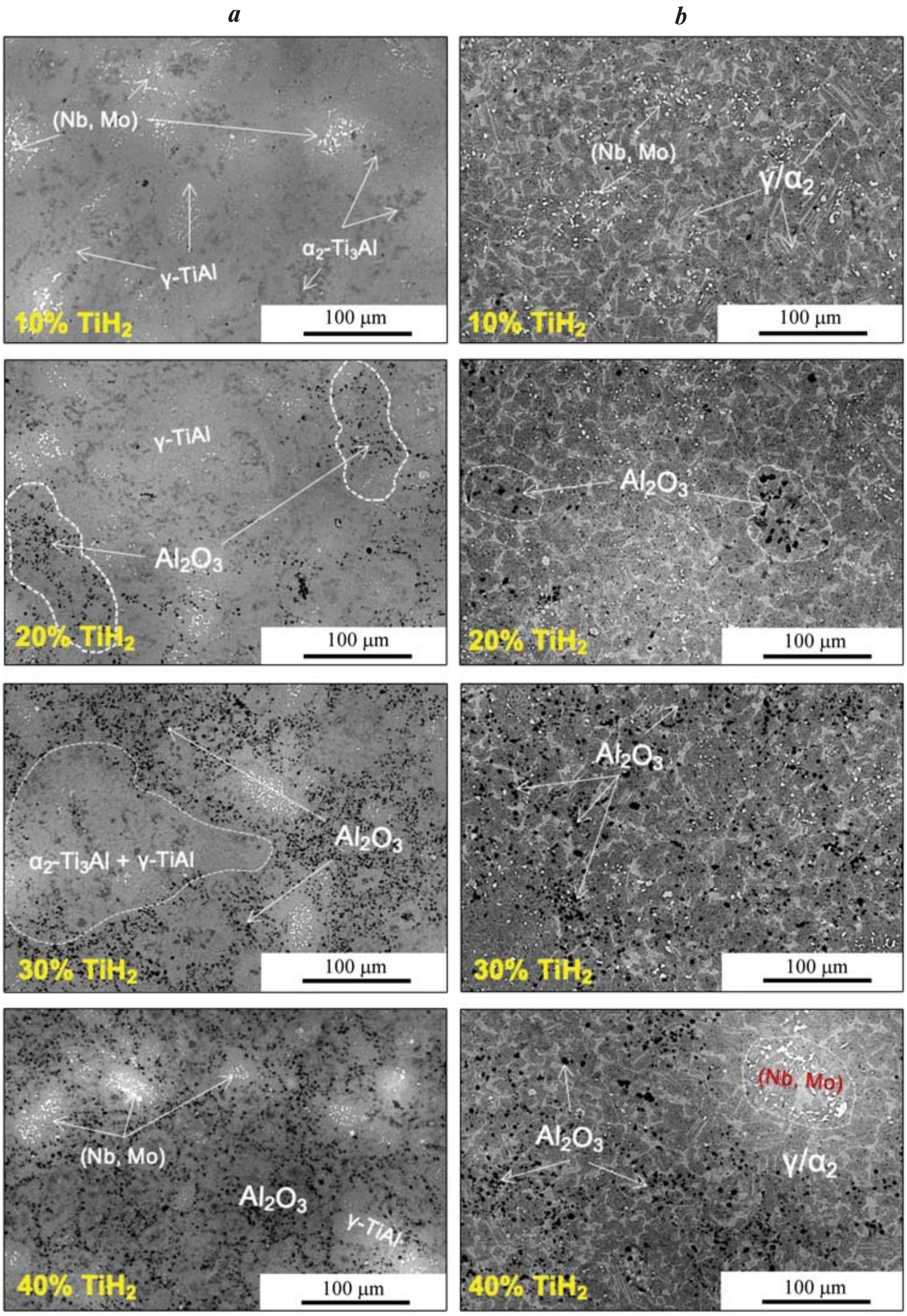

Fig. 6. Structure of the TNM-B1+1%Y_2O_3 alloy after HIP (***a***) and HIP + HT (***b***)

Рис. 6. Структура сплава TNM-B1+1%Y_2O_3 после ГИП (***a***) и ГИП + ТО (***b***)

strength and resistance to plastic deformation was observed after HIP + HT. This can be attributed to the characteristics of the microstructure. The partially lamellar structure results in a decrease in the average size of grains and lamellae inside colonies, from 2.5 to 0.3 μm. This reduction leads to a decrease in the mean free path of dislocations during deformation. Notably, the alloy in which titanium was substituted by its hydride also exhibited the highest strength, with σ_u = = 1253±15 MPa and YS = 1090±30 MPa.

The studied alloys TNM-B1+1%Y_2O_3, both with globular and partially lamellar microstructure, surpassed the classical alloy 4822 [2] and the more intricately doped analogs, Ti—46Al—4Nb—1Mo and Ti—45Al—8.5Nb—0.2W—0.2B [27; 28], in terms of strength.

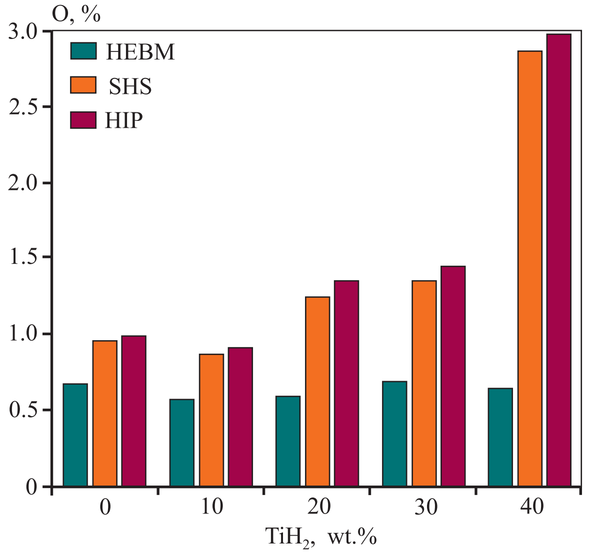

Fig. 7. Content of oxygen impurity in the TNM-B1+1%Y_2O_3 alloy with Ti : TiH_2 varying ratios after HEBM, SHS, and HIP

Рис. 7. Содержание примесного кислорода в сплаве TNM-B1+1%Y_2O_3 с различным соотношением Ti : TiH_2 после ВЭМО, СВС и ГИП

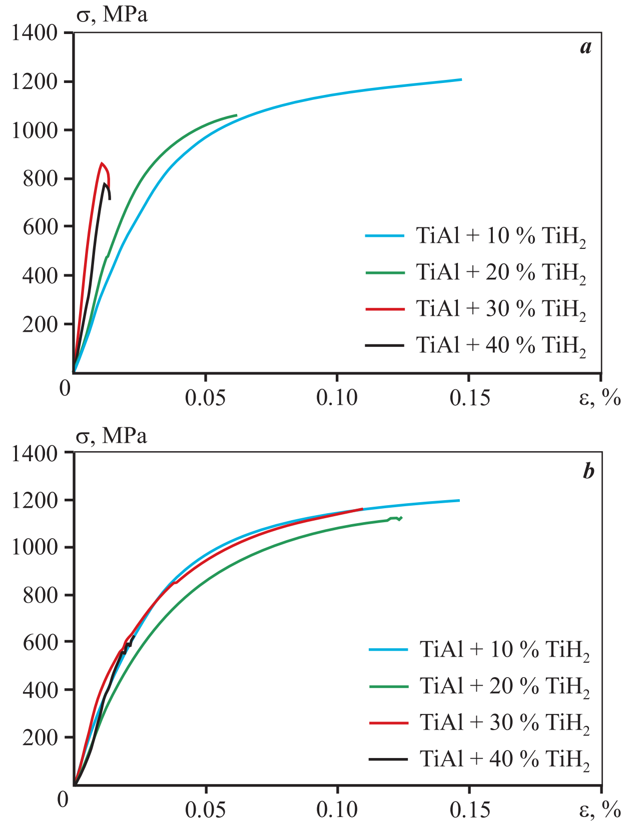

Fig. 8. Stress-strain diagrams for the TNM-B1+1%Y_2O_3 alloy obtained from SHS powders after HIP (***a***) and HIP + HT (***b***)

Рис. 8. Диаграммы логарифмической деформации при сжатии для полученного из СВС-порошков сплава TNM-B1+1%Y_2O_3 после ГИП (***a***) и ГИП + ТО (***b***)

Mechanical properties of the TNM-B1+1%Y_2O_3 alloy compact samples following HIP and HIP + HT

Механические свойства компактных образцов сплава TNM-B1+1%Y_2O_3 после ГИП и ГИП + ТО

Treatment	Content of TiH_2, wt.%	σ_u, MPa	YS, MPa	ε, %
HIP	10	1200±15	1030±25	0.010
	20	1053±50	953±20	0.009
	30	830±45	–	0.007
	40	742±32	–	0.006
HIP + HT	10	1253±15	1090±30	0.010
	20	1122±55	988±25	0.009
	30	1165±58	995±15	0.010
	40	630±25	–	0.005

Conclusions

1. The study investigated the influence of the Ti : TiH_2 ratio in the reaction mixture, along with heat treatment, on the microstructure and mechanical properties of the TNM-B1+1% Y_2O_3 alloy, which was obtained using the HEBM, SHS, and HIP methods. The substitution of 10 % of titanium with its hydride in reaction mixtures led to a reduction in the oxygen content in SHS products from 1.0 % to 0.8 %. This reduction can be attributed to the generation of a reducing atmosphere during the decomposition of TiH_2 in the combustion wave.

2. The maximum mechanical properties of the TNM-B1+1%Y_2O_3 alloy were achieved at a Ti : TiH_2 ratio of 90 : 10, with the compressive strength (σ_u) measuring 1200±15 MPa and YS measuring 1030±25 MPa. However, an increase in the proportion of TiH_2 led to a higher content of oxygen impurity, resulting in the formation of Al_2O_3. This, in turn, reduced the strength and ductility of the material.

3. Heat treatment of the TNM-B1+1%Y_2O_3 alloy transformed the globular structure into a partially lamellar one, resulting in an increase in σ_u by 50—300 MPa, depending on the TiH_2 content. This improvement can be attributed to a reduction in the average grain size and a decrease in dislocation mobility during deformation.

References

1. Burtscher M., Klein T., Lindemann J., Lehmann O., Fellmann H., Güther V., Clemens H., Mayer S. An advanced

TiAl alloy for high-performance racing applications. *Materials.* 2020;13(21):4720. https://doi.org/10.3390/ma13214720

2. Зайцев А.А., Капланский Ю.Ю., Сентюрина Ж.А., Левашов Е.А., Касимцев А.В., Погожев Ю.С., Юдин С.Н., Свиридова Т.А., Маляров А.В. Получение спеченного сплава на основе интерметаллида TiAl. Ч. 2. Исследование процессов формования и спекания. *Известия вузов. Цветная металлургия.* 2016;(1):50—62. https://doi.org/10.17073/0021-3438-2016-1-50-62
   Zaitsev A.A., Kaplanskii Y.Y., Sentyurina Z.A., Levashov E.A., Kasimtsev A.V., Pogozhev Y.S., Yudin S.N., Sviridova T.A., Malyarov A.V. Production of a sintered alloy based on the TiAl intermetallic compound: Pt. 2. Investigation into forming and sintering processes. *Russian Journal of Non-Ferrous Metals.* 2016;57:113—123. https://doi.org/10.3103/S1067821216020139
3. Касимцев А.В., Юдин С.Н., Свиридова Т.А., Маляров А.В., Зайцев А.А., Сентюрина Ж.А., Капланский Ю.Ю., Погожев Ю.С., Левашов Е.А. Получение спеченного сплава на основе интерметаллида TiAl. Ч. 1. Гидридно-кальциевая технология получения порошкового сплава Ti—47Al—2Nb—2Cr и его свойства. *Известия вузов. Цветная металлургия.* 2015;(4): 63—68. https://doi.org /10.17073/0021-3438-2015-4-63-68
   Kasimtsev A.V., Yudin S.N., Sviridova T.A., Malyarov A.V., Zaitsev A.A., Sentyurina Zh.A., Kaplanskii Yu.Yu., Pogozhev Yu.S., Levashov E.A. Production of a sintered alloy based on the TiAl intermetallic compound. Pt. 1: Calcium-hydride fabrication technology of the Ti—47Al—2Nb—2Cr powder alloy and its properties. *Russian Journal of Non-ferrous Metals.* 2015;56:548—554. https://doi.org/10.3103/S1067821215050065
4. Bewlay B.P., Nag S., Suzuki A., Weimer M.J. TiAl alloys in commercial aircraft engines. *Materials at High Temperatures.* 2016;33(4-5):549—559. https://doi.org/10.1080/09603409.2016.1183068
5. Rittinghaus S.K., Zielinski J. Influence of process conditions on the local solidification and microstructure during laser metal deposition of an intermetallic TiAl alloy (GE4822). *Metallurgical and Materials Transactions: A.* 2021;52:1106—1116. https://doi.org/10.1007/s11661-021-06139-2
6. Ostrovskaya O., Badini C., Deambrosis S.M., Miorin E., Biamino S., Padovano E. Protection from oxidation of second and third generation TiAl intermetallic alloys by magnetron sputtering deposition of a TiAl/TiAlN coating. *Materials & Design.* 2021;208:109905. https://doi.org/10.1016/j.matdes.2021.109905
7. Abdoshahi N., Dehghani M., Hatzenbichler L., Spoerk-Erdely P., Ruban A.V., Musi M., Mayer S., Spitaler J., Holec D. Structural stability and mechanical properties of TiAl + Mo alloys: A comprehensive ab initio study. *Acta Materialia.* 2021; 221:117427. https://doi.org/10.1016/j.actamat.2021.117427
8. Полькин И.С., Гребенюк О.Н., Саленков В.С. Интерметаллиды на основе титана. *Технология легких сплавов.* 2010;2:5—15. https://cyberleninka.ru/article/n/intermetallidy-na-osnove-titana-1 (дата обращения 28.09.2023)
   Pol'kin I.S., Grebenyuk O.N., Salenkov V.S. Intermetallic compounds based on titanium. *Tekhnologiya legkikh splavov.* 2010;2:5—15. (In Russ.).
9. Kamyshnykova K., Lapin J. Vacuum induction melting and solidification of TiAl-based alloy in graphite crucibles. *Vacuum.* 2018;154:218—226. https://doi.org/10.1016/j.vacuum.2018.05.017
10. Siheng G., Xianjuan D., Xuan X., Yong X. Effect of ball milling speed and sintering temperature on microstructure and properties of TiAl alloy prepared by powder metallurgy. *Procedia Manufacturing.* 2020;50:355—361. https://doi.org/10.1016/j.promfg.2020.08.066
11. Knörlein J., Franke M.M., Schloffer M., Berger T., Körner C. Microstructure and mechanical properties of additively manufactured γ-TiAl with dual microstructure. *Intermetallics.* 2023;161:107978. https://doi.org/10.1016/j.intermet.2023.107978
12. Wu X. Review of alloy and process development of TiAl alloys. *Intermetallics.* 2006;14(10-11):1114—1122. https://doi.org/10.1016/j.intermet.2005.10.019
13. Loginov P.A., Kaplanskii Y.Y., Markov G.M., Patsera E.I., Vorotilo K.V., Korotitskiy A.V., Shvyndina N.V., Levashov E.A. Structural and mechanical properties of Ti—Al—Nb—Mo—B alloy produced from the SHS powder subjected to high-energy ball milling. *Materials Science and Engineering: A.* 2021;814:141153. https://doi.org/10.1016/j.msea.2021.141153
14. Taguchi K., Ayada M., Ishihara K.N., Shingu P.H. Near-net shape processing of TiAl intermetallic compounds via pseudoHIP-SHS route. *Intermetallics.* 1995;3(2):91—98. https://doi.org/10.1016/0966-9795(95)92673-N
15. Aguilar J., Schievenbusch A., Kättlitz O. Investment casting technology for production of TiAl low pressure turbine blades—Process engineering and parameter analysis. *Intermetallics.* 2011;19(6):757—761. https://doi.org/10.1016/j.intermet.2010.11.014
16. Lagos M.A., Agote I. SPS synthesis and consolidation of TiAl alloys from elemental powders: Microstructure evolution. *Intermetallics.* 2013;36:51—56. https://doi.org/10.1016/j.intermet.2013.01.006
17. Бусурина М.Л., Умаров Л.М., Ковалев И.Д., Сачкова Н.В., Бусурин С.М., Вадченко С.Г., Сычев А.Е. Особенности структуро- и фазообразования в системе

Ti—Al—Nb в режиме теплового взрыва. *Физика горения и взрыва.* 2016;52(6):44—50. https://doi.org/10.1134/S0010508216060058
Busurina M.L., Umarov L.M., Kovalev I.D., Sachkova N.V., Busurin S.M., Vadchenko S.G., Sychev A.E. Features of structure and phase formation in the Ti—Al—Nb system in the thermal explosion mode. *Combustion, Explosion and Shock Waves.* 2016;52(6): 659—664. https://doi.org/10.15372/FGV20160605

18. Mukasyan A.S., Rogachev A.S. Combustion behavior of nanocomposite energetic materials. *Energetic Nanomaterials.* 2016;163—192. https://doi.org/10.1016/B978-0-12-802710-3.00008-8
19. Rak Z.S., Walter J. Porous titanium foil by tape casting technique. *Journal of materials processing technology.* 2006;175(1-3):358—363. https://doi.org/10.1016/j.jmatprotec.2005.04.066
20. Bidaux J.E., García-Gómez J., Hamdan H., Zufferey D., Rodríguez-Arbaizar M., Girard H., Carreno-Morelli E. Tape casting of porous titanium thin sheets from titanium hydride. In: *Proceedings of the Euro PM2011 Congress & Exhibition.* (Barcelona, Spain. 9—12 October 2011). 2011. P. 2.
21. Samal S., Cho S., Park D.W., Kim H. Thermal characterization of titanium hydride in thermal oxidation process. *Thermochimica Acta.* 2012;542:46—51. https://doi.org/10.1016/j.tca.2012.02.010
22. Peillon N., Fruhauf J.B., Gourdet S., Feraille J., Saunier S., Desrayaud C. Effect of TiH_2 in the preparation of MMC Ti based with TiC reinforcement. *Journal of Alloys and Compounds.* 2015; 619:157—164. https://doi.org/10.1016/j.jallcom.2014.09.014
23. Azevedo C.R.F., Rodrigues D., Neto F.B. Ti—Al—V powder metallurgy (PM) via the hydrogenation-dehydrogenation (HDH) process. *Journal of Alloys and Compounds.* 2003;353(1-2):217—227. https://doi.org/10.1016/S0925-8388(02)01297-5
24. Курбаткина В.В., Пацера Е.И., Бодян А.Г., Левашов Е.А. Получение субмикронного порошка на основе TiAl в режиме теплового взрыва. *Цветные металлы.* 2017;2:68—73. https://doi.org/10.17580/tsm.2017.02.11
Kurbatkina V.V., Patsera E.I., Bodyan A.G., Levashov E.A. Preparation of submicron TiAl-based powder in thermal explosion mode. *Tsvetnye metally.* 2017;2:68—73. (In Russ.). https://doi.org/10.17580/tsm.2017.02.11
25. Xu W.C., Huang K., Wu S.F., Zong Y.Y., Shan D.B. Influence of Mo content on microstructure and mechanical properties of β-containing TiAl alloy. *Transactions of Nonferrous Metals Society of China.* 2017;27(4):820—828. https://doi.org/10.1016/S1003-6326(17)60094-3
26. Pan Y., Lu X., Liu C., Hui T., Zhang C., Qu X. Sintering densification, microstructure and mechanical properties of Sn-doped high Nb-containing TiAl alloys fabricated by pressureless sintering. *Intermetallics.* 2020;125:106891. https://doi.org/10.1016/j.intermet.2020.106891
27. Li Z., Luo L., Su Y., Wang B., Wang L., Liu T., Yao M., Liu C., Guo J., Fu H. A high-withdrawing-rate method to control the orientation of $(\gamma + \alpha_2)$ lamellar structure in a β-solidifying γ-TiAl-based alloy. *Materials Science and Engineering: A.* 2020;857:144078. https://doi.org/10.1016/j.msea.2022.144078
28. Qiang F., Kou H., Tang B., Song L., Li J. Effect of cooling rate on microstructure evolution of Ti—45Al—8.5—Nb0.2—W0.2—B0.02—Y alloy during multi-step heat treatment. *Materials Characterization.* 2018;145:210—217. https://doi.org/10.1016/j.matchar.2018.08.031

Information about the authors

Georgy M. Markov – Junior Research Scientist of the “In situ Diagnostics of Structural Transformations” Laboratory of Scientific Educational Center of Self Propagating High-Temperature Synthesis (SEC SHS), MISIS–ISMAN, National University of Science and Technology (NUST) “MISIS”.
https://orcid.org/0000-0001-7285-7888
E-mail: markov.sci@gmail.com

Pavel A. Loginov – Cand. Sci. (Eng.), Senior Research Scientist of the “In situ Diagnostics of Structural Transformations” Laboratory of SEC SHS, MISIS–ISMAN.
https://orcid.org/0000-0003-2505-2918
E-mail: pavel.loginov.misis@list.ru

Nataliya V. Shvyndina – Leading Engineer of SEC SHS, MISIS–ISMAN.
https://orcid.org/0000-0002-4662-544X
E-mail: natali19-03@list.ru

Информация об авторах

Георгий Михайлович Марков – мл. науч. сотрудник лаборатории «In situ диагностика структурных превращений» научно-учебного центра (НУЦ) СВС, МИСИС–ИСМАН, Национальный исследовательский технологический университет (НИТУ) «МИСИС».
https://orcid.org/0000-0001-7285-7888
E-mail: markov.sci@gmail.com

Павел Александрович Логинов – к.т.н., ст. науч. сотрудник лаборатории «In situ диагностика структурных превращений» НУЦ СВС, МИСИС–ИСМАН.
https://orcid.org/0000-0003-2505-2918
E-mail: pavel.loginov.misis@list.ru

Наталия Владимировна Швындина – вед. инженер НУЦ СВС, МИСИС–ИСМАН.
https://orcid.org/0000-0002-4662-544X
E-mail: natali19-03@list.ru

Fedor A. Baskov – Cand. Sci. (Eng.), Research Scientist of the "In situ Diagnostics of Structural Transformations" Laboratory of SEC SHS, MISIS–ISMAN, Head of Sector, JSC "Composite".
https://orcid.org/0000-0001-6238-4378
E-mail: baskov_fa@mail.ru

Evgeny A. Levashov – Dr. Sci. (Eng.), Professor, Full Member of Russian Academy of Natural Science, Head of Department of Powder Metallurgy and Functional Coatings, NUST "MISIS", Head of SEC SHS, MISIS–ISMAN.
https://orcid.org/0000-0002-0623-0013
E-mail: levashov@shs.misis.ru

Федор Алексеевич Басков – к.т.н., науч. сотрудник лаборатории «In situ диагностика структурных превращений» НУЦ СВС, МИСИС–ИСМАН, начальник сектора АО «Композит».
https://orcid.org/0000-0001-6238-4378
E-mail: baskov_fa@mail.ru

Евгений Александрович Левашов – д.т.н., проф., академик РАЕН, академик Всемирной академии керамики, зав. кафедрой порошковой металлургии и функциональных покрытий НИТУ «МИСИС», директор НУЦ СВС, МИСИС–ИСМАН.
https://orcid.org/0000-0002-0623-0013
E-mail: levashov@shs.misis.ru

Contribution of the authors

Georgy M. Markov – formulated the research purpose, prepared initial materials, conducted experiments, and wrote the manuscript.

Pavel A. Loginov– formulated the research purpose, participated in result discussions, and reviewed and edited the article.

Natalia V. Shvyndina – conducted microscopy examinations and participated in result discussions.

Fedor A. Baskov – carried out sample compaction and participated in result discussions.

Evgeniy A. Levashov – contributed to the conceptualization and supervised the article, participated in result discussions.

Вклад авторов

Г.М. Марков – определение цели работы, подготовка исходных материалов, проведение экспериментов, написание текста статьи.

П.А. Логинов – определение цели работы, участие в обсуждении результатов, проведение обзора и редактирование статьи.

Н.В. Швындина – проведение микроскопических исследований, участие в обсуждении результатов.

Ф.А. Басков – проведение компактирования образцов, участие в обсуждении результатов.

Е.А. Левашов – концептуализация и проверка статьи, участие в обсуждении результатов.

The article was submitted 28.09.2023, revised 11.10.2023, accepted for publication 13.10.2023

Статья поступила в редакцию 28.09.2023, доработана 11.10.2023, подписана в печать 13.10.2023

PHYSICAL METALLURGY AND HEAT TREATMENT / МЕТАЛЛОВЕДЕНИЕ И ТЕРМИЧЕСКАЯ ОБРАБОТКА

UDC 669.017:669.3 + 621.721.1
https://doi.org/10.17073/0021-3438-2023-6-66-83

Research article
Научная статья

Restoration of continuous casting machine mold copper plates made of Cr–Zr bronze using multi-pass friction stir lap welding

A.V. Makarov[1], **N.V. Lezhnin**[1], **A.B. Kotelnikov**[2], **A.A. Vopneruk**[2], **Yu.S. Korobov**[1,3], **A.I. Valiullin**[1], **E.G. Volkova**[1]

[1] **M.N. Mikheev Institute of Metal Physics of Ural Branch of Russian Academy of Sciences**
18 S. Kovalevskaya Str., Yekaterinburg 620108, Russia

[2] **R&D Enterprise "Mashprom"**
5 Krasnoznamennaya Str., Yekaterinburg 620143, Russia

[3] **Ural Federal University named after the First President of Russia B.N. Yeltsin**
19 Mira Str., Yekaterinburg 620002, Russia

✉ Alexey V. Makarov (av-mak@yandex.ru)

Abstract: An innovative technology has been developed and implemented for the restoration and manufacturing of new mold copper plates for continuous casting machines (CCMs) using wear-resistant composite coatings. These copper plates significantly surpass the service life of imported copper plates featuring galvanic coatings, sometimes by up to 20 times. However, the pressing challenge of restoring the copper plates of molds once they have reached the minimum permissible thickness remains unresolved. This study aimed to explore the feasibility of restoring a plate composed of precipitation-hardening Cr–Zr bronze with the same material by employing friction stir lap welding (FSLW). The objectives were to examine the structure, quality, and hardness of the welded joint, alongside investigating the impact of heat treatment (quenching and aging). By utilizing multi-pass FSLW method with a rotating tool crafted from a heat-resistant alloy and overlapping (partially overlapping) successive passes, a welded joint with a thickness of ~5 mm was achieved, devoid of critical continuity flaws (cracks or voids). Within the bronze layer restored through FSW, a softening effect ranging from 85–105 HV1 was observed compared to the initial hardness of the bronze in its hardened and aged state while in service (116–126 HV1). This is attributed to recrystallization and overaging, specifically the coarsening of chromium particles within the Cr–Zr bronze due to the heating of the weld nugget (stir zone) to 600–700 °C. The observed softening effect during FSW can be effectively rectified through heat treatment involving dissolution of the hardening phases followed by aging, resulting in a hardness increase to approximately 120–150 HV1. The process of restoring copper plates to their original thickness via the progressive and environmentally friendly FSW method, followed be the subsequent application of wear-resistant composite coatings, presents the opportunity for an almost infinite operational cycle of molds. This advancement could potentially eradicate the necessity for Russia to rely on importing such molds copper plates.

Keywords: mold copper plate, restoration, bronze, friction stir lap welding (FSLW), hardness, structure, hardening, aging.

Acknowledgments: This research received support from the Ministry of Science and Higher Education of the Russian Federation (Research topic "Structure" No. 122021000033-2) and from the integrated project titled "Development of new materials and technologies for the formation of coatings resistant to abrasive and corrosive wear" (Ural Interregional Research and Education Center for Advanced Production Technologies and Materials). The work used equipment from the Shared Use Center "Testing Center for Nanotechnologies and Advanced Materials" (Institute of Physics and Mathematics, Ural Branch, Russian Academy of Sciences).

For citation: Makarov A.V., Lezhnin N.V., Kotelnikov A.B., Vopneruk A.A., Korobov Yu.S., Valiullin A.I., Volkova E.G. Restoration of continuous casting machine mold copper plates made of Cr–Zr bronze using multi-pass friction stir lap welding. *Izvestiya. Non-Ferrous Metallurgy*. 2023;29(6):66–83. https://doi.org/10.17073/0021-3438-2023-6-66-83

Восстановление стенок кристаллизаторов машин непрерывного литья заготовок из хромоциркониевой бронзы методом многопроходной сварки трением с перемешиванием

А.В. Макаров[1], **Н.В. Лежнин**[1], **А.Б. Котельников**[2], **А.А. Вопнерук**[2], **Ю.С. Коробов**[1,3], **А.И. Валиуллин**[1], **Е.Г. Волкова**[1]

[1] **Институт физики металлов им. М.Н. Михеева УрО РАН**
Россия, 620108, г. Екатеринбург, ул. С. Ковалевской, 18

[2] **ЗАО «НПП “Машпром”»**
Россия, 620143, г. Екатеринбург, ул. Краснознамённая, 5

[3] **Уральский федеральный университет имени первого Президента России Б.Н. Ельцина**
Россия, 620002, г. Екатеринбург, ул. Мира, 19

✉ Алексей Викторович Макаров (av-mak@yandex.ru)

Аннотация: Разработана и практически реализована инновационная технология восстановительного ремонта и производства новых стенок кристаллизаторов машин непрерывного литья заготовок (МНЛЗ) с износостойкими композиционными покрытиями, значительно (до 20 раз) превосходящих ресурс импортных стенок с гальваническими покрытиями. Однако нерешенной остается актуальная задача восстановления медных стенок (плит) кристаллизаторов после достижения ими минимально допустимой толщины. Целью работы являлось исследование возможности восстановления плиты из дисперсионно-твердеющей хромоциркониевой бронзы марки БрХЦр этим же материалом с использованием сварки трением с перемешиванием (СТП), изучение структуры, качества и твердости сварного соединения, а также влияния на его структуру и твердость термической обработки (закалки и старения). С применением многопроходной плоскостной СТП вращающимся инструментом из жаропрочного сплава при наложении (частичном перекрытии) последовательных дорожек получено сварное соединение толщиной ~5 мм без критичных дефектов сплошности (трещин, пор). В восстановленном способом СТП слое бронзы обнаружено разупрочнение до 85–105 HV1 по сравнению с исходной твердостью бронзы в закаленном и состаренном состоянии плиты, бывшей в эксплуатации (116–126 HV1). Это связано с рекристаллизацией и перестариванием (укрупнением частиц хрома) в Cr–Zr-бронзе в результате нагрева ядра сварки (зоны перемешивания) до температур 600–700 °C. Отмеченное разупрочнение при СТП может быть эффективно устранено термической обработкой (закалкой с последующим старением), приводящей к повышению твердости до 120–150 HV1. Восстановление медных плит до первоначальной толщины прогрессивным экологичным методом СТП с последующим нанесением износостойких композиционных покрытий открывает перспективы практически бесконечного цикла эксплуатации кристаллизаторов и исключения потребности России в их импорте.

Ключевые слова: плита кристаллизатора, восстановительный ремонт, бронза, сварка трением с перемешиванием (СТП), твердость, структура, закалка, старение.

Благодарности: Работа выполнена в рамках государственного задания Минобрнауки России (тема «Структура», № 122021000033-2) и комплексного проекта «Разработка новых материалов и технологий для формирования покрытий, стойких в условиях абразивного и коррозионного изнашивания» УМНОЦ мирового уровня «Передовые производственные технологии и материалы». Работа выполнена с использованием оборудования ЦКП «Испытательный центр нанотехнологий и перспективных материалов» ИФМ УрО РАН.

Для цитирования: Макаров А.В., Лежнин Н.В., Котельников А.Б., Вопнерук А.А., Коробов Ю.С., Валиуллин А.И., Волкова Е.Г. Восстановление стенок кристаллизаторов машин непрерывного литья заготовок из хромоциркониевой бронзы методом многопроходной сварки трением с перемешиванием. *Известия вузов. Цветная металлургия*. 2023;29(6):66–83.
https://doi.org/10.17073/0021-3438-2023-6-66-83

Introduction

Continuous casting machines (CCMs) (Fig. 1, *a*) contribute to more than 96 % of global steel production [1]. The main technological component of the CCM is the mold, wherein the crucial consumable element comprises water-cooled plates made from copper alloys (Fig. 1, *b*). To decrease wear resulting from friction with the solidifying slab shell, the thermal effects of liquid and solidifying metal, as well as corrosive wear of the copper plates in the lower part of the mold [2], protective coatings are applied to the working surface of these copper plates.

The dependency on imported copper plates featuring protective galvanic coatings in Russian metallurgical plants was notably high, reaching 97 % in 2012. This heavy reliance is critical for Russian national safety. The exit of foreign manufacturers and suppliers of plates from the Russian market poses a tangible threat to the Russian steel industry. Over the period spanning from the 1960s to the 2000s, advancements in the composition of galvanic coatings led to a significant rise in the average durability of copper plates, escalating from 100 to 1000 heats [1].

Nevertheless, the imported galvanic coatings employed as protective coatings present significant drawbacks: notable susceptibility to wear and tear (Fig. 2, *a*), the occurrence of thermal cracks within the coating (Fig. 2, *b*), alongside high costs and limited environmental friendliness associated with the galvanization method.

In Russia, a collaborative endeavor involving specialists from R&D Enterprise “Mashprom”, JSC, Institute of Metal Physics, Institute of Engineering Science of Ural Branch of the Russian Academy of Sciences, Ural Federal University, and several metallurgical enterprises has successfully developed and implemented an innovative technology for the restorative repair and production of new copper plates for CCM molds, integrating wear-resistant composite coatings [1; 3] (Fig. 3).

During the development of this new domestic technology, a series of pivotal tasks were addressed:

— formulation of metal-ceramic powder mixtures for wear-resistant coatings was achieved by using powders within the Ni—Cr alloying system, incorporating carbides (WC, Cr_3C_2, SiC, TiC), borides (CrB_2, TiB_2), and metallic (Cr, Mo) compounds. Additionally, a unique technology involving robotic high velocity air fuel (HVAF) thermal spraying for applying coatings was created [1; 4];

— scientific substantiation of the optimal application efficacy of composite coatings containing substantial strengthening phases was accomplished [5];

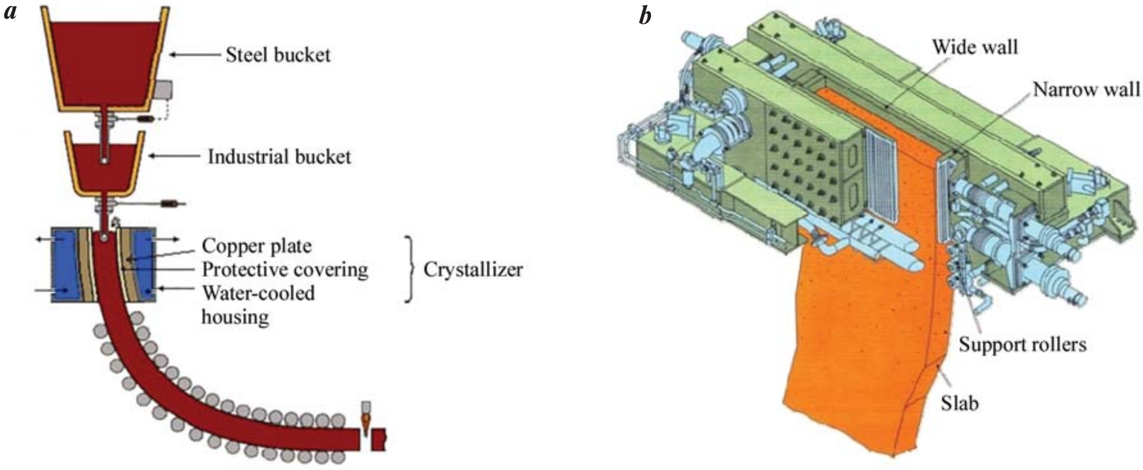

Fig. 1. Schematic view of the slab continuous casting machine (CCM) (***a***) and mold design for the slab CCM (***b***)

Рис. 1. Схема машины непрерывного литья заготовок (***a***) и конструкция кристаллизатора слябовой МНЛЗ (***b***)

Fig. 2. Electroplated coatings defects: wear (***a***) and heat cracks (***b***)

Рис. 2. Дефекты гальванических покрытий: износ (***a***) и тепловые трещины (***b***)

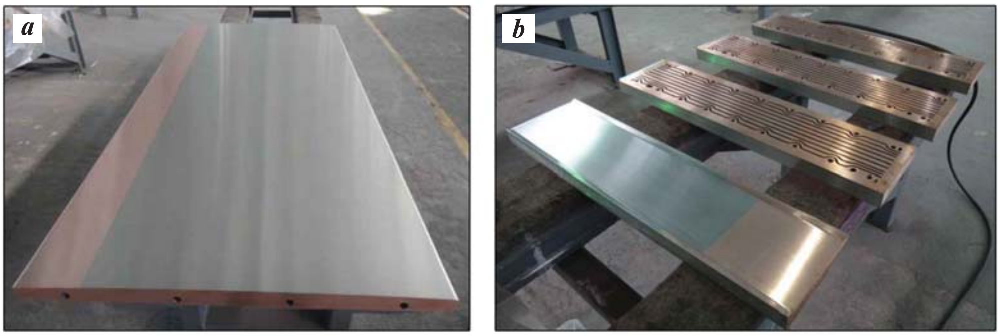

Fig. 3. Slab CCM mold plates: wide (***a***) and narrow (***b***)

Рис. 3. Широкая (***а***) и узкие (***b***) стенки кристаллизатора слябовой МНЛЗ

— a methodology was developed, enabling the reinforcement of copper alloy and enhancing the heat and wear resistance of the coating. This was achieved through the implementation of a new scientific phenomenon wherein a wear-resistant framework composed of coarse carbide and boride particles is formed during annealing [6—9].

During industrial trials conducted at Russian metallurgical enterprises such as MMK, EVRAZ NTMK, Severstal, NLMK, OMK-Steel, and others, it was determined that the durability of the innovative mold copper plates increased significantly, ranging from 4 to 20 times when compared to imported counterparts equipped with galvanic coatings. Simultaneously, these advancements led to an enhancement in the quality of produced billets. The wear resistance of the composite coatings has demonstrated an ability to endure up to 700 thousand tons of cast steel within a single overhaul cycle. The integration of this technology into the production complex of R&D Enterprise "Mashprom" in Nizhny Tagil surpasses the production capabilities of foreign companies that rely on galvanic production. This superiority extends across environmental safety, energy efficiency, and resource utilization. The development entirely aligns with the objectives outlined in the action plan of the Russian Ministry of Industry and Trade, specifically addressing the need for import substitution in heavy machine building. Following the successful implementation of this technology in major Russian Steelmakers, the proportion of foreign slab molds utilized in domestic steel mills decreased substantially, reaching 40 % by the end of 2022.

The pressing challenge of restoring copper plates in molds after reaching the minimum allowable thickness remains unresolved. When the loss of copper plate material reach 10—15 mm due to wear and repair cycles (Fig. 4), the costly plate with cooling channels is typically discarded as it no longer meets the necessary mechanical characteristic requirements.

Presently, the restoration of copper plates of continuous casting molds primarily relies on arc welding using a non-consumable electrode within inert gases (Fig. 5). However, this process exhibits low manufacturability concerning this specific product due to the metallurgical intricacies involved in welding this material. Copper and its alloys possess distinctive attributes such as high thermal conductivity, heat capacity, coefficient of thermal expansion, and a susceptibility to forming hot cracks and pores. Notably, within the temperature range of $t = 250 \div 550$ °C, copper experiences a reduction in strength and ductility [10]. These properties necessitate the preheating of a solid plate during TIG welding, within a fairly narrow temperature range of approximately 350±10 °C. Throughout the TIG welding process on a solid plate, maintaining the temperature within this narrow range proves challenging. This difficulty significantly escalates the labor intensity compared to volume-based metal deposition estimations. The constant

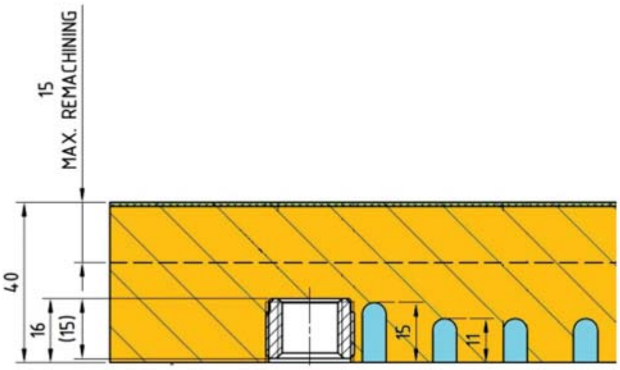

Fig. 4. Schematic diagram of the copper CCM mold plate
Dimensions in mm

Рис. 4. Конструкция медной плиты кристаллизатора МНЛЗ
Размеры указаны в мм

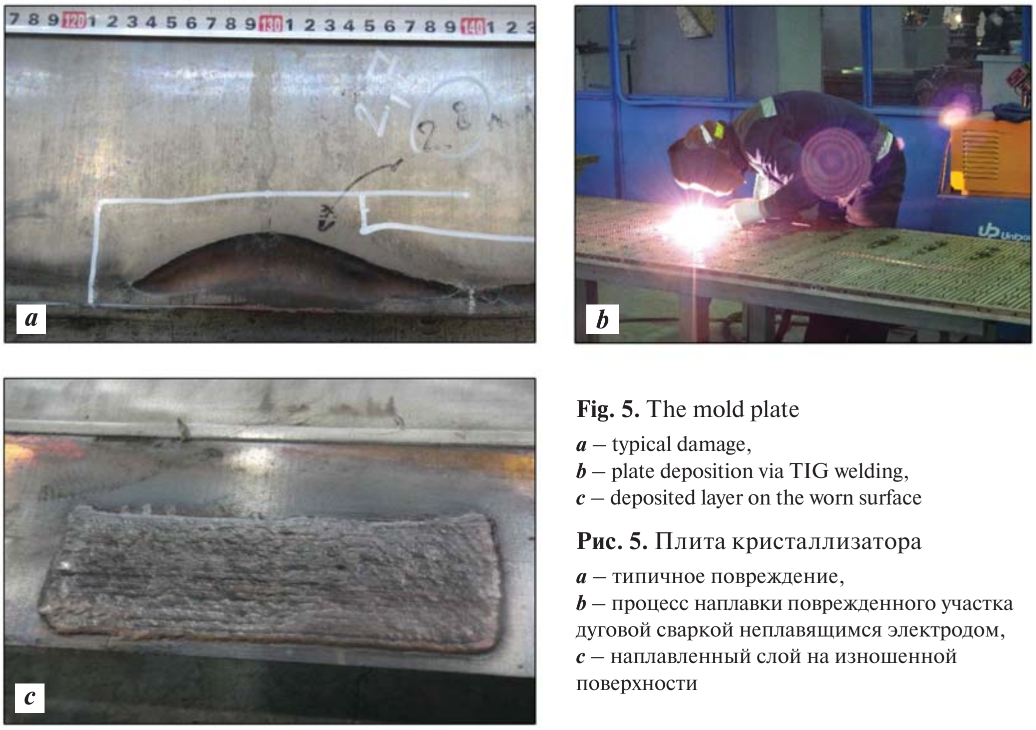

Fig. 5. The mold plate

a – typical damage,
b – plate deposition via TIG welding,
c – deposited layer on the worn surface

Рис. 5. Плита кристаллизатора

a – типичное повреждение,
b – процесс наплавки поврежденного участка дуговой сваркой неплавящимся электродом,
c – наплавленный слой на изношенной поверхности

need for plate heating, labor costs to rectify defects, and the inconsistent quality of the deposited metal amplify labor requirements. Moreover, this technology poses environmental hazards and risks to the welder's health.

Consequently, the information presented in Fig. 5 cannot be deemed a viable restoration technology for extensive surface areas of plates, let alone for full-size plates.

The utilization of specialized solid-state welding methods such as diffusion welding [11], explosion welding [12], and ultrasonic welding [13] for the aforementioned purposes is unfeasible. The impossibility of using laser techniques arises from the high reflectivity exhibited by copper (95 %) and Cu—Cr—Zr alloy (90 %) when exposed to fiber optic and other solid-state lasers emitting at a wavelength (λ) of 1064 nm, which is standard in most complexes used for laser cladding and additive manufacturing [14; 15]. This reflective property hinders the application of modern laser technologies for the restoration of copper plates. The absorption capacity of copper and chromium-zirconium bronze significantly increases only for ultrashort wavelengths (less than 550 nm) of electromagnetic radiation. However, powerful technological laser installations utilizing green ($\lambda = 510 \div 532$ nm) and blue ($\lambda = 360 \div \div 480$ nm) lasers have yet to be developed. Consequently, the restoration of copper plates of CCM molds is most promisingly addressed by advancing an environmentally friendly friction stir welding (FSW) technology to resolve these challenges.

The FSW technology, initially proposed in the Soviet Union [16] and subsequently patented by the British Institute of Welding in 1991 [17], facilitates the joining of materials in a solid state by employing a rotating tool to stir the materials. This process induces a plastic state in the material due to frictional heating without reaching a melting point, resulting in the formation of a weld through mechanical stirring of the metal in the workpieces [18—20]. FSW operates at relatively low temperatures, circumventing issues associated with conventional fusion welding, such as overheating and related crystallization defects like porosity, cast structure, and crystallization cracks. Since the early 2000s, active research has been conducted on FSW and Friction Stir Processing (FSP) of pure copper [21—23] and nickel aluminum bronze [24; 25]. Extensive studies have focused on creating dissimilar welded joints involving copper alloys [26; 27], copper or bronze in combination with other metals [28—31], and analyzing structural patterns during FSW of copper [21]. Additionally, investigations have explored phase transformations and various properties of surface-modified FSP cast nickel-aluminum bronzes, encompassing corrosion and cavitation resistance, as well as fatigue resistance [18; 32—34]. Specific studies have delved into the characteristics of FSW involving Cu—Cr—Zr alloys [35; 36].

In a study [37], the potential for restoring CCM mold copper plates using the FSW method with a Cu—Ag alloy is discussed. Moreover, research has demonstrated the capability of joining pure copper plates with thicknesses of 16—22 mm to copper plates with thicknesses of 2.5—5.0 mm using FSW [38]. The intricacies of FSLW of a 5 mm thick plate made of pure copper to a fragment of a mold plate, composed of Cr—Zr bronze, were examined [39]. However, it's noteworthy that in studies [37; 39], the welding was conducted in separate tracks rather than over the entire surface.

To restore substantial sections of the plate, multi-pass FSLW involving the sequential overlap of welds is necessary, subjecting the metal to thermomechanical influence during joint performance. Achieving complete restoration of a Cr—Zr bronze plate is best accomplished using the same bronze material as a filler rather than pure copper, as detailed in [38]. This study demonstrated that, under specific FSW conditions, a welded copper joint exhibited nearly equal strength compared to a copper base. When restoring Cr—Zr bronze with a pure copper plate in the welding zone, an increase in microhardness to 150—190 HV1 was observed compared to the original coarse-grained bronze with a hardness of 110—130 HV1. This rise was attributed to the formation of an ultrafine structure (0.5—1.0 μm) resulting from FSW and dispersion strengthening of the alloy using nano-sized particles of chromium and the Cu_5Zr intermetallic compound [39].

However, in the case of multi-pass FSLW of thick Cu—Cr—Zr alloy plate, high temperatures within the mixing zone led to adverse effects such as grain growth, dissolution and coarsening of strengthening phases. This resulted in a detrimental impact on the mechanical and physical properties of the material [40]. The structure and strength properties of Cr—Zr bronze can be significantly influenced by both the thermomechanical effects during multipass FSLW and subsequent heat treatment processes, particularly hardening and aging, which are commonly employed for dispersion-hardening alloys.

The objective of this study is to investigate the potential for restoring a plate made of dispersion-strengthened Cr—Zr bronze using the same material through the multi-pass friction stir lap welding method while applying consecutive joints with partial overlay. Additionally, the study aims to analyze the structure, integrity, and hardness of the welded joint, as well as to assess the impact of heat treatment (quenching and aging) on its structure and hardness.

Materials and methods

The foundational material comprised a 38 mm thick plate, constituting the copper plate of a CCM mold. Made from precipitation-hardening chromium zirconium bronze, it underwent hardening, aging, and subsequent operational phases. Additionally, a 5 mm thick bronze plate with identical chemical composition served as filler material, wt.%: 98.82—99.57 Cu; 0.80 Cr; 0.13 Zr; <0,03.Ni; <0.01 As; <0.003 Pb; <0.01 Zn; <0.002 Bi; <0.01 Sn; <0.1 impurities. Unlike solid solution strengthened alloys, which exhibit reduced thermal conductivity due to dissolved alloying elements, the precipitation-strengthened Cu—Cr—Zr alloy offers both high strength and superior thermal conductivity [41]. The remarkably low solubility of chromium and zirconium in copper at temperatures below 600 °C facilitates the creation of an alloy matrix primarily composed of pure copper, thereby ensuring high thermal conductivity. Meanwhile, finely dispersed particles of chromium and the intermetallic compound Cu_5Zr serve as strengthening phases, significantly enhancing the alloy's strength and heat resistance following thermal aging. Chromium plays an important role in dispersion strengthening, whereas zirconium contributes to elevating the recrystallization temperature, thereby enhancing heat resistance.

To bond the plates through an "overlap" technique, a portal welding setup was utilized at the Institute of Metal Physics of Ural Branch of the Russian Academy of Sciences (Fig. 6, *a*). The workpiece was secured onto the welding table using the equipment depicted in Fig. 6, *b*. For the welding process, a specialized welding tool crafted from the heat-resistant alloy was employed. This tool featured a conical threaded pin, 6 mm in length, with a base diameter of 8 mm tapering down to 6 mm at the tip (Fig. 7, *a*). As illustrated in Fig. 7, this rotating welding tool was angled at $\alpha = 3°$ opposite to the welding direction and immersed into the filler plate, thereby generating a zone of superplasticity. The heat necessary for welding was produced through the friction between the rotating tool's pin and the shoulder, combined with intense plastic deformation of the metal plate. The heating process resulted in the plasticization of the material around the pin. As the tool moved forward, it mechanically transferred the material from the front to the back edge of the tool, effectively filling the weld. The tool's shoulder applied pressure to the plate's surface, ensuring that the flow of plasticized metal remained close to it. Consequently, a welded joint was formed without requiring the material to melt.

Multi-pass lap welding was executed through a sequence of successive passes, with a seam axis step of 6 mm, which accounts for 0.86 of the average diameter of the tool's conical pin, measuring 7 mm. The welding parameters were as follows: load $S = 13.7\div15.7$ kN, spindle

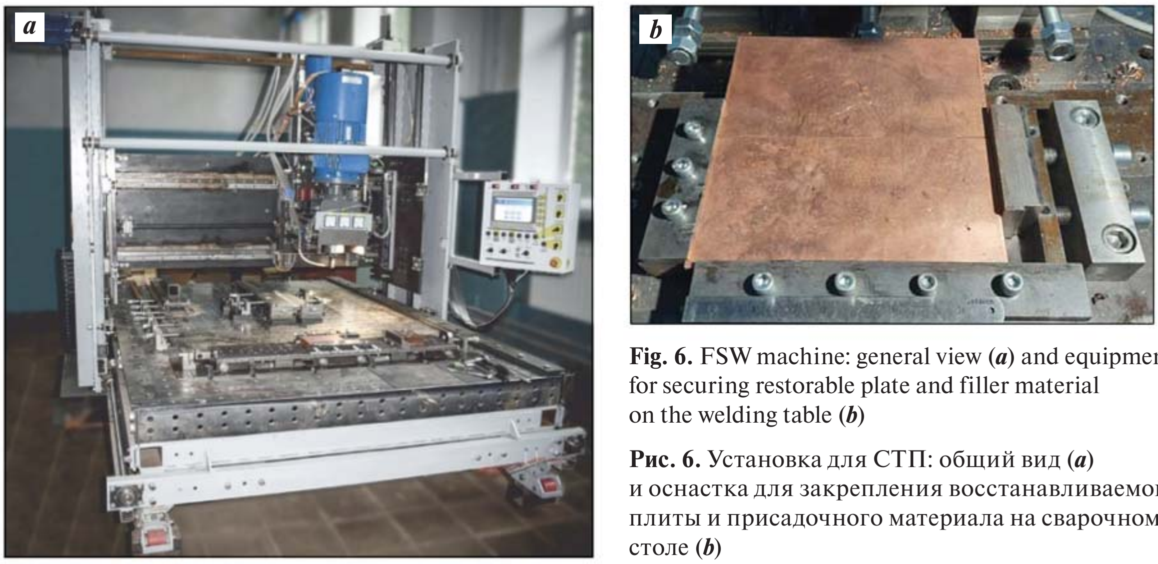

Fig. 6. FSW machine: general view (***a***) and equipment for securing restorable plate and filler material on the welding table (***b***)

Рис. 6. Установка для СТП: общий вид (***a***) и оснастка для закрепления восстанавливаемой плиты и присадочного материала на сварочном столе (***b***)

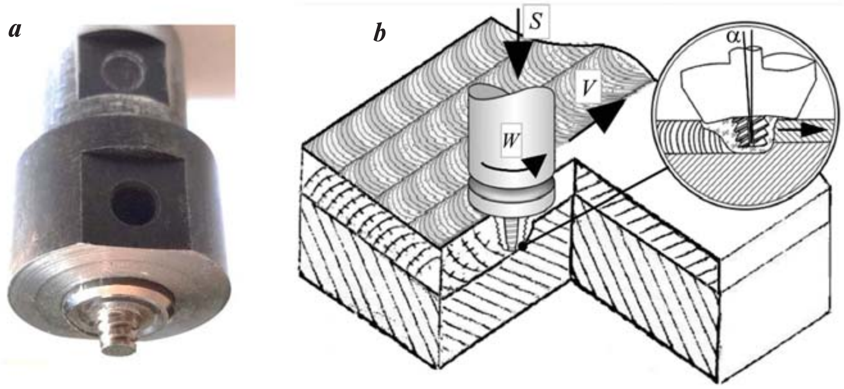

Fig. 7. Heat-resistant stir tool (***a***) and schematic drawing of multi-pass FSLW (***b***)
S – load, W – tool rotational speed, V – longitudinal welding velocity, α – tilt angle

Рис. 7. Внешний вид сварочного инструмента из жаропрочного сплава (***a***) и схема процесса плоскостной СТП (***b***)
S – нагрузка; W – скорость вращения инструмента, об/мин; V – скорость сварки, мм/мин; α – угол наклона, град

(tool) rotation speed $W = 900$ rpm, and welding speed $V = 30$ mm/min (refer to Fig. 7, *b*). Throughout the welding process, the parts were cooled by directing an air jet onto them. The temperature at the periphery of the tool shoulder was monitored using a DGE 10NV non-contact laser pyrometer (DIAS_Pyrospot, Germany).

Following FSW, a heat treatment procedure was implemented, involving quenching from 1050 °C (held for $\tau = 1$ hour in an evacuated ampoule) in water, followed by aging at $t = 450$ °C ($\tau = 1$ hour, cooled in air).

The macrostructure of the samples was examined through optical microscopy after etching in a 50 % aqueous solution of nitric acid. This analysis was conducted on transverse metallographic sections perpendicular to the passages of the welding tool. The fine structure was scrutinized using Transmission Electron Microscopy (TEM) using thin foils. For assessing hardness, a Vickers indenter with a load of 1 kg was employed via a Qness 10A+ automated hardness tester (Qness, Austria). Comprehensive data was obtained, including 2D maps, 3D hardness distribution profiles, and hardness distribution curves along the depth of the welded joint. This involved conducting 10 measurements at various depths to ascertain the hardness characteristics.

Results and discussion

Figure 8, *a* presents an overall view of the plate surface, which was reconstructed through multi-pass FSLW, displaying overlapped tracks from individual passes of the welding tool. The examination of the macrostructure of the welded joint on a transverse section (across the passages) revealed specific characteristics (Fig. 8, *b*): the structure of the used bronze plate exhibited large recrystallized grains, measuring between 5 to 20 mm.

As documented in [39], scanning electron microscopy reveals spherical particles of pure chromium featuring a BCC lattice, measuring 1—5 μm in size, distributed within the grains of a metal matrix. Additionally, rod-shaped particles, reaching up to 1 μm in size and representing Cu_5Zr with a complex face-centered cubic lattice type Be_5Au [43], were observed. Optical microscopy (Fig. 9, *a*) also distinctly highlighted the presence of round chromium particles, up to 5 μm in size, within the plate's structure. Their existence in the original plate structure following hardening, aging, and prolonged operational use can be attributed to the limited solubility of chromium in copper, which, even at t = 1050 °C, does not exceed 0.6 wt.% [41].

Transmission electron microscopy observations revealed the existence of a specific quantity of dislocations within the copper grains (Fig. 10). However, the elevated hardness of the restored CCM mold plate, measuring between 116—126 HV1 (Fig. 11 and 12, curve *1*), is primarily attributed not only to these structural characteristics but predominantly to the presence of pre-deposits in the aged bronze, specifically Guinier—Preston zones, and nanodispersed chromium particles that are coherent with the matrix. These elements generate elastic stress fields within the matrix [44—46].

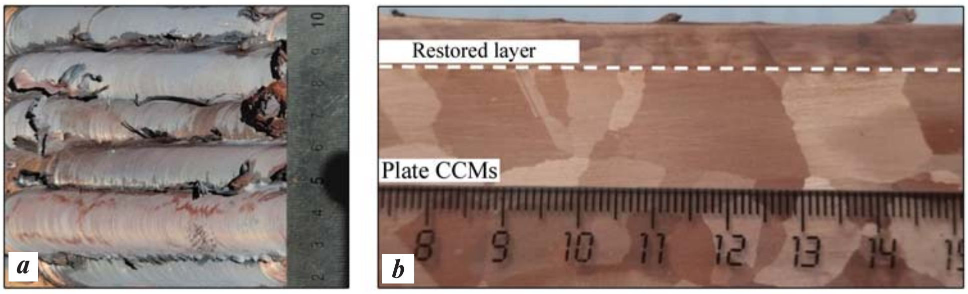

Fig. 8. Appearance of the FSW restored layer (***a***) and macrostructure of the restored layer and substrate in a transverse cross-section (***b***)

Рис. 8. Вид восстановленного СТП-слоя (***a***) и макроструктура восстановленного слоя и подложки в поперечном сечении (***b***)

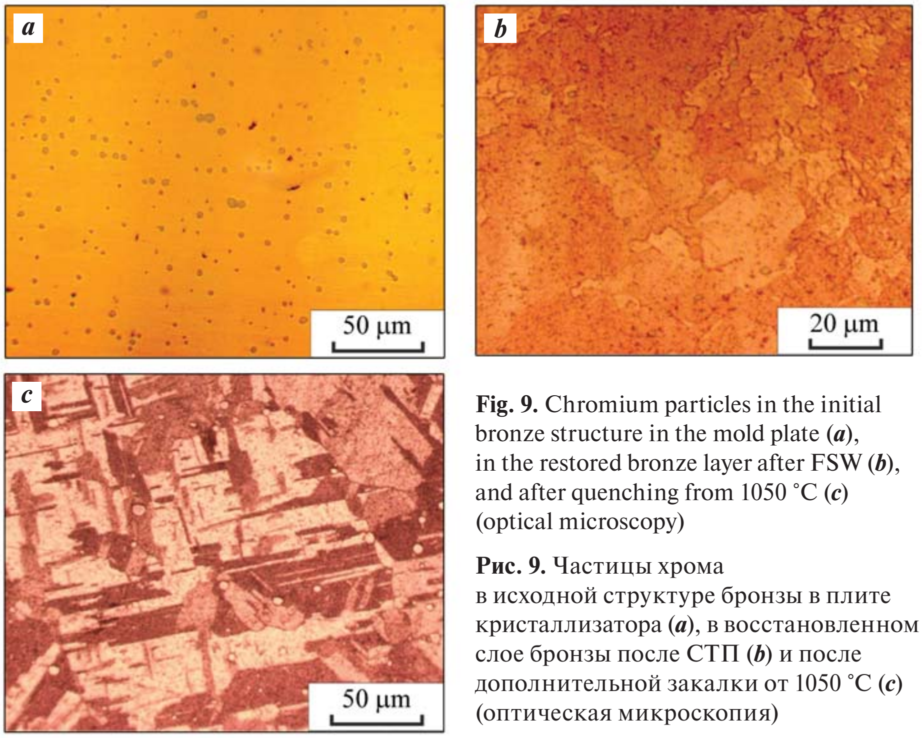

Fig. 9. Chromium particles in the initial bronze structure in the mold plate (***a***), in the restored bronze layer after FSW (***b***), and after quenching from 1050 °C (***c***) (optical microscopy)

Рис. 9. Частицы хрома в исходной структуре бронзы в плите кристаллизатора (***a***), в восстановленном слое бронзы после СТП (***b***) и после дополнительной закалки от 1050 °C (***c***) (оптическая микроскопия)

In Figure 8, *b*, it is evident that multi-pass welding, with a 6 mm step, generates a continuous bronze layer approximately 5 mm thick on the plate's surface. This layer is formed due to the partial overlap of welded joints. The restored layer exhibits a relatively uniform macrostructure. Importantly, no observable continuity defects such as breaks, cracks, or pores were detected either across the entire cross-section of the welded joint or along the boundary of the connection between the applied material and the metal of the plate undergoing restoration.

The analysis conducted via an automated hardness tester provided a 2D map, a 3D hardness distribution profile (Fig. 11), and a graph illustrating changes in hardness along the depth of the welded joint (Fig. 12, curve *1*). These assessments revealed a reduction in the hardness of the applied layer to a range of 85—105 HV1 due to multi-pass FSLW. This decrease contrasts with the initial hardness of the CCM mold plate, which was measured at 116—126 HV1. Additionally, no significant differences or noticeable drops in hardness were observed in the overlap area of adjacent passages. Within the thermomechanically affected zone (refer to Fig. 11, zone *II*), a slight increase in hardness was noted compared to the hardness level in the original (base) metal of the mold plate. This elevated hardness can be attributed to the deformation hardening of the plate material nearby the rotating welding tool caused by its mechanical action.

Optical metallography analysis reveals a notable dispersion in the structure of the deposited bronze layer, particularly evident in the weld nugget (Fig. 13). This dispersion results in the weld structure exhibiting grain sizes, ranging from units to tens of micrometers (Fig. 14). In the upper section of the layer restored by FSW (stir zone) (as shown in Fig. 13), a fine-grained equiaxial recrystallized structure emerges, characterized by a grain size of approximately 5 µm (refer to Fig. 14, *a*). While the predominant size of recrystallized grains in the stir zone falls within the range of

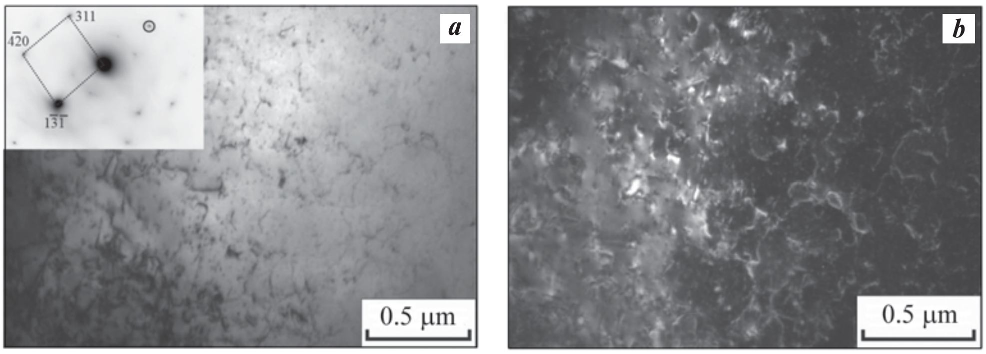

Fig. 10. Initial microstructure of the Cr–Zr bronze (TEM)
a – bright-field image and electron-diffraction pattern, zone axis $[12\bar{5}]$; ***b*** – dark-field image in the $\bar{1}31_{Cu}$ reflection

Рис. 10. Исходная структура бронзы из плиты кристаллизатора МНЛЗ (ПЭМ)
а – светлопольное изображение и картина микродифракции, ось зоны $[12\bar{5}]$; ***b*** – темнопольное изображение в рефлексе $\bar{1}31_{Cu}$

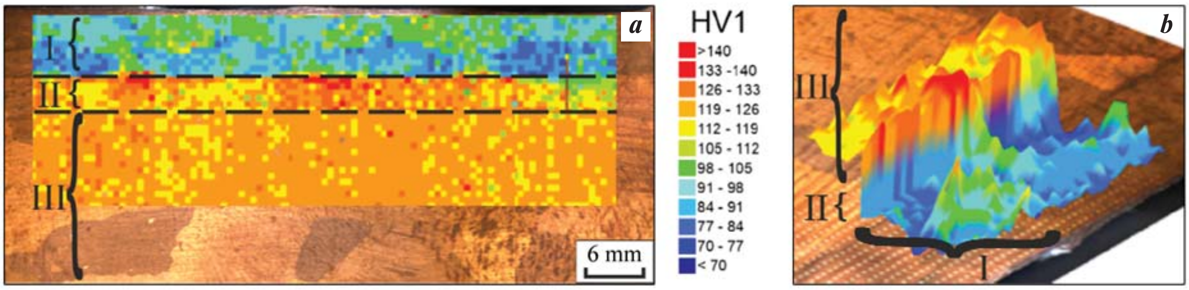

Fig. 11. Hardness distribution of the weld: 2D-map (***a***) and 3D profile (***b***)
I – stir zone of the restored layer; ***II*** – thermomechanically affected zone; ***III*** – initial (base) metal of the mold plate

Рис. 11. Распределение твердости по сечению сварного соединения: 2D-карта (***а***) и 3D-профиль (***b***)
I – восстановленный способом СТП слой бронзы (зона перемешивания); ***II*** – зона термомеханического влияния;
III – исходный (основной) металл плиты кристаллизатора

5 to 15 μm, observations at different depths beneath the surface reveal areas and bands spanning several hundred micrometers with a grain size of up to 20—50 μm (see Fig. 14, *b*, *c*). Within the thermomechanically affected zone (refer to Fig. 13), a combination of fine-grained structure and deformed coarse grains is evident (depicted in Fig. 14, *d*). These areas gradually transition into the structure resembling the initial material of the mold plate.

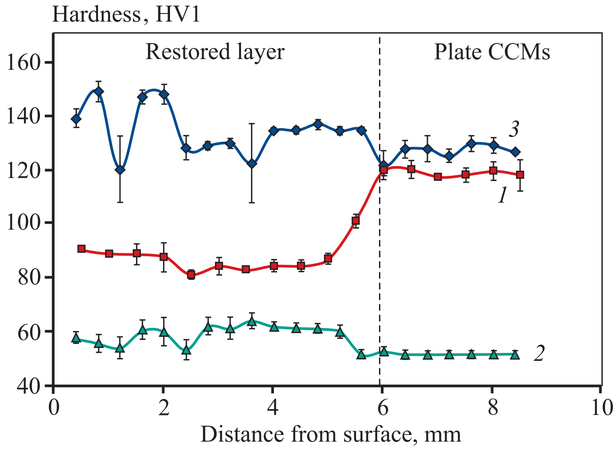

Fig. 12. Hardness distribution in the restored layer and the mold plate after various technological operations

1 – FSW; *2* – FSW + quenching 1050°C;
3 – FSW + quenching 1050°C + aging at 450°C

Рис. 12. Распределение твердости в восстановленном слое Cr–Zr-бронзы и плите кристаллизатора МНЛЗ после различных технологических операций

1 – СТП; *2* – СТП + закалка от 1050 °C;
3 – СТП + закалка от 1050 °C + старение при 450 °C

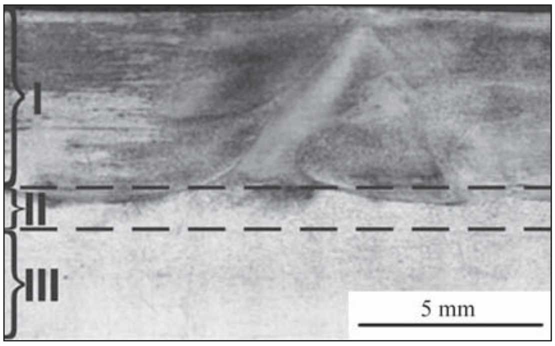

Fig. 13. General view of a transverse section of the weld

I – stir zone of the restored layer; *II* – thermomechanically affected zone; *III* – initial (base) metal of the mold plate

Рис. 13. Общий вид поперечного шлифа сварного соединения хромоциркониевой бронзы

I – восстановленный способом СТП слой (зона перемешивания);
II – зона термомеханического влияния;
III – исходный (основной) металл плиты кристаллизатора

The movement of material around the pin of the welding tool during FSW is intricate, characterized by gradients in the degree and rate of deformation as well as temperature fluctuations [18; 19]. Consequently, the microstructure in the weld nugget (stir zone) retains traces of varying thermomechanical histories of different metal layers. This leads to structural heterogeneity due to the complexity of FSW. In the case of multi-pass FSW (as shown in Fig. 7, *b* and 8, *a*), additional thermal and thermomechanical effects on the metal structure occur due to different weld zones overlapping (such as thermal and thermomechanically affected zones and the weld nugget). This further contributes to the observed structural heterogeneity in the restored layer and the zone of thermomechanical influence, as highlighted in Figs. 13 and 14. Notably, despite the varied grain sizes observed in these zones, it's essential to point out that this diversity did not significantly impact the uniformity of hardness distribution in these specified zones (as evident in Figs. 11 and 12). Furthermore, it's important to mention that the heat-affected zone does not exhibit distinct identification based on changes in the size of structural components or alterations in the material's hardness.

Transmission electron microscopy examinations in the stir zone reveal the presence of areas with deformed grains alongside a significant number of clean recrystallized grains characterized by broad banded boundaries (Fig. 15 *a*, *b*). Within these grains, chromium particles are observed (Fig. 15, *c*), with sizes that can extend up to 100 nm. Heating to high temperatures and intense plastic deformation during multi-pass FSW leads to the initiation of dynamic recrystallization processes behind the welding tool and contribute to the enlargement of strengthening phases (overaging). It's previously shown (refer to Fig. 9, *b*) that FSW does not result in complete dissolution of coarse chromium particles, which are initially present in the structure of the original plate (as seen in Fig. 9, *a*). Consequently, these relatively larger chromium particles, which can reach sizes of up to 5 μm, do not exert a decisive influence on the material's hardness.

The substantial decrease in hardness within the stir zone, from the initial 116—126 HV1 of the continuous caster mold plate to the range of 85—105 HV1 (as observed in Fig. 11 and 12), despite the significant refinement of the bronze grain structure (as depicted in Fig. 8, *b* and 14), is attributed to recrystallization and overaging processes resulting from multi-pass FSW. During the FSW of chromium zirconium bronze, the temperature measured at the periphery of the tool shoulder, composed of the heat-resistant alloy, registered at 500—550 °C (Fig. 16) using a non-contact laser pyrome-

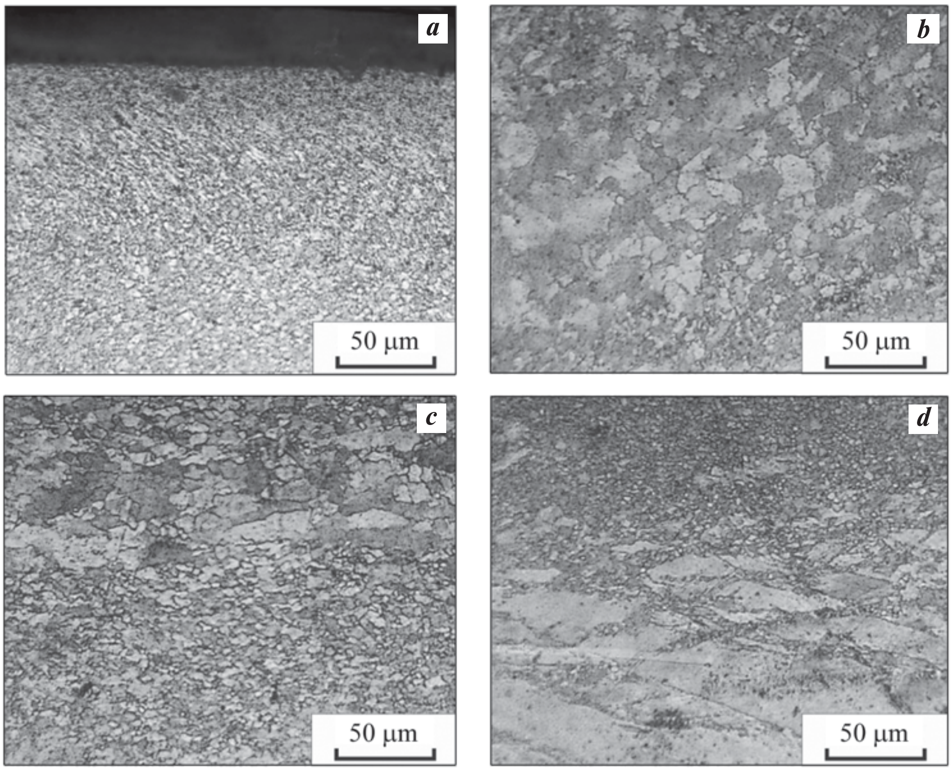

Fig. 14. Structure of chromium-zirconium bronze in the restored layer of the continuous caster mold plate after FSW (optical microscopy)

a – near the surface; ***b*** – mid area, ***c*** – area of variable grain structure, ***d*** – the transition zone «layer – base metal»

Рис. 14. Структура хромоциркониевой бронзы в восстановленном слое плиты кристаллизатора МНЛЗ после СТП (оптическая микроскопия)

a – вблизи поверхности; ***b*** – в центральной части восстановленного слоя, ***c*** – на границе участков с разноразмерной структурой, ***d*** – в переходной зоне с основным металлом

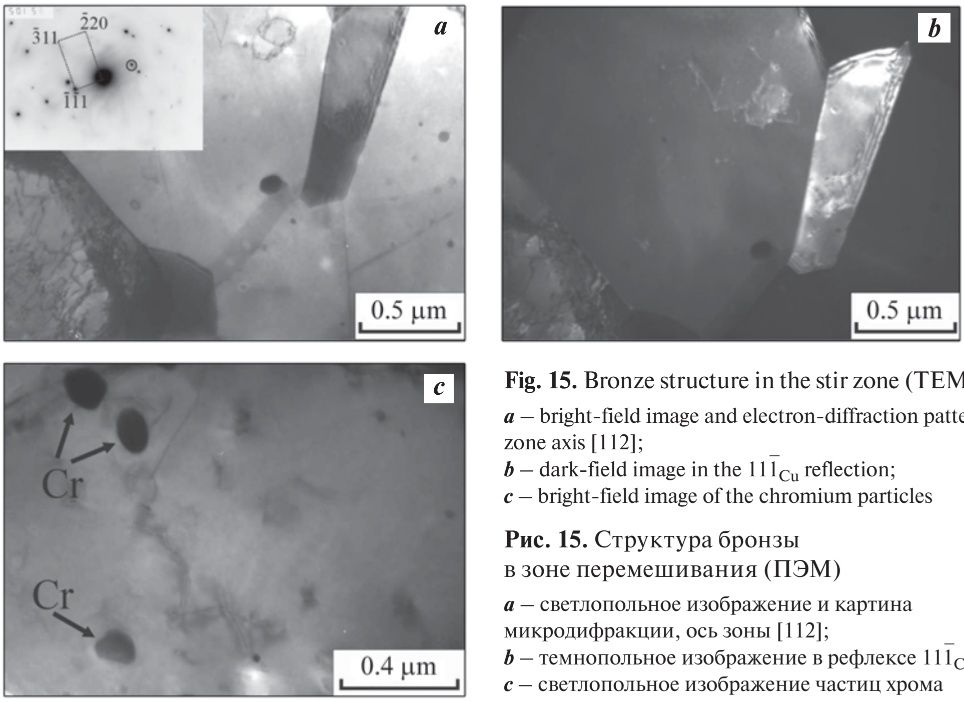

Fig. 15. Bronze structure in the stir zone (TEM)

a – bright-field image and electron-diffraction pattern, zone axis [112];
b – dark-field image in the $11\bar{1}_{\mathrm{Cu}}$ reflection;
c – bright-field image of the chromium particles

Рис. 15. Структура бронзы в зоне перемешивания (ПЭМ)

a – светлопольное изображение и картина микродифракции, ось зоны [112];
b – темнопольное изображение в рефлексе $11\bar{1}_{\mathrm{Cu}}$;
c – светлопольное изображение частиц хрома

ter. Simulation results [40] indicate that the temperature within the weld zone (stir zone) surpasses the measured value by 100—150 °C, reaching 600—700 °C. Additionally, the accumulation of metal heating under multi-pass FSW conditions contributes to the softening effect. In a study [39], during a single-pass FSW with a tool made of H13 die steel, which heated the welding zone to approximately 420 °C, a reduction in bronze softening was observed. Conversely, this led to material strengthening by 1.5—2.0 times. This outcome suggests that less heating did not trigger the development of overaging processes.

Quenching the material from 1050 °C induces substantial growth in many grains within the layer restored by multi-pass FSLW (Fig. 17, *a*, *b*). This growth occurs due to the development of recrystallization processes during high-temperature exposure to the quenching process. The thermal dissolution of dispersed strengthening phases, particularly chromium particles measuring up to 100 nm observed post-welding (refer to Fig. 15, *c*), facilitates the growth of recrystallized grains. Consequently, in certain areas of the restored layer, grain growth expands to several hundred microns, often accompanied by the formation of annealing twins (depicted in Fig. 17, *a*, *b*). The observed grain coarsening and the dissolution of dispersed reinforcing chromium particles contribute to significant softening, reducing

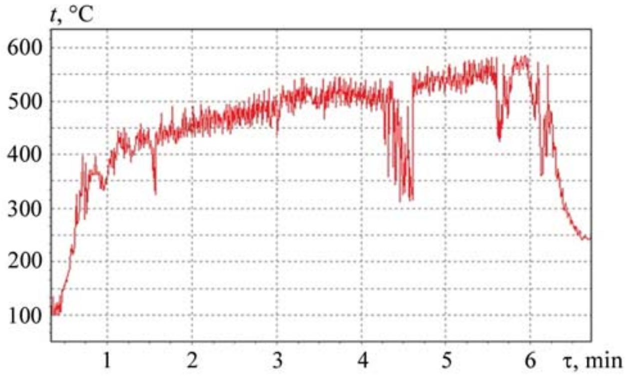

Fig. 16. Temperature variation at the periphery of the welding tool shoulder during FSW of Cr—Zr bronze

Рис. 16. Изменение температуры на периферии заплечика сварочного инструмента в процессе плоскостной СТП хромоциркониевой бронзы

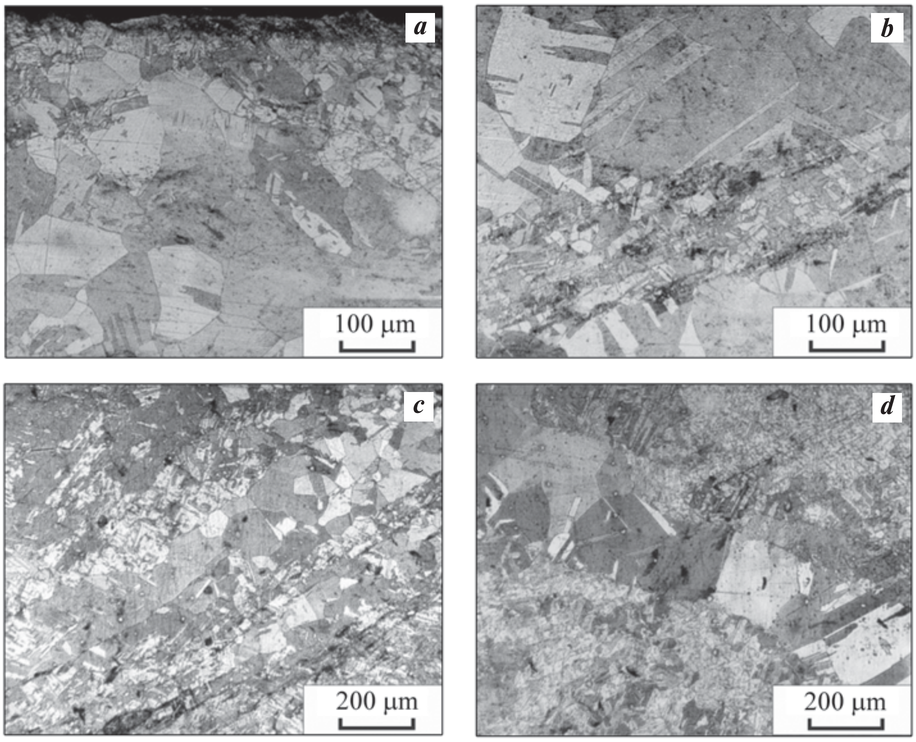

Fig. 17. Cr—Zr bronze structure in the restored layer after various heat treatments (optical microscopy)

a, ***b*** – FSW + quenching from 1050 °C; ***c***, ***d*** – FSW + quenching from 1050 °C + aging at 450 °C
a, ***c*** – near the surface; ***b***, ***d*** – in the mid area of the restored layer

Рис. 17. Структура хромоциркониевой бронзы в восстановленном слое плиты кристаллизатора МНЛЗ после различных термических обработок (оптическая микроскопия)

a, ***b*** – СТП + закалка от 1050 °C; ***c***, ***d*** – СТП + закалка от 1050 °C + старение при 450 °C
a, ***c*** – вблизи поверхности; ***b***, ***d*** – в центральной части восстановленного слоя

the hardness to values between 52—62 HV1, observed in both the restored layer with a dispersed structure and the coarse-grained base material of the plate (Fig. 12, curve *2*). Interestingly, even after one hour of hardening at $t = 1050$ °C, coarse chromium particles up to 5 microns in size, initially present in the bronze structure of the original plate (as seen in Fig. 9, *a*) and post-FSW treatment (as shown in Fig. 9, *b*), retain in the structure (seen in Fig. 9, *c*). This retention is due to the limited solubility of chromium in copper, which at the specified quenching temperature does not exceed 0.6 wt.% [41].

According to the observations made through transmission electron microscopy, following the quenching process, coarse grains exhibit a limited number of dislocations found both inside the grain and at high-angle boundaries (Fig. 18, *a*). Additionally, undissolved dispersed chromium particles, measuring up to 30 nm, are present (Fig. 18, *b*), alongside twins (Fig. 18, *c*, *d*). Figures 18, *c*, *d* also show a deformation contrast in the form of “butterfly wings” or arcs. The structural images reveal specific contrasts, such as “coffee beans” and “rings”, which indicate the presence of Guinier—Preston zones within the structure. These zones are known to be coherently associated with the matrix [44; 45] or forming nuclei of chromium particles that generate a field of elastic stresses around themselves within the matrix [46]. The emergence of such characteristic structural features of aged bronze post-quenching in water [44—46] could be linked to the use of a sealed ampoule during the high-temperature heating of the sample, causing a delay in its cooling process.

Quenching followed by aging at $t = 450$ °C results in the strengthening of the weld joint to 120—150 HV1 (as observed in Fig. 12, curve *3*). This strengthening effect occurs despite the presence of large grains within the structure of the restored layer (seen in Fig. 17, *c*, *d*), formed during the heating to 1050 °C for quenching. In the bright-field TEM image, a contrast in the form of arcs is observed within the grain bulk (Fig. 19, *a*), indicating the initial stages of fine strengthening phase formation. Moreover, the dark-field image in Fig. 19, *b* indicates the release of a considerable number of dispersed particles enriched with chromium from a supersaturated solid solution. These released particles play a significant role in efficient dispersion strengthening, affecting both the layer restored by FSW and the origi-

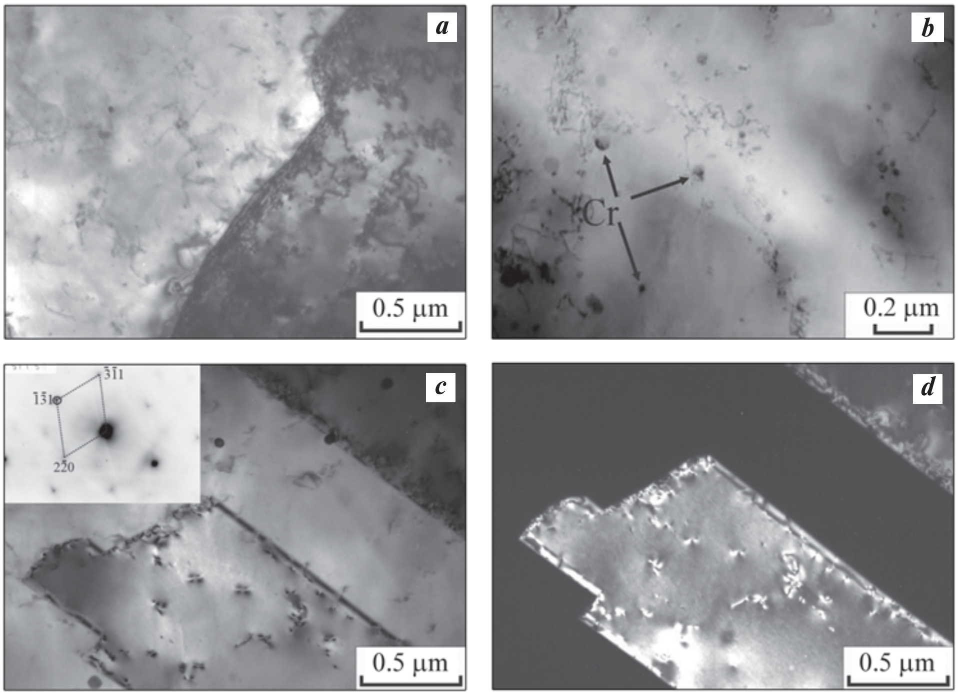

Fig. 18. Bronze structure in the stir zone of FSW joint at a depth of 1 mm (***a***, ***b***) and at a depth of 4 mm (***c***, ***d***) after quenching from 1050 °C (TEM)

a, ***b*** – bright-field images; ***c*** – bright-field image and electron-diffraction pattern, zone axis [114]; ***d*** – dark-field image in the $\overline{13}1_{\text{Cu}}$ reflection

Рис. 18. Структура бронзы в зоне перемешивания СТП на глубине 1 мм (***a***, ***b***) и 4 мм (***c***, ***d***) после закалки от 1050 °C (ПЭМ)

a, ***b*** – светлопольные изображения; ***c*** – светлопольное изображение и картина микродифракции, ось зоны [114],
d – темнопольное изображение в рефлексе $\overline{13}1_{\text{Cu}}$

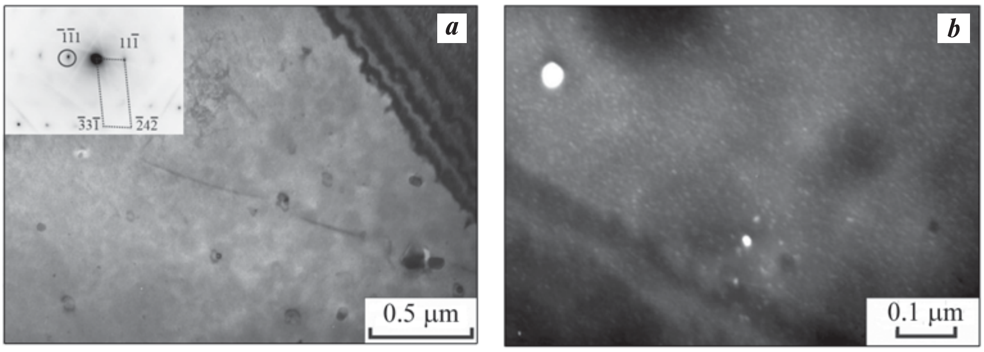

Fig. 19. Bronze structure in the stir zone near the surface at a depth of 1 mm, after quenching from 1050 °C followed by aging at 450 °C (TEM)

a – bright-field image and microdiffraction pattern, zone axis [123]; ***b*** – dark-field image in the $\bar{1}11_{\text{Cu,Cr}}$ mixed reflection

Рис. 19. Структура бронзы в зоне перемешивания СТП на глубине 1 мм после закалки от 1050 °C и старения при 450 °C (ПЭМ)

a – светлопольное изображение и картина микродифракции, ось зоны [123];
b – темнопольное изображения в смешанном рефлексе $\bar{1}11_{\text{Cu,Cr}}$

nal plate of chromium-zirconium bronze (as seen in Fig. 12, curve *3*). This signifies the dominant role of the dispersion strengthening mechanism over the grain boundary strengthening mechanism. Active release of dispersed chromium particles during aging is facilitated by the presence of chromium-enriched Guinier—Preston zones or chromium particle nuclei, as observed in the discussion regarding Fig. 18, *c*, *d*, subsequent to hardening. Consequently, this heat treatment process (quenching followed by aging) effectively reverses the de-strengthening effect observed in the stir zone of chromium-zirconium bronze, a result of overaging during the multi-pass FSW caused by overheating.

Conclusions

The manufacture and restoration of CCM molds hold significant strategic importance for ensuring the national safety of the Russian Federation within the steel industry. An innovative technology has been developed and practically implemented in major Russian metallurgical enterprises for the restoration and production of new mold plates, incorporating wear-resistant composite HVAF thermal spray coatings. This innovation has shown remarkable performance, surpassing imported plates with galvanic coatings by a significant margin (4—20 times), while simultaneously enhancing the quality of the produced workpieces. Consequently, the reliance on foreign slab molds in Russian metallurgical plants has been decreased from 97 % in 2012 to 40 % by the end of 2022.

To prolong the service life and reduce the cost of consumable components in a CCM, solutions are being sought to address the pressing issue of restoring copper plates of slab molds after reaching the minimum permissible thickness due to operation and repairs. The advantages and potential of restoring mold plates using Cr—Zr bronze are being explored, employing the environmentally friendly method of multi-pass Friction Stir Lap Welding by applying a filler plate made of the same material onto the restored plate. A series of successive passes using a rotating conical tool with partial joints overlap produced a welded layer (restored bronze layer) approximately 5 mm thick, exhibiting no critical continuity defects such as breaks, cracks, or pores. Various grain sizes, ranging from units to tens of microns, were observed in the weld zones.

The FSW process, coupled with blowing the welding zone with an air jet, resulted in softening of the bronze within the restored layer, measuring 85—105 HV1 compared to the original plate hardness of 116—126 HV1. This softening phenomenon is linked to dynamic recrystallization and overaging, involving the coarsening of chromium particles to approximately 100 nm in Cr—Zr bronze due to heating the weld nugget (stir zone) to temperatures of 600—700°C.

Subsequent quenching from 1050 °C further contributed to the softening of the bronze, reducing its hardness to 52—62 HV1. This affected both the FSW restored layer with a dispersed structure and the original plate containing coarse grains (5—20 mm) due to the development of recrystallization and thermal dissolution of dispersed strengthening phases (chromium particles) up to 100 nm in size, observed post-welding.

Subsequent aging at a t = 450 °C results in the strengthening of the restored layer to a 120—150 HV1, despite the retention of coarse-grained structure formed during the heating process for quenching. This efficient strengthening during aging, observed in both the restored layer and the original plate, is attributed to the release of chromium-enriched dispersed particles from a supersaturated solid solution. This highlights the predominant role of the dispersion mechanism in strengthening Cr—Zr bronze over the grain-boundary strengthening mechanism. The active release of dispersed chromium particles during aging is facilitated by the formation of chromium-enriched Guinier—Preston zones or nuclei of chromium particles within the bronze layer restored by FSW, which begins during the quenching stage. Consequently, the softening of bronze during multi-pass FSW can be effectively eliminated by quenching followed by aging.

The restoration of copper plates to their original thickness using multi-pass friction stir lap welding coupled with the subsequent application of wear-resistant composite coatings ensures a continuous operational cycle for slab molds and substantially diminishes the necessity for their importation. The utilization of advanced FSW methods for plate restoration, apart from being economically efficient, also promises considerable environmental benefits. This approach reduces the requirement for environmentally harmful metallurgical production to manufacture new mold plates from copper alloys.

References

1. Kotelnikov A.V., Vopneruk A.A., Makarov A.V., Korobov Yu.S., Kirichkov A.A., Dagman A.I., Shefrin I.N. New materials and technologies for significantly increase the wear resistance of the working surface of metallurgical equipment. *Tyazheloe mashinostroenie*. 2018;(9):14—20. (In Russ.).
   Котельников А.Б., Вопнерук А.А., Макаров А.В., Коробов Ю.С., Киричков А.А., Дагман А.И., Шифрин И.Н. Новые материалы и технологии существенного повышения износостойкости рабочей поверхности металлургического оборудования. *Тяжелое машиностроение*. 2018;(9):14—20.
2. Vdovin K.N., Pozin A.E. Cavitation wear of coated copper walls of molds. *Stal'*. 2018;(9):14—20. (In Russ.).
   Вдовин К.Н., Позин А.Е. Кавитационный износ медных стенок кристаллизаторов с покрытием. *Сталь*. 2017;(3):49—51.
3. Kushnarev A.V., Kirichkov A.A., Vopneruk A.A., Kotelnikov A.V., Korobov Yu.S., Makarov A.V., Filatov S.V., Shefrin I.N. Physico-mechanical characteristics of thermal sprayed coatings on the walls of the mold of continuous casting machines. *Svarka i diagnostika*. 2017;(5):50—53. (In Russ.).
   Кушнарев А.В., Киричков А.А., Вопнерук А.А., Котельников А.Б., Коробов Ю.С., Макаров А.В., Филатов С.В., Шифрин И.Н. Физико-механические характеристики газотермических покрытий стенок кристаллизатора машин непрерывного литья заготовок. *Сварка и диагностика*. 2017;(5):50—53.
4. Korobov Yu.S., Kotelnikov A.B., Kushnarev A.V., Kirichkov A.A., Filippov M.A., Vopneruk A.A. Analysis of the features of the formation of thermal sprayed coatings on the wall slab crystallizer. *Chernye metally*. 2017;(1):41—45. (In Russ.).
   Коробов Ю.С., Котельников А.Б., Кушнарев А.В., Киричков А.А., Филиппов М.А., Вопнерук А.А. Анализ особенностей формирования газотермических покрытий на стенке слябового кристаллизатора. *Черные металлы*. 2017;(1):41—45.
5. Makarov A.V., Soboleva N.N., Malygina I.Yu. Role of the strengthening phases in abrasive wear resistance of laser-clad NiCrBSi coatings. *Journal of Friction and Wear*. 2017;38(4): 272—278.
   Макаров А.В., Соболева Н.Н., Малыгина И.Ю. Роль упрочняющих фаз в сопротивлении абразивному изнашиванию NiCrBSi покрытий, сформированных лазерной наплавкой. *Трение и износ*. 2017;38(4): 311—318.
6. Makarov A.V., Soboleva N.N., Malygina I.Yu., Osintseva A.L. Possibility of obtaining heat-resistant coating: Patent 2492980 (RF). 2013. (In Russ.).
   Макаров А.В., Соболева Н.Н., Малыгина И.Ю., Осинцева А.Л. Способ получения теплостойкого покрытия: Патент 2492980 (РФ). 2013.
7. Makarov A.V., Soboleva N.N., Malygina I.Yu., Osintseva A.L. Formation of wear-resistant chromium-nickel coating with extra high thermal stability by combined laser-and-heat treatment. *Metal Science and Heat Treatment*. 2015;57(3-4):161—168.
   Макаров А.В., Соболева Н.Н., Малыгина И.Ю., Осинцева А.Л. Формирование износостойкого хромоникелевого покрытия с особо высоким уровнем теплостойкости комбинированной лазерно-термической обработкой. *Металловедение и термическая обработка металлов*. 2015;(3):39—46.
8. Makarov A.V., Soboleva N.N., Malygina I.Yu., Kharanzhevskiy E.V. Improving the properties of a rapidly crystallized NiCrBSi laser clad coating with high-temperature processing. *Journal of Crystal Growth*. 2019;525;125200.
   https://doi.org/10.1016/j.jcrysgro.2019.125200
9. Soboleva N.N., Makarov A.V. Effect of conditions of high-temperature treatment on the structure and tribological

properties of nickel-based laser-clad coating. *Russian Journal of Non-Ferrous Metals*. 2021;62(6): 682—691. https://link.springer.com/article/10.3103/S1067821221060183
Соболева Н.Н., Макаров А.В. Влияние условий высокотемпературной обработки на структуру и трибологические свойства наплавленного лазером покрытия на никелевой основе. *Известия вузов. Цветная металлургия*. 2021;27(5):67—77. https://doi.org/10.17073/0021-3438-2021-5-67-77

10. Gurevich S.M. Handbook on welding of non-ferrous metals. Kiev: Naukova dumka, 1981. 608 p.
Гуревич С.М. Справочник по сварке цветных металлов. Киев: Наукова думка, 1981. 608 p. (In Russ.).
11. Kazakov N.F. Diffusion Bonding of Materials. Oxford, New York: Pergamon Press, 1985. 304 p.
12. Lysak V., Kuzmin S. Lower boundary in metal explosive welding. Evolution of ideas. *Journal of Materials Processing Technology*. 2012;212(1):150—156. https://doi.org/10.1016/j.jmatprotec.2011.08.017
13. Nazarov A.A., Murzinova M.A., Mukhametgalina A.A., Shayakhmetova E.R. Bulk ultrasonic treatment of crystalline materials. *Metals*. 2023;13(2):344. https://doi.org/10.3390/met13020344
14. Sun F., Liu P., Chen X., Zhou H., Guan P., Zhu B., Mechanical properties of high-strength Cu—Cr—Zr alloy fabricated by selective laser melting. *Materials*. 2020;13;5028. https://doi.org/10.3390/ma13215028
15. Tang X., Chen X., Sun F., Liu P., Zhou H., Fu S. The current state of CuCrZr and CuCrNb alloys manufactured by additive manufacturing: A review. *Materials & Design*. 2022;224;111419. https://doi.org/10.1016/j.matdes.2022.111419
16. Klimenko Yu.V. Method of friction welding of metals: Patent 195846 (USSR). 1967. (In Russ.).
Клименко Ю.В. Способ сварки металлов трением: Патент 195846 (СССР). 1967.
17. Thomas W.M., Nicholas E.D., Needham J.C., Murch M.G., Templesmith P., Dawes C.J. Optimization of welding parameters for friction stir lap welding of AA6061-T6 alloy: Patent PCT/GB92/02203 (International).1991.
18. Mishra R.S., Ma Z.Y. Friction stir welding and processing. *Materials Science and Engineering: R*. 2005;50(1-2):1—78. https://doi.org/10.1016/j.mser.2005.07.001
19. Mishra R.S., Mahoney M.W. Friction stir welding and processing. *ASM International*. 2007;1:1—5. https://doi.org/10.1361/fswp2007p001
20. Heidarzadeh A., Mironov S., Kaibyshev R., Çam G., Simar A., Gerlich A., Khodabakhshi F., Mostafaei A., Field D.P., Robson J.D., Deschamps A., Withers P.J. Friction stir welding/processing of metals and alloys: A comprehensive review on microstructural evolution. *Progress in Materials Science*. 2021;(117):100752. https://doi.org/10.1016/j.pmatsci.2020.100752
21. Lee W.B., Jung S.B. The joint properties of copper by friction stir welding. *Materials Letters*. 2004;58(6): 1041—1046. https://doi.org/10.1016/j.matlet.2003.08.014
22. Sun Y.F., Fujii H. Investigation of the welding parameter dependent microstructure and mechanical properties of friction stir welded pure copper. *Materials Science and Engineering: A*. 2010;527(26):6879—6886. https://doi.org/10.1016/j.msea.2010.07.030
23. Surekha K., Els-Botes A. Development of high strength, high conductivity copper by friction stir processing. *Materials & Design*. 2011;32(2)911—916. https://doi.org/10.1016/j.matdes.2010.08.028
24. Palko W.A., Fielder R.S., Young P.F. Investigation of the use of friction stir processing to repair and locally enhance the properties of large NiAl bronze propellers. *Materials Science Forum*. 2003;426-432:2909—2914. https://doi.org/10.4028/www.scientific.net/MSF.426-432.2909
25. Oh-Ishi K., Zhilyaev A.P., McNelley T.R. A microtexture investigation of recrystallization during friction stir processing of as-cast NiAl bronze. *Metallurgical and Materials Transactions A*. 2006;37(7):2239—2251. https://doi.org/10.1007/BF02586143
26. Barlas Z., Uzun H. Microstructure and mechanical properties of friction stir butt welded dissimilar Cu/CuZn30 sheets. *Journal of Achievements in Materials and Manufacturing Engineering*. 2008;30(2):182—186.
27. Heidarzadeh A. Saeid T., Klemm V., Chabok A., Pei Y. Effect of stacking fault energy on the restoration mechanisms and mechanical properties of friction stir welded copper alloys. *Materials & Design*. 2019;162:185—197. https://doi.org/10.1016/j.matdes.2018.11.050
28. Galvão I., Loureiro A., Rodrigues D. M. Critical review on friction stir welding of aluminium to copper. *Science and Technology of Welding and Joining*. 2016;21(7):523—546. https://doi.org/10.1080/13621718.2015.1118813
29. Zoeram A.S., Anijdan S.H.M., Jafarian H.R., Bhattacharjee T. Welding parameters analysis and microstructural evolution of dissimilar joints in Al/Bronze processed by friction stir welding and their effect on engineering tensile behavior. *Materials Science and Engineering: A*. 2017;687:288—297. https://doi.org/10.1016/j.msea.2017.01.071
30. Narasimharaju S., Sankunny S. Microstructure and fracture behavior of friction stir lap welding of dissimilar AA 6060-T5/Pure copper. *Engineering Solid Mechanics*. 2019;7(3):217—228. https://doi.org/10.5267/j.esm.2019.5.002

31. Avettand-Fènoël M.N., Nagaoka T., Marinova M., Taillard R. Upon the effect of Zn during friction stir welding of aluminum-copper and aluminum-brass systems. *Journal of Manufacturing Processes*. 2020;58: 259—278. https://doi.org/10.1016/j.jmapro.2020.08.006
32. Ni D.R., Xiao B.L., Ma Z.Y., Qiao Y.X., Zheng Y.G. Corrosion properties of friction—stir processed cast NiAl bronze. *Corrosion Science*. 2010;52(5):1610—1617. https://doi.org/10.1016/j.corsci.2010.02.026
33. Li Y., Lian Y., Sun Y. Cavitation erosion behavior of friction stir processed nickel aluminum bronze. *Journal of Alloys and Compounds*. 2019;795:233—240. https://doi.org/10.1016/j.jallcom.2019.04.302
34. Lv Y., Nie B., Wang L., Cui H., Li L., Wang R., Lyu F. Optimal microstructures on fatigue properties of friction stir processed NiAl bronze alloy and its resistant fatigue crack growth mechanism. *Materials Science and Engineering: A*. 2020;771:138577. https://doi.org/10.1016/j.msea.2019.138577
35. He D.Q., Lai R.L., Xu Sh.H., Yang K.Y., Ye Sh.Y., Wang J., Zhu J.M., Suet B. Microstructure and mechanical properties of Cu—Cr—Zr alloy by friction stir welding. *Advanced Materials Research*. 2012;602-604:608—611. https://doi.org/10.4028/www.scientific.net/AMR.602-604.608
36. Wang Y.D., Zhu S.Z., Xie G.M., Wu L.H., Xue P., Ni D.R., Xiao B.L., Ma Z.Y. Realising equal-strength welding with good conductivity in Cu—Cr—Zr alloy via friction stir welding. *Science and Technology of Welding and Joining*. 2021;26(6):448—454. https://doi.org/10.1080/13621718.2021.1935151
37. Nikityuk Yu.N., Grigorenko G.M., Zelenin V.I., Zelenin E.V., Poleshchuk M.A. Technology for the restoration of slab molds of continuous casters using friction stir surfacing. *Sovremennaya elektrometallurgiya*. 2013;(3): 51—55. (In Russ.).
Никитюк Ю.Н., Григоренко Г.М., Зеленин В.И., Зеленин Е.В., Полещук М.А. Технология восстановительного ремонта слябовых кристаллизаторов МНЛЗ способом наплавки трением с перемешиванием. *Современная электрометаллургия*. 2013;(3):51—55.
38. Grigorenko G.M., Adeeva L.I., Tunik A.Yu., Poleshchuk M.A., Zelenin V.I., Zelenin E.V. Refurbishment of slab copper crystallizers of continuous casting machines. Structure and properties of metal in the joint zone. *Sovremennaya elektrometallurgiya*. 2015;(1):44—49.
Григоренко Г.М., Адеева Л.И., Туник А.Ю., Полещук М.А., Зеленин В.И., Зеленин Е.В. Восстановительный ремонт слябовых медных кристаллизаторов МНЛЗ. Структура и свойства металла в зоне соединения. *Современная электрометаллургия*. 2015;(1):44—49.
39. Lezhnin N.V., Makarov A.V., Volkova E.G., Valiullin A.I., Kotelnikov A.B., Vopneruk A.A. Realizing ultrafine grain structure of Cu—Cr—Zr alloy via friction stir welding/processing. *Letters on Materials*. 2022;12(4):428—432. https://doi.org/10.22226/2410-3535-2022-4-428-432
40. Lai R., Li X., He D., Lin J., Li J., Lei Q. Microstructures evolution and localized properties variation of a thick friction stir welded CuCrZr alloy plate. *Journal of Nuclear Materials*. 2018;510;70—79. https://doi.org/10.1016/j.jnucmat.2018.07.055
41. Osintsev O.E., Fedorov V.N. Copper and copper alloys. Domestic and foreign brands: Directory. 2nd ed., revised. and additional Moscow: Innovatsionnoe mashinostroenie, 2016. 360 p. (In Russ.).
Осинцев О.Е., Федоров В.Н. Медь и медные сплавы. Отечественные и зарубежные марки: Справочник. 2-е изд., перераб. и доп. М.: Инновационное машиностроение, 2016. 360 с.
42. Morozova A., Mishnev R., Belyakov A., Kaibyshev R. Microstructure and properties of fine grained Cu—Cr—Zr alloys after termo-mechanical treatments. *Reviews on Advanced Materials Science*. 2018;54;56—92. https://doi.org/10.1515/rams-2018-0020
43. Khomskaya I.V., Zel'dovich V.I., Frolova N.Y., Abdullina D.N., Kheifets A.E. Investigation of Cu_5Zr particles precipitation in Cu—Zr and Cu—Cr—Zr alloys subjected to quenching and high strain rate deformation. *Letters on Materials*. 2019;9(4):400—404. https://doi.org/10.22226/2410-3535-2019-4-400-404
44. Edwards D.J., Singh B.N., Tähtinen S. Effect of heat treatments on precipitate microstructure and mechanical properties of a CuCrZr alloy. *Journal of Nuclear Materials*. 2007;367-370:904—909. https://doi.org/10.1016/j.jnucmat.2007.03.064
45. Park J.-Y., Lee J.-S., Choi B.-K., Hong B.G., Jeong Y.H. Effect of cooling rate on mechanical properties of aged ITER-grade CuCrZr. *Fusion Engineering and Design*. 2008;83:1503—1507. https://doi.org/10.1016/j.fusengdes.2008.07.006
46. Zel'dovich V.I., Khomskaya I.V., Frolova N.Yu., Kheifets A.E., Shorokhov E.V., Nasonov P.A. Structure of chromium-zirconium bronze subjected to dynamic channel-angular pressing and aging. *Physics of Metals and Metallography*. 2013;114(5):411—418. https://doi.org/10.1134/S0031918X13050141
Зельдович В.И., Хомская И.В., Фролова Н.Ю., Хейфец А.Э, Шорохов Е.В., Насонов П.А. Структура хромоциркониевой бронзы, подвергнутой динамическому канально-угловому прессованию и старению. *Физика металлов и металловедение*. 2013;114(5):449—456. https://doi.org/10.7868/S0015323013050148

Information about the authors

Alexey V. Makarov – Dr. Sci. (Eng.), Corresponding Member of RAS, Head of Materials Science Department, Head of Mechanical Properties Laboratory, M.N. Miheev Institute of Metal Physics of Ural Branch of the Russian Academy of Sciences (IMP UB RAS).
https://orcid.org/0000-0002-2228-0643
E-mail: av-mak@yandex.ru

Nikita V. Lezhnin – Cand. Sci. (Eng.), Senior Research Scientist of Mechanical Properties Laboratory, IMP UB RAS.
https://orcid.org/0000-0001-9483-6607
E-mail: nlezhnin@bk.ru

Alexander B. Kotelnikov – General Director of CJSC Scientific and Production Enterprise «Mashprom”.
https://orcid.org/0009-0005-9471-9378
E-mail: office@mashprom.ru

Alexander A. Vopneruk – Cand. Sci. (Eng.), Project Manager of CJSC Scientific and Production Enterprise “Mashprom”.
https://orcid.org/0000-0002-0179-5453
E-mail: vopneruk@gmail.com

Yuri S. Korobov – Dr. Sci. (Eng), Chief Research Scientist, Head of Laboratory of Laser and Plasma Processing, IMP UB RAS; Professor of the Department of Welding Production Technology, Ural Federal University named after the First President of Russia B.N. Yeltsin.
https://orcid.org/0000-0003-0553-918X
E-mail: yukorobov@imp.uran.ru

Andrey I. Valiullin – Cand. Sci. (Eng.), Research Scientist of Mechanical Properties Laboratory, IMP UB RAS.
https://orcid.org/0000-0001-5539-4295
E-mail: a_valiullin@mail.ru

Elena G. Volkova – Cand. Sci. (Phys.-Math.), Senior Research Scientist of Mechanical Properties Laboratory, IMP UB RAS.
https://orcid.org/0000-0003-4958-3027
E mail: volkova@imp.uran.ru

Информация об авторах

Алексей Викторович Макаров – д.т.н., чл.-корр. РАН, гл. науч. сотрудник, зав. отделом материаловедения и лабораторией механических свойств Института физики металлов им. М.Н. Михеева Уральского отделения Российской академии наук (ИФМ УрО РАН).
https://orcid.org/0000-0002-2228-0643
E-mail: av-mak@yandex.ru

Никита Владимирович Лежнин – к.т.н., ст. науч. сотрудник лаборатории механических свойств ИФМ УрО РАН.
https://orcid.org/0000-0001-9483-6607
E-mail: nlezhnin@bk.ru

Александр Борисович Котельников – ген. директор ЗАО «НПП “Машпром”».
https://orcid.org/0009-0005-9471-9378
E-mail: office@mashprom.ru

Александр Александрович Вопнерук – к.т.н., руководитель проекта ЗАО «НПП “Машпром”».
https://orcid.org/0000-0002-0179-5453
E-mail: vopneruk@gmail.com

Юрий Станиславович Коробов – д.т.н., гл. науч. сотрудник, зав. лабораторией лазерной и плазменной обработки ИФМ УрО РАН; профессор кафедры технологии сварочного производства Уральского федерального университета имени первого Президента России Б.Н. Ельцина.
https://orcid.org/0000-0003-0553-918X
E-mail: yukorobov@imp.uran.ru

Андрей Илдарович Валиуллин – к.т.н., науч. сотрудник лаборатории механических свойств ИФМ УрО РАН.
https://orcid.org/0000-0001-5539-4295
E-mail: a_valiullin@mail.ru

Елена Георгиевна Волкова – к.ф.-м.н., ст. науч. сотрудник лаборатории механических свойств ИФМ УрО РАН.
https://orcid.org/0000-0003-4958-3027
E mail: volkova@imp.uran.ru

Contribution of the authors

A.V. Makarov – conceptualized and defined the work's objectives, wrote the manuscript.

N.V. Lezhnin – conducted sample welding, prepared thin sections, conducted optical microscopy, and contributed to defining the work's objectives and discussing the results.

A.B. Kotelnikov – contributed to defining the work's objectives and discussing the results.

A.A. Vopneruk – contributed to defining the work's objectives and discussing the results

Yu.S. Korobov – Contributed to manuscript writing.

A.I. Valiullin – conducted microhardness measurements and assisted in data plotting.

E.G. Volkova – conducted transmission electron microscopy.

Вклад авторов

А.В. Макаров – определение цели работы, написание статьи.

Н.В. Лежнин – сварка образцов, подготовка шлифов, проведение оптической микроскопии, участие в определении цели работы и обсуждении результатов.

А.Б. Котельников – участие в определении цели работы и обсуждении результатов.

А.А. Вопнерук – участие в определении цели работы и обсуждении результатов.

Ю.С. Коробов – участие в написании текста статьи.

А.И. Валиуллин – измерение микротвердости, построение графиков.

Е.Г. Волкова – проведение просвечивающей электронной микроскопии.

The article was submitted 20.10.2023, revised 06.11.2023, accepted for publication 10.11.2023

Статья поступила в редакцию 20.10.2023, доработана 06.11.2023, подписана в печать 10.11.2023